INVESTIGATION OF DAY- AND NIGHT-TIME NOX/VOCS COUPLING USING THERMAL DISSOCIATION CAVITY RING-DOWN SPECTROSCOPY

Dissertation
zur Erlangung des Grades

"Doktor der Naturwissenschaften"

im Promotionsfach Chemie

am Fachbereich Chemie, Pharmazie und Geowissenschaften
der Johannes Gutenberg-Universitätin Mainz

Nicolas Jean Sobanski

geb. in Arras, France am 20.09.1988

Mainz, den 06.10.2016

I hereby declare that I wrote the dissertation submitted without any unauthorized external assistance and used only sources acknowledged in the work. All textual passages which are appropriated verbatim or paraphrased from published and unpublished texts as well as all information obtained from oral sources are duly indicated and listed in accordance with bibliographical rules. In carrying out this research, I compiled with the rules of standard scientific practice as formulated in the statutes of Johannes Gutenberg University Mainz to insure standard scientific practice.

Table of Contents

Abstract

Reactive nitrogen species, so called NOy, are a class of compounds involved in different atmospheric cycles that impact the global distribution of atmospheric trace gases. The NOz group of compounds , whose precursors are NOx ($NO + NO_2$), includes short lived species like NO_3, HONO, RO_2NO_2, $ClNO_2$ and longer lived species like N_2O_5, HNO_3, $R(O)O_2NO_2$ and $RONO_2$. The fate of NOy (NOx + NOz) in the lowest layer of the atmosphere, the planetary boundary layer, has a strong influence on ozone levels, on HOx ($OH + HO_2 + RO_2$) species and on aerosol particles composition. The destruction of NOx through processes other than NO_2 photolysis (which produces NO) like conversion to NOz and subsequent removal by dry or wet deposition, results in a decrease of the global ozone production. This thesis investigates atmospheric levels, lifetimes and production rates of different NOy species in the field using thermal dissociation cavity ring-down spectroscopy (abbreviated as TD-CRDS). Results using existing instruments and an instrument developed in the frame of this work are presented.

The first chapter reports the current knowledge on NOy chemistry and describe the research objectives of this work. Chapter 2 describes the design and performances of a newly developed 5 channel TD-CRDS based instrument to measure NO_2, NO_3, N_2O_5, the sum peroxy nitrates (ΣRO_2NO_2, abbreviated as ΣPNs) and the sum of alkyl nitrates ($\Sigma RONO_2$, abbreviated as ΣANs). We show that this method allows for precise measurement of those reactive nitrogen species at high time resolution and with a good accuracy. A number of design improvements compared to previously developed similar instruments which reduce the measurement uncertainties and facilitate field deployment are detailed.

Chapter 3 reports field observations during two campaigns that took place in 2011 and 2015 on top of the “Kleiner Feldberg” mountain near Frankfurt am Main (Germany). NO_3 mixing ratios and estimated lifetimes are analysed in regard to meteorological and chemical influences. It is demonstrated that the measurement site is occasionally sampling from the nocturnal residual layer which result in very high steady state NO_3 lifetimes (up to 1 hour) which is unusual for ground based measurements. The estimated lifetimes assuming steady state are compared to the NO_3 reactivity calculated using VOCs measurements (by GC-FID and GC-MS) and NO measurements (by CLD) and significant discrepancies are found. An unaccounted source of NO_3 through the oxidation of NO_2 by Stabilized Criegee Intermediates (SCIs) as well as the influence of the local topography are considered as the potential causes

of the observed differences. In this chapter are also reported the measured mixing ratios and calculated production rates of organic nitrates during both campaign. The differences in lifetimes between OH and NO_3 generated organic nitrates are discussed. The nitrogen partitioning ratio between organic nitrates (ΣPNs + ΣANs) and NOx is reported and found to depend on NOx and temperature and to be as high as 80 % in aged, warm air masses. Finally the effective yield of alkyl nitrates for the PARADE campaign is estimated using O_3 and ΣANs mixing ratios and is found to match well the calculated yield based on VOCs measurements and individual alkyl nitrates yields reported in the literature.

The general conclusions of this work are presented in Chapter 4.

Zusammenfassung

Reaktive Stickstoffverbindungen, sogenannte NOy, sind eine Klasse von Stoffen, die in verschiedenen atmosphärischen Kreisläufen die globale Verteilung von Spurengasen beeinflussen. Die Gruppe der NOz, gebildet aus NOx ($NO+NO_2$), beinhaltet kurzlebige Verbindungen wie z.B. NO_3, HONO, RO_2NO_2, $ClNO_2$ aber auch langlebigere Verbindungen wie N_2O_5, HNO_3, $R(O)O_2NO_2$ and $RONO_2$. Das Schicksal von NOy (NOx+NOz) in der niedrigsten Schicht der Atmosphäre, der sogenannten Grenzschicht (boundary layer), hat einen starken Einfluss auf Ozon Mischverhältnisse, auf HOx Verbindungen ($OH+HO_2+RO_2$) und auf die Zusammensetzung von Aerosolen. Von der Photolyse von NO2 abgesehen, die zur Bildung von NO führt, führen die Zersetzung von NOx sowie die die Umwandlung zu NOz und der nachfolgende Entzug aus der Atmosphäre durch trockene oder nasse Ablagerung zu einem Absinken der globalen Ozon Produktion. Diese Doktorarbeit untersucht die atmosphärischen Konzentrationen, Lebenszeiten und Produktionsraten von verschiedenen NOy Verbindungen mit einer 5 Kanal, Laserabsorption Methode (Thermal Dissociation Cavity Ring-Down Spectroscopy (TD-CRDS)) in Feldmessungen. Die Ergebnisse unter Verwendung eines bereits existierenden, sowie eines neu entwickelten Instruments, werden im Rahmen dieser Arbeit präsentiert.

Das erste Kapitel legt das derzeitige Wissen über NOy Chemie dar und beschreibt die Forschungsziele dieser Arbeit. Das zweite Kapitel beschreibt den Aufbau und die Leistung des neu entwickelten TD-CRDS um NO_2, NO_3, N_2O_5 sowie die Summe der Peroxynitrate (ΣRO_2NO_2) und die Summe der Alkylnitrate ($\Sigma RONO_2$) zu messen. Wir demonstrieren, dass diese Methode genaue Messungen von reaktiven Stickstoffverbindugen mit guter Zeitauflösung und hoher Genauigkeit erlaubt. Weiterhin werden einige Verbesserungen zu bisher entwickelten Instrumenten aufgezeigt, welche Unsicherheiten in den Messungen reduzieren und gleichermaßen die Verwendung dieser Instrumente in Feldexperimenten erleichtern.

In Kapitel 3 wird von 2 Feldmesskampagnen berichtet, die 2011 und 2015 auf dem Plateu des kleinen Feldbergs in der Nähe von Frankfurt (Deutschland) stattfanden. Im ersten Teil wird das Verhalten von NO_3 Mischverhältnissen und Lebenszeiten mit Hinsicht auf meterologische und chemischen Einflüsse analysiert. Es wird gezeigt, dass dieser Messort gelegentlich Luftmassen aus der nächtlichen Restschicht (nocturnal residual layer) erhält, was zu sehr langen steady state NO_3 Lebenszeiten (bis zu einer Stunde) führt, wie sie für

bodenbasierte Messungen sehr ungewöhlich sind. Die steady state Lebenszeiten werden Reaktivitäten, berechnet aus VOC-Messungen (durch GC-FID und GC-MS) und NO Messungen (durch CLD), verglichen und es werden signifikante Unterschiede gefunden. Die Oxidation von NO_2 durch stabilisierte Criegee Intermediate (SCIs) als Quelle von NO_3 aber auch der Einfluss der lokalen Toopographie werden als mögliche Gründe für die beobachteten Unterschiede zwischen steady State und berechneten NO_3 Lebenszeiten angenommen. In diesem Kapitel werden auch die gemessenen Mischverhältnisse und berechneten Produktionsraten von organischen Nitraten während der beiden Kampagnen beschrieben. Es werden zudem die unterschiedliche Lebensdauer dieser organischen Nitrate in Abhängigkeit ihrer Bildung durch OH oder NO_3 diskutiert. Die Daten zeigen, dass die organische Nitrate bis 80 % der NO*x* Konzentration erreichen kann und dass die Partitionierung von [NO*x*] und von der Temperatur abhängig ist. Zuletzt wird die effektive Ausbeute von Alkylnitraten für die PARADE Kampagne, auf Grundlage der Ozon und $RONO_2$ Mischverhältnisse, geschätzt. Diese steht in guter Übereinstimmung mit den berechneten Ausbeuten basierend auf den VOC Messungen und individuellen Alkylnitratausbeuten wie in der Literatur beschrieben.

Die Schlussfolgerungen dieser Arbeit, sowie ein Ausblick und weitere mögliche Ansätze für zukünftige Arbeiten werden in Kapitel 4 beschrieben.

Chapter 1

Introduction

1.1. Planetary boundary layer chemistry and air quality in the modern era

The planetary boundary layer (PBL) is the part of the atmosphere that is the most strongly impacted by the earth surface activities. Ground emissions of trace gases can be related to anthropogenic or biogenic activities. Since the beginning of the industrial era, the anthropogenic emissions of nitrogen, sulphur, organic compounds and particulate matter have increased significantly leading to strong changes in chemical cycles and trace gas composition of the atmosphere (Muller, 1992). A lot of those anthropogenic sources are concentrated in urban and/or industrial areas in the Northern hemisphere. The increase of NOx ($NO + NO_2$) and volatile organic compounds (VOCs) emissions in those areas has lead to a strong global degradation of the air quality. The interaction between increased NOx and VOCs levels and sunlight has drastically increased tropospheric O_3 levels (Lelieveld and Dentener, 2000;Haagensmit and Fox, 1956) and lead to episodic strong pollution events ("photo-smog") in big cities (Haagensmit, 1952) . The boundary layer O_3 increase has a strong impact on human health and on the rest of the biosphere, for example decreasing crops yields and damaging the natural flora through leave surface degradation. The photo-smog (referring to a highly concentrated mixture of NOx, O_3, reactive nitrogen oxides, peroxides and fine particulate matter) has had similar effects on the biosphere (Haagensmit et al., 1952). Improving air quality in urban and semi-urban environment remains a challenge in European and North-American countries and a crucial priority in rapidly developing countries whose economies are based on high fossil fuel consumptions. Besides being involved in the degradation of urban areas air quality, NOx emissions can impact regions remote from any anthropogenic activities through long range transport of NOx reservoire species that act as sources of NOx in the absence of direct, ground emissions.

The mitigation of anthropogenic NOx and VOCs emissions is considered as the main solution to reduce ozone and reactive nitrogen oxides production in the boundary layer (Finlayson-Pitts and Pitts, 1977) but requires a deep knowledge of the complex chemical interactions between both groups of species. The day-time production of boundary layer O_3

and reactive nitrogen oxides is the result of the oxidation of VOCs by the hydroxyl radical (OH) followed by reaction with NOx (Levy, 1971). This chemical system is strongly influenced by the amount of NOx available and by the NO to NO_2 ratio. Close from NO sources, ambient mixing ratios of O_3 remains low due to its rapid reaction with NO to form NO_2 and O_2 (R1.1). Under very high [NO_2] conditions, this one acts as a strong sink of OH and thus limits the production of organic radicals. When NO_2 is present in lower amounts, the reaction between OH and VOCs leads to the production of O_3 and organic nitrogen species. Under very low [NOx] conditions, the reaction between OH and VOCs ultimately leads to the destruction of O_3. Those different regimes and the corresponding dominating reactions are described in the following sections.

1.2. NOx emissions

Overall more than 90% of the NOx is emitted as NO (Finlayson-Pitts and Pitts, 1999). In the PBL, a significant fraction of NO is very rapidly converted after emission to NO_2 through reaction with O_3 (R1.1) which is why NO sources are generally considered as NOx sources.

$$NO + O_3 \rightarrow NO_2 + O_2 \qquad \text{(R1.1)}$$

The main tropospheric source of NO is combustion of fossil fuels or biomass according to the Zeldovitch process described by reactions R1.2 to R1.4 (Zel'dovich and Raizer, 1966)

$$O_2 \rightarrow 2O \qquad \text{(R1.2)}$$

$$O + N_2 \rightarrow NO + N \qquad \text{(R1.3)}$$

$$N + O_2 \rightarrow NO + O \qquad \text{(R1.4)}$$

This process explains the production of NO by combustion engines, fossil fuel consuming power plants and biomass burning. The two first sources are purely anthropogenic while biomass burning also occurs as a natural phenomenon. The second most important source of NOx is soil emission following the denitrification process. This one correspond to the transformation of nitrates present in the ground to more reduced and volatile nitrogen

compounds (like N_2O, NO, N_2) as part of the respiration mechanism of some micro-organisms. This process occurs in natural soils and is intensified in agricultural soils by the use of fertilizers which increases the amount of nitrates available. Two minor sources of NOx in the troposphere are aircraft emissions and lightning which inject NOx directly at higher altitude. The global emission rates for the different sources described above for the decade 2000-2010 are given in Table 1 and correspond to values recommended by the IPCC (IPCC, 2013).

Table 1. Emission rates of NOx for the decade 2000-2010 as recommended by the last IPCC report (in TgN yr^{-1}).

Source	**Emission rate**	**Estimation range**
Fossil fuel combustion and industrial processes	28.3	-
Biomass and biofuel burning	5.5	-
Agriculture	3.7	
Aircrafts	-[a]	-
Natural soils	7.3	5-8
Lightning	4	3-5
Total	48.8	45.5-50.5

[a] the aircraft emissions are taken into account in the industrial processes value

According to those estimations, the annual, global emission rate of NOx is 48.8 TgN yr^{-1} for the previous decade. This value can be compared with pre-industrial estimations of 12 TgN yr^{-1} (Galloway et al., 2004) which shows the importance of industrial development on NOx emissions. Even though NOx emissions have stopped increasing in some regions thanks to emissions mitigation policies, the global annual emission rate is still on a raising slope. The estimations for the evolution of NOx emissions vary widely depending on the society evolution scenario considered. A conservative estimation (SRES A2 scenario (IPCC, 2013)), accounting for weak mitigation policies plans on an increase of NOx global emission rate up to 100 TgN yr^{-1} in 2100 (Lamarque et al., 2005).

1.3. VOC emissions

The most abundant VOC in the atmosphere is methane, whose concentration in the troposphere is very homogenous and is about 1.8 ppm and global annual emissions approximately 600 Tg(CH_4) yr^{-1} (top-down estimation (Prather et al., 2012)). Non-methane VOCs (NMVOCs) represent a large number of species which makes global emission rates estimation very challenging. On a global scale, continental biogenic sources of NMVOCs are dominating over anthropogenic sources with respective estimated annual emission rates of ≈ 650 TgC yr^{-1} and ≈ 100 TgC yr^{-1} for the decade 1980 to 1990 according to Muller (1992). Those estimations present high uncertainties due to the strong inter-annual emissions variability (especially regarding biogenic sources). Guenther et al. (1995) give a higher estimation of 1200 TgC yr^{-1}. According to this work, nearly half of the NMVOCs emission is due to isoprene (44%). This compound is mostly emitted by deciduous trees and is thus present at high mixing ratios in tropical and tempered forested areas and at lower mixing ratios in boreal regions. Another important class of biogenic VOCs (BVOCs) are terpenes (mono- and sesquiterpenes) that are important reaction partners of NO_3. Anthropogenic NMVOCs are mostly represented by the alkanes, alkenes and polycyclic aromatic hydrocarbons (PAHs) groups Overall, double bonded VOCs (of biogenic or anthropogenic origins) have higher reaction rate constant with OH and NO_3 and their oxidation might result in the formation of multifunctional compounds (Atkinson and Arey, 2003).

1.4. Day-time fate of NOx

During the day, the fate of NOx is strongly controlled by photochemistry. The OH radical is responsible, directly or indirectly, for the oxydation of NOx to higher oxides that are ultimately removed from the atmosphere by dry or wet deposition or transfer to aerosol particles (Badr and Probert, 1993;Nielsen et al., 1996). In the presence of only NO and NO_2 and sunlight, those two species are in photochemical equilibrium with O_3 which results from Leighton cycle (R1.5 to R1.7).

$$NO_2 + h\nu\ (\lambda < 420\ nm) \rightarrow NO + O \quad \text{(R1.5)}$$

$$O + O_2 + M \rightarrow O_3 + M \quad \text{(R1.6)}$$

$$NO + O_3 \rightarrow NO_2 + O_2 \quad \text{(R1.7)}$$

The photolysis of NO_2 in this cycle does not represent a net source of O_3 since the NO produced in the same time as the O atom converts O_3 back into NO_2. Deviations from the photo-stationary state occur under very polluted conditions typically close from NO sources or in the presence of high level of peroxy radicals that reacts with NO (R1.10). The built up of O_3 downwind or urban areas is due to the oxidation of NO to NO_2 by organic radicals. The day-time organic radical chemistry is initiated by the oxidation of VOCs by the OH radical. It proceeds either by H atom abstraction or by additions to a double bond. Those two mechanisms (R1.8 and R1.9) both result in the production of a peroxy radical.

$$OH + RH\ (+O_2) \rightarrow\ RO_2 +\ H_2O \qquad \text{(R1.8)}$$

$$RR' + OH\ (+O_2) \rightarrow\ ROHR'O_2 \qquad \text{(R1.9)}$$

$$RO_2 + NO \rightarrow\ RO + NO_2 \qquad \text{(R1.10)}$$

$$ROHR'O_2 + NO \rightarrow\ ROHR'O + NO_2 \qquad \text{(R1.11)}$$

In the presence of peroxy radicals, NO is oxidized to NO_2 and an alkoxy radical is produced (R1.10 and R1.11). This radical then reacts with O_2 to form HO_2 and a carbonyl compound (multi-substituted when the initial VOC contains a double bond). The OH radical consumed by reactions R1.8 and R1.9 is recycled by reaction between HO_2 and NO which produces NO_2 and OH. Following this NO_2 production process, its photolysis results in the net production of O_3. Under very low NOx concentration, the radical chemistry is terminated by reaction between RO_2 and RO_2 or HO_2 which forms peroxides or between O_3 and HO_2.

The local production of O_3 by those mechanisms is limited by the conversion of NOx to NOy species. One of the strongest sink of NO_2 is the direct reaction with OH that produces an HNO_3 molecule (R1.12).

$$NO_2 + OH\ \rightarrow\ \ HNO_3 \qquad \text{(R1.12)}$$

$$RO_2 + NO + M \rightarrow\ RONO_2 +\ M \qquad \text{(R1.13)}$$

$$R(O)O_2 + NO_2 + M \rightarrow\ RO(O_2)NO_2 +\ M \qquad \text{(R1.14)}$$

$$RO_2 + NO_2 + M \rightarrow\ RO_2NO_2 +\ M \qquad \text{(R1.15)}$$

When $[NO_2]$ is very high in comparison with VOCs mixing ratios, this reaction stops the production of organic radicals by neutralizing OH. In dry conditions, HNO_3 is very long lived and is lost to deposition on the ground. It is rapidly washed out of the atmosphere in

foggy/rainy conditions due to its very high solubility. Another important loss process of NOx is by the formation of organic nitrates. The reaction between peroxy radicals and NO results mainly in the formation of NO_2 (R1.10, R1.11). A minor branch of this reaction (R1.13) results in the formation of alkyl nitrates ($RONO_2$) (Atlas, 1988;Flocke et al., 1991) with a yield comprised between 1 and 30 % (Perring et al., 2013). Those compound are primarly formed in a excited state which can then undergo collisional deactivation with a third body. For this reason, the alkyl nitrate yield is positively correlated with pressure and the lengh of the carbon chain and negatively correlated with temperature. The oxydation of aldehydes by OH leads to the formation of acyl-peroxy radicals that reacts with NO_2 (R1.14) to form peroxyacyl nitric anhydrides ($R(O)O_2NO_2$, also called peroxyacyl nitrates or PANs) (Roberts, 1990) . The most abundant PANs is the peroxyacetyl nitrate which is one of the major species responsible for the toxicity of the photo-chemical "smog" phenomenon. NO_2 can also react with simple peroxy radical (R1.15) but the reaction products, non-acyl peroxy nitrates (RO_2NO_2) are very short lived compared to the peroxyacyl nitrates and represent a significant fraction of NOy only in the coldest regions of the troposphere (Browne et al., 2011;Murphy et al., 2004;Nault et al., 2015)

1.5. Night-time fate of NOx

During the night, the absence of OH and HO_2 leads to a different radical chemistry. After emission by anthropogenic or biogenic sources, NO reacts with O_3 but is not reformed by photolysis of NO_2 which results in decaying mixing ratios downwind of source areas. The oxidation of NO_2 by O_3 leads to the formation of the nitrate radical NO_3 (R1.15). In the absence of NO or sunlight, NO_3 mixing ratios can build up to detectable amounts (otherwise converted back to NO_2 (R1.17, R1.18a and R1.18b). The nitrate radical is a very reactive species with a lifetime that varies between few seconds up to several tens of minutes. It is the main night-time VOCs oxidants and initiates night-time radical chemistry (Platt et al., 1980;Wayne et al., 1991;Atkinson and Arey, 2003). While its reaction rate constants with saturated VOCs are very low, its reactions rate constants with alkenes and BVOCs are very high and for some VOCs, higher than the reaction rate constants with OH. The oxidation of double bonded VOCs by NO_3 proceeds by addition to the double bond which leads to the formation of a nitroperoxy radical (R1.19). At the difference of the peroxy radical formed by the oxydation of VOCs by OH, the nitrated peroxy radical is not lost by reaction with NO

since NO_3 is present only under small/negligible [NO] conditions. The sinks of this nitroperoxy radical are reaction with NO_3, HO_2, or RO_2 to form multi-functionnal alkyl nitrates (dinitrates, nitrates containing a hydroperoxy- or peroxy- group). The alkyl nitrate yields via NO_3 oxidation are significantly higher (20-80%) than via OH oxidation (1-30%) (Perring et al., 2013).

$$NO_2 + O_3 \rightarrow NO_3 + O_2 \quad \text{(R1.16)}$$

$$NO_3 + NO \rightarrow 2NO_2 \quad \text{(R1.17)}$$

$$NO_3 + h\nu \rightarrow NO + O_2 \quad \text{(R1.18a)}$$

$$\rightarrow NO_2 + O \quad \text{(R1.18b)}$$

$$R = R' + NO_3 + O_2 \rightarrow R(ONO_2)R'O_2 \quad \text{(R1.19)}$$

$$NO_2 + NO_3 + M \rightarrow N_2O_5 + M \quad \text{(R1.20)}$$

$$N_2O_5 + M \rightarrow NO_2 + NO_3 + M \quad \text{(R1.21)}$$

The formation of NO_3 by NO_2 leads to the simultaneous formation of dinitrogen pentoxide (N_2O_5) (R1.20). Its decomposition rate constant that is strongly depending on temperature, which makes that, in boundary layer conditions, NO_2, NO_3 and N_2O_5 are in equilibrium (according to R1.20 and R1.21). N_2O_5 radical is mostly lost by hydrolysis both in the gas phase (minor process) and on aerosol particles surface (major process). Because of the thermal equilibrium involving NO_3 and N_2O_5, losses of N_2O_5 indirectly act as removal processes for NO_3 and the reciproque is also true. The heterogeneous hydrolysis of N_2O_5 results mainly in the formation NO_3^- in the condensed phase and eventually to the further release of HNO_3. In the case where the aerosol particles contain chlorine ions, the hydrolysis of N_2O_5 can results in the release of ClNO2 in the gas phase whose main removal pathway is photolysis (Bertram and Thornton, 2009).

1.6. Research work and objectives

As already mentioned above, nitrogen oxides play an important role on the global repartition of nitrogen in the troposphere. At a local level, the partitioning of nitrogen species between short and long lived nitrogen compounds plays a role on the loss rate of NOx and on its transport downwind. It is therefore crucial to understand and quantify the production and removal rate of those species as well as the cycling between the different types of nitrogen

oxides. The boundary layer dynamic plays an important role in the transport/removal of reactive nitrogen oxides. During the day, ground heating results in the vertical mixing of ground emitted NOx and VOCs which leads to small vertical gradients in those species mixing ratios and chemical reactivity. During the night, the mixing intensity is strongly reduced which leads to a non homogeneity in terms of mixing ratios and lifetimes. One of the objectives of this work is to better understand what controls NO_3 and N_2O_5 lifetimes. In this optic, it is important to access laboratory determined reaction rates constants between NO_3 and VOCs (which controls NO_3 lifetimes) against field measurements. The same apply for the uptake coefficient of N_2O_5 to the aerosol particles, which is especially difficult to determine in the field due to the influence of a wide number of parameters on this value. As stated above, the reduction of mixing process intensity during the night when NO_3 and N_2O_5 are present makes it difficult to evaluate the conversion efficiency of NO_2 due to vertical gradients in mixing ratios and reactivity. The dependency of altitude on NO_3 and N_2O_5 mixing ratios and lifetimes is examined using data obtained during the PARADE field campaign in 2011 on top of a small mountain near Frankfurt am Main (Germany) (see Chapt. 2).

The wide variety of organic nitrates present in the atmosphere makes the observation of their mixing ratios very challenging. One aim of this work is understanding which role those species are playing in term of transport of NOx and what controls their mixing ratios in the boundary layer. The importance of those species in regard to the partitioning of nitrogen between them and NOx is examined . The day-time and night time production rates of alkyl nitrates ($RONO_2$) are compared using measured VOCs mixing ratios and literature reported yields of alkyl nitrates. Those results are used to make assumptions on the lifetimes of OH and NO_3 generated alkyl nitrates. The data used for this were obtained during the PARADE field campaign (2011) and during the NOTOMO campaign which took place at the same location (2015).

The in-situ measurement of the different NOy species described before is challenging due to the very high reactivity of NO_3 and N_2O_5 toward surfaces which leads to significant losses in measure instruments. NO_2 and organic nitrates are less reactive but represent all together a very wide range of species. For this reason measurements by mass spectrometry, which require calibration against standard samples, are rarely able to account for the atmospheric variety of those components. Recent developments in cavity enhanced based spectroscopy technique allow for the direct detection of NO_3 and NO_2 (Zalicki, 1994;Brown et al., 2002;Mazurenka et al., 2003). An objective of this work is to use the TD-CRDS method

to detect N_2O_5 and organic nitrates, respectively as NO_3 and NO_2 together with those species. Two existing instruments were used during the PARADE campaign (Schuster et al., 2009;Thieser et al., 2016), while a third instrument which was developed in the course of this work was used during the NOTOMO campaign. Figure 1 summarizes the important nitrogen oxides chemistry described in the introduction section. All 5 species or group of species that are measured by the cited TD-CRDS instruments are circled in red which shows the good coverage of the overall gas phase nitrogen oxides chemistry.

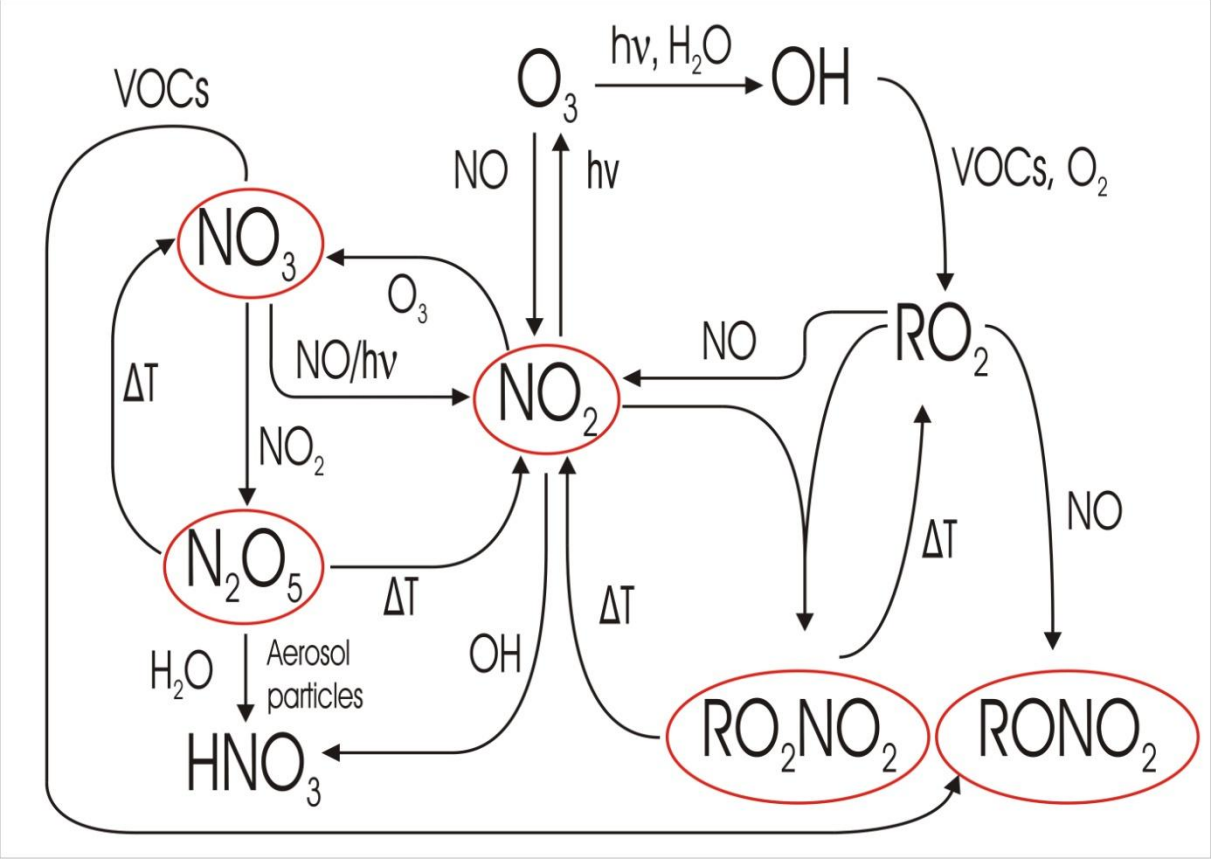

Figure 1. Atmospheric sources and sinks of the NOy species (in red circles) measured by the TD-CRDS instruments deployed during the PARADE and NOTOMO campaigns (2011 and 2015) and their link to VOC degradation and photochemical O_3 formation.

Chapter 2

Instrumentation and campaigns overview

2.1. The thermal dissociation cavity ring-down spectroscopy technique

The instrument developed during this project is based on previous instruments described in (Schuster et al., 2009) and (Thieser et al., 2016). It comports significant improvements compared to those ones in term of design, measurement accuracy and signal quality. A schematic of this newly developed instrument is shown on Fig. 2.

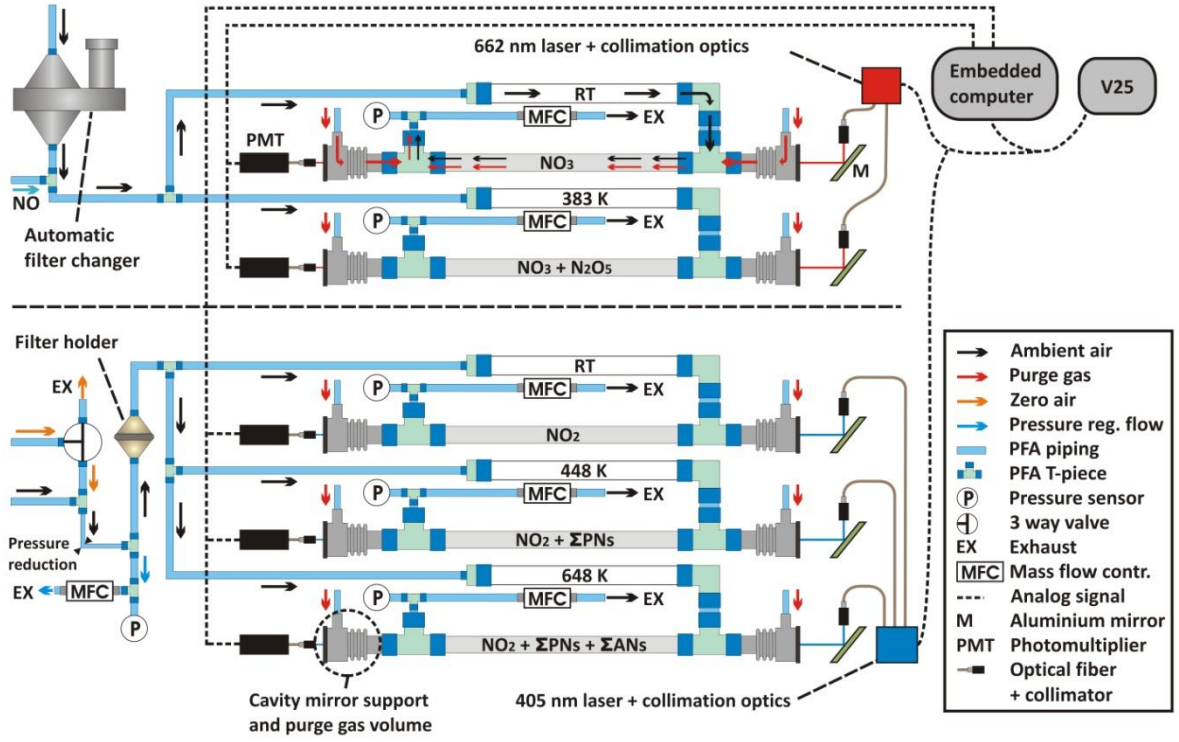

Figure 2. Schematic of the 5 channel TD-CRDS instrument developed in the frame of this thesis project.

The three instruments mentioned above are based on the cavity ring-down method that allows for the detection of NO_3 and NO_2 using their high absorption cross section at 662 nm ($\sigma(NO_3)_{662}$ = 2.3 x 10^{-17} cm^2 $molecule^{-1}$ at room temperature (Osthoff et al., 2007)) and 405 nm ($\sigma(NO_2)_{405}$ = 6 x 10^{-19} cm^2 $molecule^{-1}$ at room temperature (Voigt et al., 2002))

respectively. In both cases, the basis of this method consists in coupling a collimated laser beam into an optical cavity that is made of two highly reflective mirrors (R > 0.9999) and a 50 to 100 cm long cylinder. Once the light source is turned off, the light intensity profile detected behind the back mirror takes the shape of an exponential decay whose decay constant depends on the sampled air absorbance and on the mirrors reflectivity. The concentration of the absorbing species (in this case NO_3 or NO_2) is then deduced from the decay constant as shown by Eq.(1) where k is the decay constant in the presence of NO_3 or NO_2 and k_0 is the decay constant obtained when NO_3 or NO_2 are not present in the cavity.

$$[X] = \frac{1}{c\sigma(X,\lambda)}(k - k_0) \qquad \text{Eq.(1)}$$

The detection of N_2O_5 and organic nitrates in the newly developed, 5 channel TD-CRDS, is described hereafter. N_2O_5 is thermally decomposed at 383 K to form one NO_3 and one NO_2 according to reaction R(1.21). N_2O_5 is then detected as NO_3 and the mixing ratio of N_2O_5 obtained by subtraction between the ambient NO_3 signal and the NO_3 + N_2O_5 signal. Those two signals are measured simultaneously in two different cavities. In a similar way, a third cavity detects ambient NO_2, while a fourth one detects the sum of ambient NO_2 plus NO_2 coming from the decomposition of PNs at 448K according to (R2.1) with a yield approximately equal to one. In the fifth channel, the sum of NO_2, NO_2 resulting from PNs decomposition and NO_2 resulting from the decomposition of ANs (R2.2) is measured. The mixing ratio of PNs and ANs are then deduced by subtraction operations between the three 405 nm NO_2 detecting channels.

$$R(O)O_2NO_2 + M \rightarrow R(O)O_2 + NO_2 \qquad \text{(R2.1)}$$

$$RONO_2 + M \rightarrow RO + NO_2 \qquad \text{(R2.2)}$$

The data obtained using this instrument need to be corrected for different optical and chemical biases arising from the design of the instrument, from the presence in ambient air of species that acts as source or sinks of NO_2 during the sampling time and for radical losses to the instrument piping walls. A more detailed description of the instrument design, characteristics and data corrections is given in Appendix A1.

2.2. Field campaigns description

The three TD-CRDS instruments cited in the previous section were deployed during two field campaigns that took place at the Taunus Observatory station on Top of the Kleiner Feldberg mountain, 20 km north-west of Frankfurt am Main. A topographic map of this site is shown in Fig. 3.

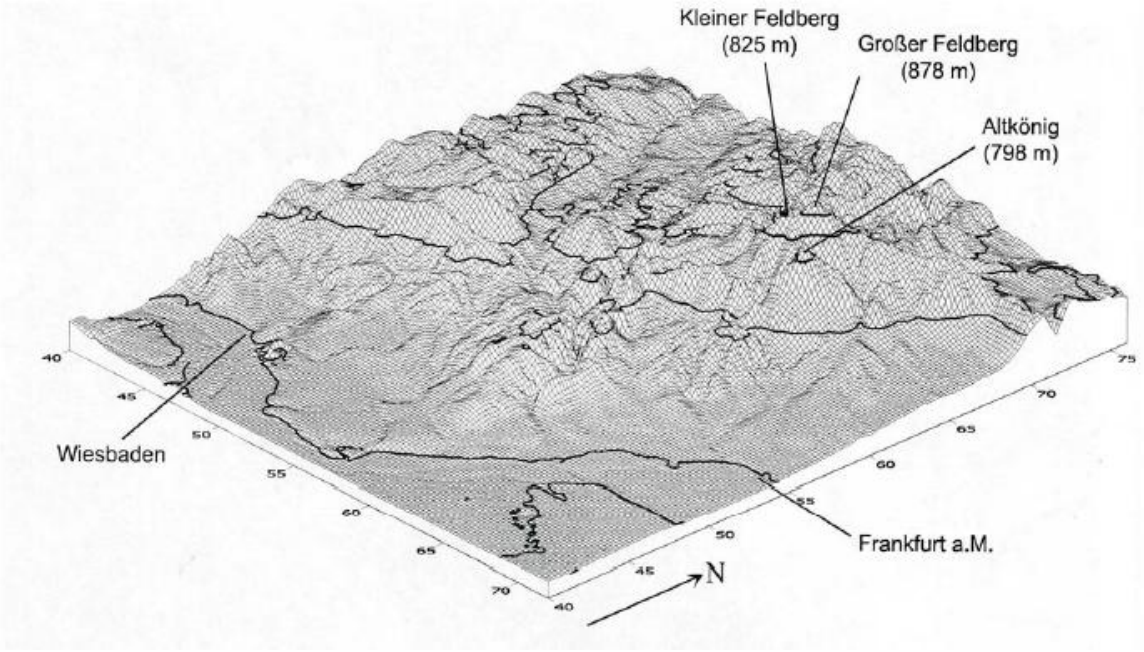

Figure 3. Topographic map of the region including the site where the PARADE and NOTOMO campaigns took place (taken from Handisides (2001))

This site is interesting for the observation of NOx/VOCs interaction due to its geographical situation. It is both impacted by anthropogenic emissions of NOx and anthropogenic VOCs by the urban area to the south and south-west (Frankfurt, Mainz and Wiesbaden cities) and by local emissions of BVOCs by the surrounding forested area. On a regional scale, the site is both impacted by continental and marine air masses which offer an interesting contrast in term of air mass aging and marine species loading.

The PARADE campaign (PArticles and RAdicals: Diel observations of the impact of urban and biogenic Emissions) took place in August-September 2011 during which were measured, together with the NOy species by TD-CRDS, a large suite of VOCs by gas chromatography techniques, $ClNO_2$ was measured by CIMS and NO by CLD. The NOTOMO campaign (NOcturnal chemistry at the Taunus Observatory: insights into Mechanisms of

Oxidation) took place during July 2015 during which the same NOy species (with the exception of NO) were measured but no VOCs measurements were made. For both campaigns, the meteorological parameters were made available by the local air quality surveillance network (HLUG).

Chapter 3

Results

3.1. NO_3 reactivity and steady state lifetime

The steady state hypothesis was used to estimate NO_3 lifetime during the PARADE campaign. The estimation is based on the fact that, due to the high reactivity of the nitrate radical, its concentration reaches state state ($d[NO_3]/dt = 0$) downwind of its precursors emission sources. Using this approach, the steady lifetime of NO_3 was calculated using NO_2 and O_3 mixing ratios (defining its production rate). The steady state lifetime was compared to the NO_3 reactivity calculated with VOCs and NO mixing ratios and on N_2O_5 heterogeneous hydrolysis rate. Strong discrepancies between steady state and calculated reactivity were observed which are potentially arising from 1) very close VOCs emissions which strongly increase the local NO_3 reactivity and drive the concentration of NO_3 out of steady state. 2) unaccounted sources of NO_3. In this regard, the oxidation of NO_2 by stabilized criegee intermediates was examined as a potential source of NO_3. Details on those observations are given in Appendix B1.

3.2. Ground emissions, boundary layer dynamic and NO_3 lifetimes

Unusually long steady state lifetime values were observed during PARADE (up to 1h) which were due to down mixing of ground decoupled air masses or/and sampling from the nocturnal residual layer . During those long lifetime events, simultaneous changes in key meteorological parameters and some ground emitted trace gases were observed. The in-situ measurement of NO_3 by CRDS and the corresponding lifetimes were compared with LP DOAS measurements. A clear dependence of altitude on NO_3 mixing ratios and lifetime was observed which is likely due to vertical gradient on NO_3 reaction partners (mainly isoprene, monoterpenes and NO). Details on those observations are given in Appendix B1.

3.3. Organic nitrates to NOx nitrogen partitioning

The mixing ratios of total organic nitrates during the PARADE and NOTOMO campaigns were analysed in regard to meteorological and chemical factors. The partitioning ratio between organic nitrates (Org.) and NO_x (Org./(Org. + NOx) was calculated and found to be as high as 0.8. It was observed that the two main factors controlling this ratio are temperature/humidity and NOx level. It was speculated that temperature and humidity are influencing the emissions rate of organic nitrate precursors as well as their transfer rate to the aerosol particles phase and that the NOx dependence traduces its sources proximity and the chemical age of the air masses. Details on those observations are given in Appendix C.

3.4. Production rate of alkyl nitrates

The average noon time production rate of alkyl nitrates was calculated for the PARADE campaign using the measured VOCs concentrations, individual alkyl nitrates yields and calculated OH concentration. The night time production rate was calculated using NO_3 concentration instead of [OH]. Both values were very similar and approximately equal to 70 pptv hr^{-1}. The calculated production rates and ambient ΣANs mixing ratios were used to compare the lifetime of OH and NO_3 induced alkyl nitrates. The similar day- and night-time production rates associated with higher day-time [ΣANs] indicate that OH generated alkyl nitrates have longer lifetimes than NO_3 induced one. It was concluded that the higher degree of substitution of NO_3 induced ANs than the OH induced ones results in a lower volatility and a higher removal rate by deposition to the ground or transfer to the aerosol phase. Details on those observations are given in Appendix C.

3.5. Effective and calculated alkyl nitrates yield

Two methods to estimate the effective alkyl nitrate yield α (average yield corresponding to the ambient VOCs mixture) during the PARADE campaign were compared. The first method uses the correlation between measured [O_3] and [ΣANs] to estimate α. This method is based on the fact that the ratio between the production rates of those two species is directly proportional to α. When the loss rates of O_3 and ANs are negligible compared to their production rate (typically at noon time), α can be approximated by the slope corresponding to

a linear fit between [O_3] and [ΣANs]. Using this method, an average α of ≈ 7 % was obtained for the whole campaign. The second method uses measured VOCs mixing ratios and individual alkyl nitrates yield from the literature. Using this method, an α value of ≈ 6 % was calculated for the noon time period (11:00 – 13:00). Different sources of error on both methods were discussed to explain the observed differences. Details on those observations are given in Appendix C.

Chapter 4

Conclusions and outlook

The instrument developed in the frame of this work is well suited for field measurements. The improvements implemented compared to previous instrument using the same TD-CRDS detection method allow for a better accuracy and a lower detection limit. Its compact and robust design makes it easy to deploy in field conditions. The thermal dissociation method is a useful tool to measure the sum of organic nitrates that constitute an important member of the NOy family. All together, the five species or group of species that are measured by this instrument represent a significant fraction of the NOy. Further improvements on this instrument are possible and include: a space use optimization to make it suitable for aircraft deployment, a better coupling between the light sources and the cavities to lower further the detection limit and a better characterisation of the organic nitrates behaviour in the sampling lines using different alkyl nitrates standards. Inter comparison between this instrument and existing one using different detection methods is recommended especially regarding organic nitrates

The data obtained by the TD-CRDS method during two field campaigns coupled with meteorological parameter measurements, long range or in-situ measurement of other trace gases has given good indication on the reactive nitrogen chemistry in particular regarding their interaction with VOCs. It has been demonstrated that the measured reactive nitrogen species lifetimes are very variable and influenced by a number of chemical and meteorological factors that were well capture by the complementary measurement during the two campaigns. Further analysis on the interactions between NOy and VOCs include, for example, direct measurement of NO_3 reactivity and co-measurement of organic nitrates with a broader suite of VOCs.

References

Atkinson, R., and Arey, J.: Atmospheric degradation of volatile organic compounds, Chem Rev, 103, 4605-4638, Doi 10.1021/Cr0206420, 2003.

Atlas, E.: Evidence for Greater-Than-or-Equal-to-C-3 Alkyl Nitrates in Rural and Remote Atmospheres, Nature, 331, 426-428, Doi 10.1038/331426a0, 1988.

Badr, O., and Probert, S. D.: Oxides of Nitrogen in the Earths Atmosphere - Trends, Sources, Sinks and Environmental Impacts, Appl Energ, 46, 1-67, Doi 10.1016/0306-2619(93)90076-2, 1993.

Bertram, T. H., and Thornton, J. A.: Toward a general parameterization of N2O5 reactivity on aqueous particles: the competing effects of particle liquid water, nitrate and chloride, Atmos Chem Phys, 9, 8351-8363, 2009.

Brown, S. S., Stark, H., Ciciora, S. J., McLaughlin, R. J., and Ravishankara, A. R.: Simultaneous in situ detection of atmospheric NO3 and N2O5 via cavity ring-down spectroscopy, Rev Sci Instrum, 73, 3291-3301, Doi 10.1063/1.1499214, 2002.

Browne, E. C., Perring, A. E., Wooldridge, P. J., Apel, E., Hall, S. R., Huey, L. G., Mao, J., Spencer, K. M., St Clair, J. M., Weinheimer, A. J., Wisthaler, A., and Cohen, R. C.: Global and regional effects of the photochemistry of CH3O2NO2: evidence from ARCTAS, Atmos Chem Phys, 11, 4209-4219, DOI 10.5194/acp-11-4209-2011, 2011.

Finlayson-Pitts, B. J., and Pitts, J. N.: The Chemical Basis of Air Quality: Kinetics and Mechanisms of Photochemical Air Pollution and Application to Control Strategies, Wiley, 1977.

Finlayson-Pitts, B. J., and Pitts, J. N.: Chemistry of the Upper and Lower Atmosphere: Theory, Experiments, and Applications, Elsevier Science, 1999.

Flocke, F., Volzthomas, A., and Kley, D.: Measurements of Alkyl Nitrates in Rural and Polluted Air Masses, Atmos Environ a-Gen, 25, 1951-1960, Doi 10.1016/0960-1686(91)90276-D, 1991.

Galloway, J. N., Dentener, F. J., Capone, D. G., Boyer, E. W., Howarth, R. W., Seitzinger, S. P., Asner, G. P., Cleveland, C. C., Green, P. A., Holland, E. A., Karl, D. M., Michaels, A. F., Porter, J. H., Townsend, A. R., and Vorosmarty, C. J.: Nitrogen cycles: past, present, and future, Biogeochemistry, 70, 153-226, DOI 10.1007/s10533-004-0370-0, 2004.

Guenther, A., Hewitt, C. N., Erickson, D., Fall, R., Geron, C., Graedel, T., Harley, P., Klinger, L., Lerdau, M., Mckay, W. A., Pierce, T., Scholes, B., Steinbrecher, R., Tallamraju, R., Taylor, J., and Zimmerman, P.: A Global-Model of Natural Volatile Organic-Compound Emissions, J Geophys Res-Atmos, 100, 8873-8892, Doi 10.1029/94jd02950, 1995.

Haagensmit, A. J.: Chemistry and Physiology of Los-Angeles Smog, Ind Eng Chem, 44, 1342-1346, Doi 10.1021/Ie50510a045, 1952.

Haagensmit, A. J., Darley, E. F., Zaitlin, M., Hull, H., and Noble, W.: Investigation on Injury to Plants from Air Pollution in the Los-Angeles Area, Plant Physiol, 27, 18-34, Doi 10.1104/Pp.27.1.18, 1952.

Haagensmit, A. J., and Fox, M. M.: Ozone Formation in Photochemical Oxidation of Organic Substances, Ind Eng Chem, 48, 1484-1487, Doi 10.1021/Ie51400a033, 1956.

Handisides, G. M.: The influence of peroxy radicals on ozone production, Fachbereich Geowissenschaften, Johann Wolfgang Goethe Universität, Frankfurt am Main, 2001.

IPCC: Climate Change 2013: The Physical Science Basis. Contribution of Working Group I to the Fifth Assessment Report of the Intergovernmental Panel on Climate Change, Cambridge University Press, Cambridge, United Kingdom and New York, NY, USA, 1535 pp., 2013.

Lamarque, J. F., Kiehl, J. T., Brasseur, G. P., Butler, T., Cameron-Smith, P., Collins, W. D., Collins, W. J., Granier, C., Hauglustaine, D., Hess, P. G., Holland, E. A., Horowitz, L., Lawrence, M. G., McKenna, D., Merilees, P., Prather, M. J., Rasch, P. J., Rotman, D., Shindell, D., and Thornton, P.: Assessing future nitrogen deposition and carbon cycle feedback using a multimodel approach: Analysis of nitrogen deposition, J Geophys Res-Atmos, 110, Artn D1930310.1029/2005jd005825, 2005.

Lelieveld, J., and Dentener, F. J.: What controls tropospheric ozone?, J Geophys Res-Atmos, 105, 3531-3551, Doi 10.1029/1999jd901011, 2000.

Levy, H.: Normal Atmosphere - Large Radical and Formaldehyde Concentrations Predicted, Science, 173, 141-&, DOI 10.1126/science.173.3992.141, 1971.

Mazurenka, M. I., Fawcett, B. L., Elks, J. M. F., Shallcross, D. E., and Orr-Ewing, A. J.: 410-nm diode laser cavity ring-down spectroscopy for trace detection of NO2, Chem Phys Lett, 367, 1-9, Pii S0009-2614(02)01652-4 Doi 10.1016/S0009-2614(02)01652-4, 2003.

Muller, J. F.: Geographical-Distribution and Seasonal-Variation of Surface Emissions and Deposition Velocities of Atmospheric Trace Gases, J Geophys Res-Atmos, 97, 3787-3804, 1992.

Murphy, J. G., Thornton, J. A., Wooldridge, P. J., Day, D. A., Rosen, R. S., Cantrell, C., Shetter, R. E., Lefer, B., and Cohen, R. C.: Measurements of the sum of HO2NO2 and CH3O2NO2 in the remote troposphere, Atmos Chem Phys, 4, 377-384, 2004.

Nault, B. A., Garland, C., Pusede, S. E., Wooldridge, P. J., Ullmann, K., Hall, S. R., and Cohen, R. C.: Measurements of CH3O2NO2 in the upper troposphere, Atmos Meas Tech, 8, 987-997, 10.5194/amt-8-987-2015, 2015.

Nielsen, T., Pilegaard, K., Egelov, A. H., Granby, K., Hummelshoj, P., Jensen, N. O., and Skov, H.: Atmospheric nitrogen compounds: Occurrence, composition and deposition, Sci Total Environ, 189, 459-465, Doi 10.1016/0048-9697(96)05246-1, 1996.

Osthoff, H. D., Pilling, M. J., Ravishankara, A. R., and Brown, S. S.: Temperature dependence of the NO(3) absorption cross-section above 298 K and determination of the equilibrium constant for NO(3)+NO(2) <-> N(2)O(5) at atmospherically relevant conditions, Phys Chem Chem Phys, 9, 5785-5793, Doi 10.1039/B709193a, 2007.

Perring, A. E., Pusede, S. E., and Cohen, R. C.: An Observational Perspective on the Atmospheric Impacts of Alkyl and Multifunctional Nitrates on Ozone and Secondary Organic Aerosol, Chem Rev, 113, 5848-5870, Doi 10.1021/Cr300520x, 2013.

Platt, U., Perner, D., Winer, A. M., Harris, G. W., and Pitts, J. N.: Detection of No3 in the Polluted Troposphere by Differential Optical-Absorption, Geophys Res Lett, 7, 89-92, Doi 10.1029/Gl007i001p00089, 1980.

Prather, M. J., Holmes, C. D., and Hsu, J.: Reactive greenhouse gas scenarios: Systematic exploration of uncertainties and the role of atmospheric chemistry, Geophys Res Lett, 39, Artn L0980310.1029/2012gl051440, 2012.

Roberts, J. M.: The Atmospheric Chemistry of Organic Nitrates, Atmos Environ a-Gen, 24, 243-287, Doi 10.1016/0960-1686(90)90108-Y, 1990.

Schuster, G., Labazan, I., and Crowley, J. N.: A cavity ring down/cavity enhanced absorption device for measurement of ambient NO(3) and N(2)O(5), Atmos Meas Tech, 2, 1-13, 2009.

Thieser, J., Schuster, G., Schuladen, J., Phillips, G. J., Reiffs, A., Parchatka, U., Pöhler, D., Lelieveld, J., and Crowley, J. N.: A two-channel thermal dissociation cavity ring-down spectrometer for the detection of ambient NO2, RO2NO2 and RONO2, Atmos. Meas. Tech., 9, 553-576, 10.5194/amt-9-553-2016, 2016.

Voigt, S., Orphal, J., and Burrows, J. P.: The temperature and pressure dependence of the absorption cross-sections of NO2 in the 250-800 nm region measured by Fourier-transform spectroscopy, J Photoch Photobio A, 149, 1-7, Pii S1010-6030-(01)00650-5 Doi 10.1016/S1010-6030(01)00650-5, 2002.

Wayne, R. P., Barnes, I., Biggs, P., Burrows, J. P., Canosamas, C. E., Hjorth, J., Lebras, G., Moortgat, G. K., Perner, D., Poulet, G., Restelli, G., and Sidebottom, H.: The Nitrate Radical - Physics, Chemistry, and the Atmosphere, Atmos Environ a-Gen, 25, 1-203, 1991.

Zalicki, P.: Cavity ring-down spectroscopy for quantitative absorption measurements, American Institute of Physics, 1994.

Zel'dovich, Y. B., and Raizer, Y. P.: Physics Of Shock Waves and High-temperature Hydrodynamic Phenomena, Academic Press, 1966.

List of publications

As first author

Sobanski, N., Tang, M. J., Thieser, J., Schuster, G., Pöhler, D., Fischer, H., Song, W., Sauvage, C., Williams, J., Fachinger, J., Berkes, F., Hoor, P., Platt, U., Lelieveld, J., and Crowley, J. N.: Chemical and meteorological influences on the lifetime of NO_3 at a semi-rural mountain site during PARADE, Atmos. Chem. Phys., 16, 4867-4883, doi:10.5194/acp-16-4867-2016, 2016.

Sobanski, N., Schuladen, J., Schuster, G., Lelieveld, J., and Crowley, J. N.. A five-channel cavity ring-down spectrometer for the detection of NO_2, NO_3, N_2O_5, total peroxy nitrates and total alkyl nitrates, Atmos. Meass. Tech., 9, 1-16, doi: 10.5194/amt-9-1-2016, 2016. *Temporary reference issued from the final proofreadig version.*

Sobanski, N., Thieser J., Schuladen, J., Sauvage, C., Song, W., Williams, J., Lelieveld, J., and Crowley, J. N.. Day- and night- time formation of organic nitrates at a forested mountain-site in South-West Germany. *Submitted in Atmos. Chem. Phys. Discuss.*, 2016.

As co-author

Phillips, G. J., Makkonen, U., Schuster, G., Sobanski, N., Hakola, H., and Crowley, J. N.: The detection of nocturnal N_2O_5 as HNO_3 by alkali- and aqueous-denuder techniques, Atmos. Meas. Tech., 6, 231-237, doi:10.5194/amt-6-231-2013, 2013.

Phillips, G. J., Thieser, J., Tang, M. J., Sobanski, N., Schuster, G., Fachinger, J., Drewnick, F., Borrmann, S., Bingemer, H., Lelieveld, J., and Crowley, J. N.: Estimating N_2O_5 uptake coefficients using ambient measurements of NO_3, N_2O_5, $ClNO_2$ and particle-phase nitrate, Atmos. Chem. Phys. Discuss., doi:10.5194/acp-2016-693, *accepted for final publication*, 2016.

Appendix

Appendix A1

A 5-channel cavity ring-down spectrometer for the detection of NO_2, NO_3, N_2O_5, total peroxy nitrates and total alkyl nitrates

N. Sobanski[1], J. Schuladen[1], G. Schuster[1], J. Lelieveld[1] and J. N. Crowley[1]

[1]Atmospheric Chemistry Department, Max-Planck-Institut für Chemie, 5 55128 Mainz, Germany.

Atmos. Meas. Tech., 9, 1–16, 2016
www.atmos-meas-tech.net/9/1/2016/
doi:10.5194/amt-9-1-2016
© Author(s) 2016. CC Attribution 3.0 License.

Atmospheric Measurement Techniques
Open Access
EGU

A five-channel cavity ring-down spectrometer for the detection of NO_2, NO_3, N_2O_5, total peroxy nitrates and total alkyl nitrates

Nicolas Sobanski, Jan Schuladen, Gerhard Schuster, Jos Lelieveld, and John N. Crowley

Atmospheric Chemistry Department, Max-Planck-Institut für Chemie, 55128 Mainz, Germany

Correspondence to: John N. Crowley (john.crowley@mpic.de)

Received: 31 May 2016 – Published in Atmos. Meas. Tech. Discuss.: 14 June 2016
Revised: 22 September 2016 – Accepted: 29 September 2016 – Published:

Abstract. We report the characteristics and performance of a newly developed five-channel cavity ring-down spectrometer to detect NO_3, N_2O_5, NO_2, total peroxy nitrates (ΣPNs) and total alkyl nitrates (ΣANs). NO_3 and NO_2 are detected directly at 662 and 405 nm, respectively. N_2O_5 is measured as NO_3 after thermal decomposition at 383 K. PNs and ANs are detected as NO_2 after thermal decomposition at 448 and 648 K. We describe details of the instrument construction and operation as well as the results of extensive laboratory experiments that quantify the chemical and optical interferences that lead to biases in the measured mixing ratios, in particular involving the reactions of organic radical fragments following thermal dissociation of PNs and ANs. Finally, we present data obtained during the first field deployment of the instrument in July 2015.

1 Introduction

Nitrogen oxides play a central role in tropospheric chemistry though their influence on ozone production and radical cycling, and thus on the oxidative capacity of the atmosphere. Nitric oxide (NO) is directly emitted into the boundary layer by e.g. fossil fuel combustion and biomass burning, and is oxidised via various mechanisms (e.g. reaction with O_3 and peroxy radicals, RO_2) to form NO_2, which is the dominant precursor of photochemically formed, tropospheric ozone. Together, NO and NO_2 are referred to as NO_x, while the sum of all reactive, oxidised nitrogen species (NO_x plus inorganic and organic nitrates and nitrites and halogenated nitrogen oxides) is referred to as NO_y. In the tropospheric boundary layer, NO_2 mixing ratios vary from < 10 pptv in remote regions to > 100 ppbv in highly polluted environments. Tropospheric NO_2 has been measured using several techniques including differential optical absorption spectroscopy (DOAS), chemiluminescence (CLD), laser-induced fluorescence (LIF) and cavity ring-down spectroscopy (CRDS). For a summary and intercomparison of these methods, the reader is referred to Fuchs et al. (2010). NO_2 is the major precursor of the inorganic nitrates NO_3 and N_2O_5. During the daytime, NO_3 is rapidly photolysed (Johnston et al., 1996) and also reacts with NO to reform NO_2 so that NO_3 mixing ratios are very low. At night, NO_3 levels may reach hundreds of parts per trillion volume in polluted air, and their reactions represent a significant route for oxidation of volatile organic compounds (VOCs) and, via formation of N_2O_5, are a source of particulate nitrate and thus sink of NO_x (Wayne et al., 1991; Allan et al., 1999). Tropospheric NO_3 has been detected using long-path DOAS (LP-DOAS; Platt et al., 1980) over a path length of typically > 1 km, whilst point detection methods of NO_3 include cavity-enhanced DOAS-, LIF- and CRDS-based instruments. N_2O_5 has been detected as NO_3 after thermal decomposition or directly measured by chemical ionisation mass spectrometry. Descriptions of methods for detecting NO_3 and N_2O_5 and an intercomparison experiment have recently been published (Fuchs et al., 2012; Dorn et al., 2013).

Reactions between atmospheric oxidants such as OH or NO_3 and anthropogenic or biogenic volatile organic compounds (VOCs) lead to the formation of organic peroxy radicals that react with NO or NO_2 to form organic nitrates (Roberts, 1990a). Reaction of RO_2 with NO_2 results in the formation of peroxy nitrates (RO_2NO_2, henceforth abbreviated as PNs). If the initial peroxy radical contains a terminal acyl group ($R(O)O_2$), peroxyacetic nitric anhydrides (also called peroxyacyl nitrates or PANs, $R(O)O_2NO_2$) are

formed, which have lifetimes on the order of hours in temperate boundary layer conditions but weeks in cold regions of the atmosphere. Following generation and transport away from pollution sources, PANs can thermally decompose to NO_2 and an organic radical, thus providing NO_x and enhancing the production of O_3 in remote locations. Non-substituted peroxy radicals react to form PNs that are less thermally stable, which undergo rapid (timescale of seconds at 298 K) thermal decomposition in the mid-latitude boundary layer, and thus only reach higher concentrations in colder regions such as the upper troposphere and regions close to the poles (Slusher et al., 2002; Murphy et al., 2004). The reaction of RO_2 with NO mainly forms RO + NO_2, but can also result in the formation of alkyl nitrates ($RONO_2$, henceforth abbreviated as ANs) in a minor branch (1–30 %) of this reaction, with higher yields for long-chain peroxy radicals (Arey et al., 2001; Perring et al., 2013). ANs are also formed at night from the reaction between NO_3 and VOCs with a higher yield (20–80 %) than the OH-initiated process (Perring et al., 2013). The oxidation of alkenes by NO_3 results in the formation of nitroxy alkyl radicals that can react with O_2 to form nitroxy alkyl peroxy radicals that can undergo further chemistry. ANs are longer lived than PANs against thermal decomposition, and can thus also act as NO_x reservoirs. Reactions with OH or photolysis or transfer to the aerosol phase are the major sinks of ANs, the relative importance depending on carbon chain size and degree of substitution. PNs and ANs represent a very wide group of species present in the atmosphere, with different levels of structural complexity due to the different possible combinations of functional groups. Individual nitrates can be measured using chromatography-based instruments followed by electron capture detection, conversion to NO or NO_2 (Roberts et al., 1989; Roberts, 1990a; Flocke et al., 1991; Blanchard et al., 1993) or chemical ionisation mass spectrometry (Beaver et al., 2012), whereas the detection of the total (i.e. non-speciated) ambient PNs and ANs has been demonstrated using thermal decomposition of the nitrates followed by NO_2 detection (Day et al., 2002, 2003; Paul et al., 2009; Paul and Osthoff, 2010; Wooldridge et al., 2010; Thieser et al., 2016).

A single instrument that measures NO_2, NO_3, N_2O_5, total peroxy nitrates (ΣPNs) and total alkyl nitrates (ΣANs) can clearly provide great insight into the reactive nitrogen budget of the troposphere, enabling studies of daytime and night-time processes that transfer NO_x from the gas to the particle phase or to organic reservoir species. The interconversions and relation to NO_x losses and photochemical O_3 generation of these traces gases are described in Fig. 1, and those highlighted in red circles are detected with this instrument. The five-channel instrument we describe is a further development and extension of the two-channel, one-colour (405 nm) prototype recently described by Thieser et al. (2016) and of the two-channel set-up for measuring NO_3 and N_2O_5 previously developed and operated by this group

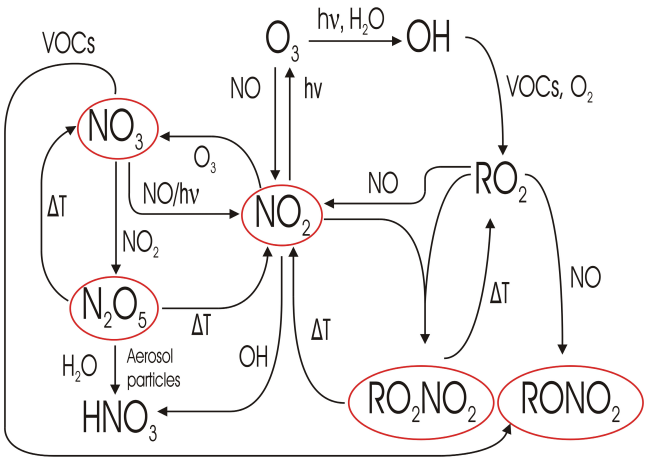

Figure 1. Atmospheric sources and sinks of the NO_y species (in red circles) measured by the five-channel TD-CRDS instrument described in this work and their link to VOC degradation and photochemical O_3 formation.

(Schuster et al., 2009). Whilst some basic concepts are similar, several significant design modifications (optical, mechanical, electrical/data-acquisition and chemical) have been made that improve the precision, the limit of detection and the accuracy of the measurements. These improvements are described in the relevant sections below.

In Sect. 2 we describe the overall design of the instrument and the features specific to the measurement of the individual trace gases. In Sect. 3 calibration procedures and laboratory characterisation experiments are described, along with an assessment of the overall uncertainty. Finally, in Sect. 4 we show data from a first field deployment at a semi-rural mountain site in Germany.

2 Instrument design

The instrument we describe uses cavity ring-down spectroscopy (CRDS), partly coupled with thermal dissociation (TD-CRDS). CRDS is a detection technique that was developed in the early 1990s (O'Keefe and Deacon, 1988; Lehmann and Romanini, 1996), and has been recently reviewed (Berden et al., 2000; Brown, 2003). The underlying principle of CRDS is the measurement of optical extinction in a (usually) closed cavity. In contrast to differential absorption spectroscopy in which optical extinction is linked to a measured light intensity difference, in CRDS set-ups, the optical extinction is calculated from the rate of decay of light intensity (ring-down constant) measured at the output of the cavity after a light pulse (pulsed CRDS) or after a continuous light source is turned off (cw-CRDS). The light intensity decay, measured behind a cavity mirror after switching the light source off, is exponential, and the concentration of an

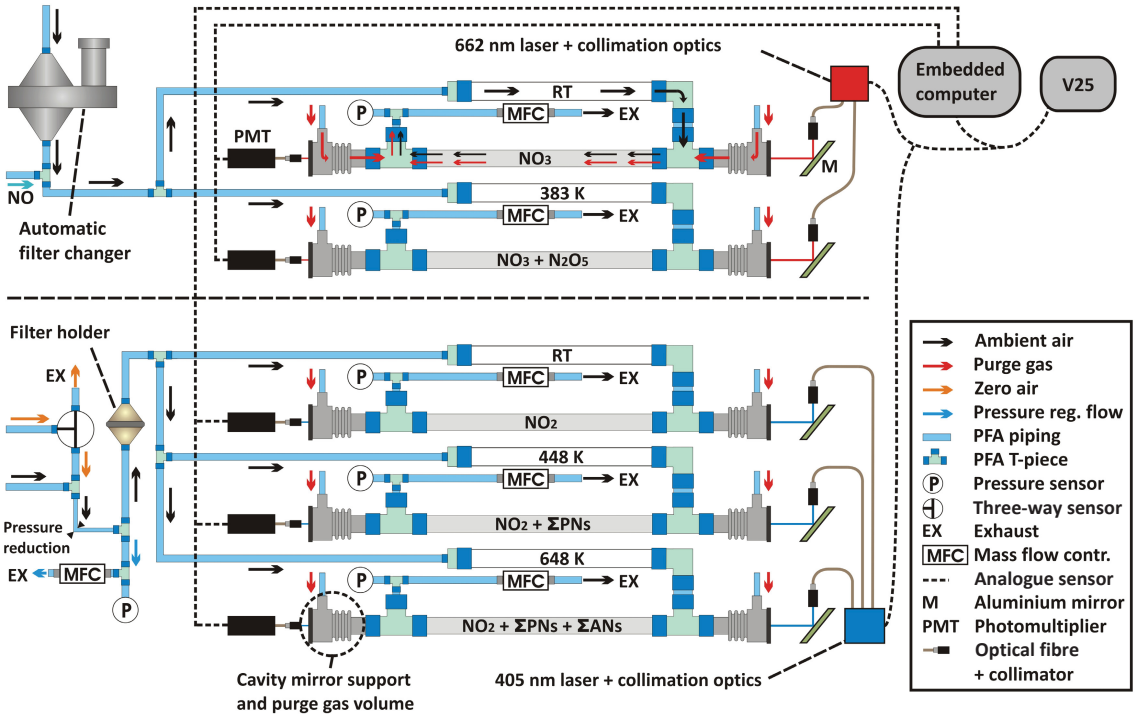

Figure 2. Schematic of the five-channel TD-CRDS. Gas flows are represented by coloured arrows. The wall temperatures of the different inlets are given for each channel. RT: room temperature.

absorbing/scattering gas (i) can be calculated using Eq. (1):

$$[i] = \frac{1}{c\sigma_{(i,\lambda)}}\left(\frac{1}{\tau(s)} - \frac{1}{\tau_0}\right), \quad (1)$$

where τ_0 and τ (s) correspond to decay constants in the absence and presence of absorbing/scattering trace gases, respectively (see Sect. 2.1 and 2.2). $\sigma_{(i,\lambda)}$ is the absorption cross section/scattering coefficient of species i at wavelength λ. The determination of the decay constants is done using a linear regression of sums fitting method (LRS), which has a number of advantages compared to least-squares (LS) fitting (Everest and Atkinson, 2008), including a faster algorithm and the removal of the need to measure an accurate zero (or baseline), which enables use of shorter on–off modulation cycles and higher data acquisition frequencies. Comprehensive comparison between the LS and LRS methods for both synthetic and real ring-down decays showed excellent agreement.

The central part of the instrument described here consists of five cavities of similar design and materials (see Fig. 2). Two cavities are used to detect NO_3 and N_2O_5 (at 662 nm), and three are used to detect NO_2, ΣPNs and ΣANs (at 405 nm). We refer to the five different inlet/cavity combinations (downstream of the filters, see Fig. 2) as the NO_2, NO_3, N_2O_5, ΣPNs and ΣANs channels. The light sources for the five cavities are two laser diodes housed in Thorlabs TCLDM9 modules located in aluminium housing with optical components for beam splitting, collimation and optical isolation (see Sect. 2.1 and 2.2). Coupling between the laser diodes and the cavities is achieved using 50 µm core optical fibres with collimators adjusted to weakly focus the beam (diameter of ≈3 mm) at a point ≈1 m behind the cavity output mirrors. The cavities are constructed from 70 cm long, seamless stainless-steel pipes (1 mm thick, with an inner diameter of 8 mm), which are Teflon-coated (DuPont, FEP, TE 9568). The use of stainless steel as cavity material is considered superior to glass, as used in our previous set-ups (Schuster et al., 2009; Thieser et al., 2016) as it eliminates the risk of breakage, and provides more homogeneous heating of the cavities. Radical losses on FEP-coated stainless-steel or glass surfaces are indistinguishable. PFA T-pieces (Swagelok) are mounted at both ends of the piping for admitting and exhausting the sample flow. Metal bellows/adjustable mirror supports are positioned behind each T-piece, resulting in a distance between mirrors of 93 cm. The bellows provide a purge gas volume for keeping the mirrors clean and reducing physical stress on the mirror supports. The 10 cavity mirrors are continuously purged with dry, synthetic air to prevent degradation in reflectivity. Purging the mirrors has the drawback of reducing the effective cavity length, and thus sensitivity, but it enabled uninterrupted operation over periods of several months. The 10 different purge gas streams are controlled by two mass flow controllers coupled with two sets of crit-

ical orifices designed for different purge flow rates depending on the size and direction of flow of ambient air through the cavities. The purge gas flows for the 405 nm cavities are 500 cm^3 (STP) min^{-1} (sccm) for the mirror opposing the main gas flow (downstream) and 100 sccm for the upstream mirror. For the 662 nm cavities, these flows are 350 (downstream) and 150 sccm (upstream). The light intensity exiting each cavity is measured and converted to an analogue electric signal by a photomultiplier/preamplifier device (Hamamatsu H10492-012 at 662 nm and H10492-002 at 405 nm). Temperature, pressure and flows are measured/regulated by a custom-designed control unit (referred to as V25). Data acquisition (ring downs and laser spectra) and data processing are performed by an embedded computer (NI PXIe-8135). Analogue-to-digital conversion of the photomultiplier signals is performed via two acquisition cards (NI PXI-6132, 14 bit, 3 MS s^{-1}) in the embedded computer rack, one for the two 662 nm cavities and one for the three 405 nm cavities.

2.1 Detection of NO_3 and N_2O_5 at 662 nm

NO_3 and N_2O_5 are detected using the strong absorption feature of NO_3 at about 662 nm ($\sigma_{662\,nm} \approx 2.3 \times 10^{-17}$ cm^2 $molecule^{-1}$ at 298 K; Orphal et al., 2003; Osthoff et al., 2007). NO_3 is measured in one channel (the NO_3 channel) at room temperature. In a second channel (the N_2O_5 channel), the sum of ambient NO_3 and NO_3 arising from the thermal decomposition of N_2O_5 at 383 K are measured, enabling the N_2O_5 mixing ratio to be calculated from the difference. The cavity mirrors (Advanced Thin Films, 1 in. diameter, 1 m radius of curvature) have a nominal reflectivity of 0.999985 and result in ring-down times (at atmospheric pressure of dry synthetic air) of 150–160 µs. To keep a constant emission wavelength of ≈ 662 nm, the laser diode (Thorlabs HL6545MG) is thermostatted to 38 °C and has an emission bandwidth of ≈ 0.5 nm (full width half maximum). An optical isolator is positioned at the immediate output of the diode laser to prevent back reflexions, and the final intensity of light reaching the front mirror of each of the two red cavities is ≈ 10–15 mW. The laser wavelength is monitored using a mini spectrograph (Ocean Optics, type HR4C2509), which records diffuse back reflexions from the N_2O_5 cavity input mirror. Taking into account the emission spectrum and the absorption cross section of NO_3, the effective cross section obtained during the first field deployment and calibrations is $\approx 2.1 \times 10^{-17}$ cm^2 $molecule^{-1}$. The uncertainty on the effective cross section is discussed in Sect. 3.1.

Before entering the NO_3 and N_2O_5 channels, air (≈ 15 L (STP) min^{-1}, slm) is drawn through a filter (Pall Corp., Teflon membrane, 47 mm ∅, 0.2 µm pore) housed in an automatic filter changer. The changer has a maximum capacity of 20–25 filters, allowing for 2–3 nights of measurement (at a change rate of one filter per hour) without requiring the presence of an operator. Losses of NO_3 in the filter and filter changer are discussed in Sect. 3.1. Air exits the filter changer through a 1/4 PFA pipe (≈ 30 cm) with a T-piece to enable the injection of a few standard cubic centimetres per minute of NO (100 ppmv in N_2) for titrating NO_3 and zeroing the instrument, which was performed for a few seconds every 4 min. The air then passes through another T-piece that divides the flow between the NO_3 (8 slm) and N_2O_5 (7 slm) channels. For N_2O_5 detection, the air flows through a heated Teflon-coated glass section (wall temperature 383 K) to decompose N_2O_5 into $NO_3 + NO_2$. This temperature is sufficient to decompose all the N_2O_5, which was verified experimentally by increasing the temperature until the maximum signal was obtained. The residence time in this reactor (≈ 0.2 s) is sufficient to allow for a reaction between total NO_3 and NO to go to completion during zeroing periods. In the NO_3 channel, the air flows first though FEP-coated glass tubing at room temperature to ensure sufficient time for complete NO_3 titration when adding NO (i.e. when zeroing). Residence times are 0.45 s in the NO_3 channel and 0.38 s in the N_2O_5 channel. The pressure in the NO_3 and the N_2O_5 channels is not regulated, and it depends on atmospheric pressure and flow rates in the instrument.

A square-wave signal provided by the V25 is used to modulate the diode laser on and off, and also triggers the acquisition of the individual decays. Typically, the modulation frequency is 400 Hz, with on and off times of 1 and 1.5 ms. Averaging 400 decay constants thus resulted in an instrumental time resolution of one data point per second. An Allan deviation plot obtained under laboratory conditions (800 mbar cavity pressure) for the NO_3 and N_2O_5 cavities is shown in Fig. 3. The Allan deviation plot shows that the (1σ) standard deviations of the zero signal (obtained in this experiment by sampling zero air) for the NO_3 and N_2O_5 channels for a 1 s integration time are 0.1 and 2 pptv, respectively. This is found to be a significant improvement in signal-to-noise ratio compared to the instrument described by Schuster et al. (2009), for which 5 s integration times were necessary to reduce noise levels to ≈ 2 pptv for both NO_3 and N_2O_5 channels. The improvement is likely related to the more stable optical set-up. Despite the fact that the two 662 nm channels in the new instrument are mechanically and optically very similar, the N_2O_5 channel shows a higher noise level, which is related to enhanced turbulence due to temperature and thus density gradients.

2.2 Detection of NO_2, ΣPNs and ΣANs at 405 nm

Three channels sampling in parallel are used for the detection of NO_2 and organic nitrates. The three cavities are maintained at slightly above ambient temperature (305 K) to reduce density fluctuations. All three channels detect NO_2 (ambient, or produced by organic nitrate decomposition) using the absorption of NO_2 at 405 nm (σ_{405nm} at 298 K $\approx 6 \times 10^{-19}$ cm^2 $molecule^{-1}$; Voigt et al., 2002). The cavity mirrors (Advanced Thin Films) have a reflectivity $R \approx$ 0.99995, which results in an average ring down of 30–35 µs

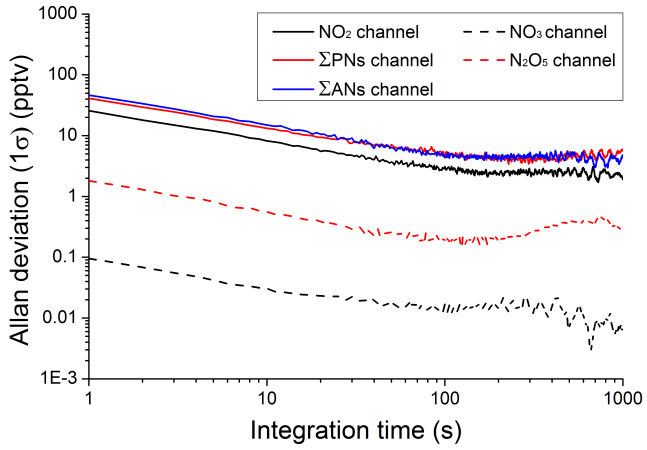

Figure 3. Allan deviation plot (1σ) for each of the five CRDS channels. The data were obtained in the laboratory at ≈ 298 K and a cavity pressure of 800 mbar.

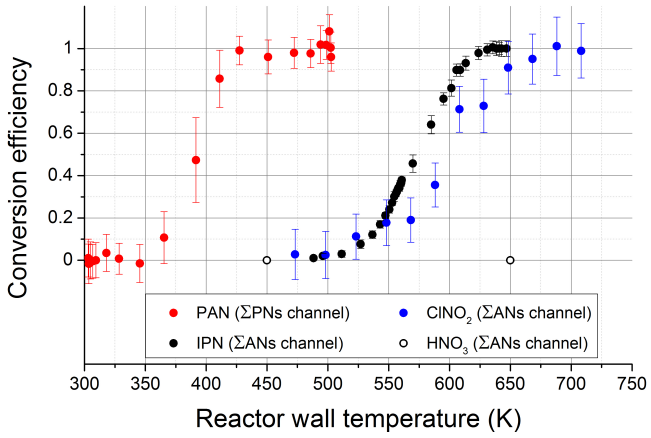

Figure 4. Decomposition profiles of PAN (red points), i-propyl nitrate (black points) and $ClNO_2$ (blue points) with statistical errors (1σ). The PAN decomposition profile was measured in the ΣPNs channel; the i-propyl nitrate (IPN) and $ClNO_2$ profile were measured in the ΣANs channel. The open black circles indicate the lack of HNO_3 decomposition when sampled into the ΣANs channel.

at 700 mbar of dry synthetic air. The 405 nm cavities have a data acquisition system and optical set-up that is similar to the 662 nm cavities, although an optical isolator to prevent back reflections was found by empirical observation to be unnecessary at 405 nm. To keep the peak emission wavelength at 405 nm, the laser diode is held at 35 °C. The maximum intensity coupled into each of the three 405 nm cavities is in the range 10–15 mW. The laser wavelength is monitored using a mini spectrograph (Ocean Optics, type HR4C5451), which records diffuse back reflexions from the ΣANs cavity input mirror. The effective cross section for the three 405 nm channels during the calibrations and field deployment was 5.9×10^{-19} cm^2 molecule^{-1} (based on the laser emission spectrum and the NO_2 absorption cross section).

Ambient NO_2 is detected directly when sampling from a room temperature inlet, whereas PNs and ANs are thermally decomposed in two heated sections of glass tubing at ≈ 448 and ≈ 648 K and then detected as NO_2. In the 448 K channel (ΣPNs channel), the sum of ambient NO_2 plus NO_2 from the thermal decomposition of PNs is measured. In the 648 K channel (ΣANs channel), NO_2 from the decomposition of ANs is additionally detected. The temperature set in the ΣPNs channel (448 K) was chosen by measuring the temperature dependence of the thermal dissociation of PAN (≈ 2 ppbv) in synthetic air as provided by a diffusion source of PAN in tridecane. The normalised [NO_2] signal as a function of temperature (Fig. 4) shows that complete decomposition to NO_2 is achieved at a nominal temperature of ≈ 433 K. The temperatures given in the text and in Fig. 4 correspond to the external surface of the heated inlets and not necessarily that of the gas flowing through them. PANs have a thermal stability that is largely independent of the *R* group (Roberts, 1990b; Kirchner et al., 1999). For the detection of atmospheric PNs, we set the temperature to 15 K above the threshold measured in the laboratory for PAN, i.e. 448 K.

Figure 4 also shows the temperature-dependent decomposition of a sample of isopropyl nitrate in synthetic air: a yield of 100 % is reached at a set temperature of ≈ 633 K. As for PANs, the thermal decomposition of all ANs is expected to be similar, so a working temperature of 648 K was chosen.

Rayleigh scattering of 405 nm light by air (Fuchs et al., 2009; Thieser et al., 2016) results in sensitivity of the ring-down constant to pressure changes, and requires that the three 405 nm cavities are actively pressure-regulated. For this reason, and because zeroing requires overfilling the inlet line (see below), the 405 nm channels have an independent inlet system. In total, ≈ 8 slm air is sampled through 1/4 in. PFA piping, of which 0.5 slm is directed to a digital humidity sensor. Active pressure control of the cavities is achieved by pumping a regulated fraction of the main flow (usually ≈ 0.5 slm) through a flow controller directly to the exhaust system (see Fig. 2) to maintain the desired pressure (generally about 700 mbar). About 7 slm of ambient air is drawn through a filter held by a PFA filter holder. The particle filters used to protect the 405 nm cavities are the same as for the 662 nm cavities, but are changed at a much lower frequency (once per day per hand) due the lower reactivity of NO_2 and organic nitrates to surfaces. After passing through the particle filter, air is then split into three equal flows (≈ 2.3 slm), resulting in residence times of 1.7, 1.3 and 1.1 s for the NO_2, ΣPNs and ΣANs channels, respectively. The three 405 nm channels consist of vertically mounted glass tubing (length ≈ 55 cm, ID = 12 mm) connected to the cavities by PFA fittings as described in Sect. 2. For the ΣPNs and ΣANs channels, a portion of the glass tubing is wrapped with heating wire and heavily insulated to achieve the desired thermal dissociation temperatures of 448 and 648 K. The first 10 cm of the heated section of the glass tubing in the ΣPNs and

ΣANs channels is filled with glass beads (≈ 0.5 mm diameter, Sigma-Aldrich G9268) supported on a glass frit (ca. 2 cm long). More detail and a diagram is given in the Supplement. The surfaces of the glass beads and glass frit scavenge organic radicals formed in the thermal decomposition of PNs and ANs, and thus reduce the impact of radical recombination with NO_2 and oxidation of NO, which can bias the results obtained, especially under conditions of high NO_x (Day et al., 2002; Paul and Osthoff, 2010; Thieser et al., 2016). Details of the laboratory experiments carried out and the corrections necessary to take such processes into account are described in Sect. 3.2.

The three 405 nm channels are zeroed for 30 s every 4 min by overflowing the inlet with ≈ 0.2 slm of bottled synthetic air or with scrubbed air provided by a zero-air generator (CAP 180, Fuhr GmbH). An upper limit to the NO_2 content of the zero air of ≈ 20 pptv was obtained by use of a blue-light converter, as described previously (Thieser et al., 2016). Previous work has shown that the different scattering coefficients for humid, ambient air and the dry, synthetic air used to zero the instrument can lead to a bias in the measured [NO_2]. The difference in the Rayleigh scattering cross section at wavelengths close to 405 nm between synthetic air and water ($\Delta\sigma$) is reported to be between 0.4 and 0.5×10^{-21} cm^2 molecule^{-1} (Fuchs et al., 2009; Thieser et al., 2016). At 50–60 % humidity at 30 °C and 1 bar, this results in an offset of ≈ 200 pptv in the [NO_2] signal. Thieser et al. (2016) have indicated that the 20 % difference in the reported scattering cross sections renders this a significant source of uncertainty at high relative humidity and low NO_2. To avoid introducing additional error by correcting for this, we implemented a zero-air humidification system, which enables the 7 slm air flow used for zeroing the instrument to be actively matched (to better than 2 % up to 80 % relative humidity; RH) to ambient RH (of ambient and zero-air, both measured at 0.2 Hz). This was achieved by passing a variable fraction of the zero air to a bubbler containing distilled water. Taking $\Delta\sigma = 0.5 \times 10^{-21}$ cm^2 molecule^{-1}, the error arising for a 2 % humidity difference at room temperature and 1 bar (measuring conditions of both humidity sensors) is equal to 10 pptv.

As the ring-down times are shorter at 405 nm (typically 35 µs), the diode laser modulation frequency could be increased so that 1666 ring-down constants were obtained per second. Figure 3 shows an Allan deviation plot (1σ) for the NO_2, ΣPNs and ΣANs channels. The 1σ standard deviations for a 1 s integration time for the three 405 nm channels are 25, 40 and 45 pptv, respectively. The higher noise level associated with the ΣPNs and ΣANs channels results from slightly lower mirror reflectivity (different batch) compared to the NO_2 cavity.

3 Data corrections, precision and total uncertainty

When based on known absorption cross sections, CRDS is an absolute concentration measurement technique. However, a number of corrections are necessary to convert measured ring-down times into volume mixing ratios of absorbing trace gases. Some corrections are related to the physical construction of the cavities, and others are related to chemical processes in the inlets and cavities that can bias the concentrations measured. The size and accuracy of these corrections contribute significantly to the overall uncertainty of the measurements, and are discussed in detail below. The more straightforward corrections needed are related to the effective absorption path length (l-to-d ratio), losses of NO_3 radicals in inlets and filters as previously described (Schuster et al., 2009; Thieser et al., 2016) and formation of NO_2 during the sampling time through $O_3 + NO$ reaction. For this instrument, the effective l-to-d ratio is 0.69 ± 0.02 for the channels detecting at 405 nm, and 0.77 ± 0.04 for the channels detecting at 662 nm. Based on several laboratory experiments, the transmission of NO_3 in the filter/filter holder is 70 ± 3 %. The 3 % uncertainty was obtained by repeated measurements under laboratory conditions. During the NOTOMO campaign (see Sect. 4), no discontinuities in the NO_3 signal were observed after hourly filter changes, which implies that there was no measurable change in transmission over the hour of exposure. In highly polluted environments, or those with highly reactive aerosol, this may not be the case, and more frequent filter changes may be necessary to avoid loss of NO_3. No losses of N_2O_5 on passage through the filter holder are observed under laboratory conditions, and similarly to NO_3, no evidence was obtained for losses on aged filters during the NOTOMO campaign. The transmission of NO_3 in the NO_3 and N_2O_5 channels is 97.4 ± 2.5 % and 90.2 ± 5 %, respectively. Details and results of the experiments to derive l-to-d ratios and correction factors for NO_3 losses are given in the Supplement. Corrections related to NO oxidation by O_3 are described in Sect. 3.2.5.

3.1 NO_3 and N_2O_5 channels

For averaging periods of longer than ≈ 1 s, the detection limit of both [NO_3] and [N_2O_5] is defined mainly by variation/drift in the zero signal. Drifts can arise from changes in the mirror reflectivity and through thermal and mechanical stresses that influence the cavity alignment. The detection limit can be estimated by the 2σ standard deviation of the difference from one zeroing period to the next one for the whole campaign. The values for the NO_3 and N_2O_5 channels are respectively 1.5 and 3 pptv, and imply that 95 % of the time, the difference between one zero value to the next one is lower than 1.5 and 3 pptv respectively. The NO_3 limit of detection is thus 1.5 pptv for 1 s averaging and zeroing every 3 min. As N_2O_5 is obtained by difference, the detection limit is ≈ 3.5 pptv (also for 1 s averaging). The total uncertainty

for the [NO_3] measurement can be estimated by propagation of the individual uncertainties associated with the correction factors (see above) and the uncertainty associated with the effective absorption cross section, which depends on the NO_3 absorption cross section uncertainty (≈ 10 %, taken from Osthoff et al., 2007) and the uncertainty associated with measurement of the laser emission spectrum (≈ 5 %). The resulting total uncertainty for NO_3 measurement is 25 %. The uncertainty associated with the [N_2O_5] measurement depends on the absolute values of [NO_3] and [N_2O_5], and is therefore variable. As an example, combining the 25 % uncertainty of the total NO_3 measured in the N_2O_5 channel with [NO_3] and [N_2O_5] mixing ratios of 50 and 500 pptv results in an uncertainty of 28 % for the N_2O_5 measurement.

3.2 NO_2, ΣPNs and ΣANs channels

3.2.1 Losses of NO_2 in the heated ΣPNs and ΣANs inlets

The transmission of NO_2 through the hot glass inlets (with frit and packed with glass beads) of the ΣPNs and ΣANs channels was investigated by sampling NO_2 in synthetic air (up to 10 ppbv)into the three 405 nm channels simultaneously. NO_2 is depleted slightly in the hot inlets with a transmission of 98.5±2 % and 95.5±2 % found for the ΣPNs and ΣANs inlets, respectively (see Fig. 5). The NO_2 transmission was measured before, during and after the field deployment of this instrument (corresponding to a period of several months), and was found to be constant and also independent of relative humidity.

3.2.2 Reaction of radicals with NO / NO_2 in the ΣPNs channel (448 K)

The thermal decomposition of PNs leads to the formation of organic radicals and NO_2. In an ideal situation, in which PNs decompose 100 % to NO_2 and when NO_2 does not undergo any further production or loss reaction, the total [NO_2] measured in the ΣPNs channel is equal to the sum of ambient NO_2 and PNs. Under the operating conditions of the CRDS instrument described here, the total [NO_2] signal in the ΣPNs channel can, however, be biased by a number of reactions initiated by the organic radicals. The influence of these reactions has been described in the literature (Day et al., 2002; Paul and Osthoff, 2010; Thieser et al., 2016). Taking the example of peroxyacetyl nitrate (PAN), subsequent to its thermal decomposition (Reaction R1a), there are processes that lead both to the removal of NO_2 (Reactions R1b, R5) and to its formation (Reactions R2, R3, R4).

$$CH_3C(O)O_2NO_2 + M \rightarrow CH_3C(O)O_2 + NO_2 + M \quad \text{(R1a)}$$
$$CH_3C(O)O_2 + NO_2 + M \rightarrow CH_3C(O)O_2NO_2 + M \quad \text{(R1b)}$$

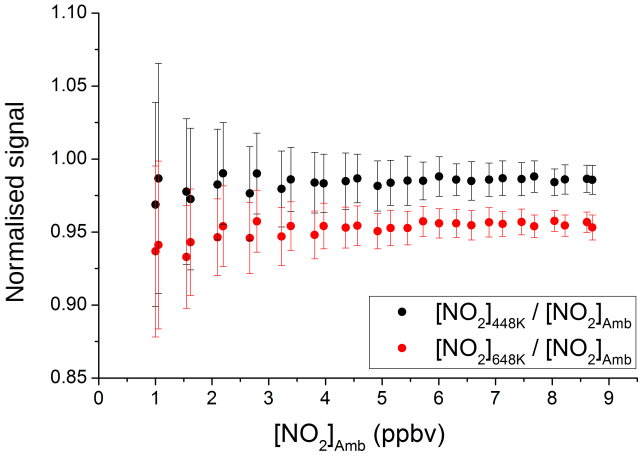

Figure 5. NO_2 loss in the heated inlets of the ΣPNs and ΣANs channels. Black points represent the NO_2 mixing ratio measured in the ΣPNs channel ($[NO_2]_{448\,K}$) normalised to the NO_2 mixing ratio measured in the NO_2 channel ($[NO_2]_{Amb}$). Red points represent the NO_2 mixing ratio measured in the ΣANs channel ($[NO_2]_{648\,K}$) normalised to the NO_2 signal measured in the NO_2 channel.

$$CH_3C(O)O_2 + NO(+O_2) \rightarrow NO_2 + CH_3O_2 + CO_2 \quad \text{(R2)}$$
$$CH_3O_2 + NO(+O_2) \rightarrow HCHO + HO_2 + NO_2 \quad \text{(R3)}$$
$$HO_2 + NO \rightarrow OH + NO_2 \quad \text{(R4)}$$
$$OH + NO_2 + M \rightarrow HNO_3 + M \quad \text{(R5)}$$

Reactions (R2)–(R4) show that, in the most unfavourable scenario, if all organic radicals react with NO, each peroxyacetyl radical can lead to the formation of three NO_2 molecules, biasing the result by the same factor. Likewise, the presence of very high NO_2 could conceivably result in complete reformation of PAN (Reaction R1b). The size and sign of the bias thus depends on the relative concentrations of NO and NO_2 and, most importantly, on the rate of loss of organic radicals to the reactor walls or via thermal decomposition. The bias resulting from these reactions can be reduced by minimising the residence time between thermal dissociation and detection and by making pressure-dependent recombination reactions inefficient by working at low pressures, e.g. by using LIF detection of NO_2 (Day et al., 2002; Wooldridge et al., 2010). As CRDS instruments operate at higher pressures, to maintain sufficient sensitivity (typically from 0.5 to 1 bar), we have taken a different approach and optimised the surface losses of the organic radicals by modifying the surface-to-volume ratio in the heated inlets.

First experiments on PAN samples using glass wool as a radical scavenger resulted in the desired reduction in the rate of recombination of $CH_3C(O)O_2$ with NO_2. Glass wool was, however, observed to greatly enhance (rather than reduce) the oxidation of NO to NO_2. This is presumably the result of a surface-catalysed process as previously observed on powdered, aluminium silicate mineral dust samples (Hanisch and

Crowley, 2003), and may be related to the formation of oxidised surface sites that can react with NO. This led us to test glass beads, which presumably have less reactive "defective" sites than glass wool but a sufficient surface area to remove a large fraction of the organic radicals (see below). We conducted a series of experiments with different mixtures of PAN and NO_2 / NO (from 1 ppmv in synthetic air gas bottles) and analysis of the observations by numerical simulation, similar to that presented in Thieser et al. (2016).

The set of chemical reactions used in the numerical simulations is essentially the same as that described in Thieser et al. (2016). One exception is formation of NO_2 via the reaction between O_3 and NO, which Thieser et al. (2016) treated as occurring independently of other chemical processes. Here, this reaction is treated more rigorously by including it in the chemical simulation. The other difference is the use of two different values for a rate constant (k_s) used to calculate the kinetic limitation on the radical uptake coefficient (γ, see below). In order to simulate all laboratory data sets, different values of k_s (one for sections A and B and one for sections C and D; see Fig. S1 in Supplement) are required to account for the temperature gradient in the heated sections of the inlets. The heterogeneous loss of radicals to the reactor walls is based on a Langmuir–Hinshelwood mechanism, with the first-order rate constant (k_w) given by Eq. (2).

$$k_w = \frac{\gamma \bar{c} A}{4} \quad (2)$$

The uptake coefficient, γ, depends on both kinetic and diffusive limitations as described in detail by Thieser et al. (2016). Here we focus on the role of glass beads in enhancing the rate of uptake and reaction of organic radicals by increasing the surface area available for reaction (A). Without the glass beads, the value of A in the heated inlets is 3.5 $cm^2\,cm^{-3}$ (corresponding to a cylinder with internal diameter 1.2 cm). The presence of the glass beads, with an average diameter of 0.5 mm, results in a surface-to-volume ratio of $\approx 100\,cm^2\,cm^{-3}$. The exact determination of the temperature profile in the inlet is possible in the case of a classic cylindrical reactor, but is difficult to achieve with the presence of the glass beads and glass frit. An approximate profile in section D of the reactor (part of the cylindrical reactor between the fritted glass and the cavity inlet; see Fig. S1) was obtained by measuring the temperature between the fritted glass and the entrance of the cavity. It is assumed that the temperature in section B (containing the glass beads) increases from ambient to 448 K at the point where the gas enters section C (corresponding to the fritted glass section). This profile is also used to calculate the residence time in the ΣPNs channel of 1.3 s. To take into account the variations of temperature, pressure, specific surface area and diffusion radius along the glass reactor, a profile for each of these parameters is used as input in the numerical simulation.

Figure 6a shows results of a set of four experiments in which different amounts of PAN are mixed with different amounts of NO_2 and monitored in the three channels. The y axis shows the total [NO_2] measured in the ΣPNs channel ($[NO_2]_{448\,K}$) minus NO_2 measured in NO_2 channel ($[NO_2]_{Amb}$). The negative slopes of these data indicate that NO_2 from PAN decomposition is lost at high mixing ratios of added NO_2. A similar set of data, but with added NO rather than NO_2, is displayed in Fig. 6b. In this case, the positive slopes indicate that NO_2 is being formed from the reaction of organic radicals with NO. Note that the solid lines are the results of the numerical simulations (with identical mechanism) of NO_2 formation and loss in both experiments. The mixing ratios of PAN listed are those required in the model to match the experimental data. In both data sets the slopes are weakest at low PAN concentrations, reflecting the fact that radical-NO or radical-NO_2 reaction rates will be dependent on the radical concentrations. The mixing ratios of PAN cannot be derived by simple back extrapolation to zero NO_2 or NO as this does not take into account the NO_2 formed when PAN itself decomposes. At the highest mixing ratios of NO_2, up to 25 % of the peroxyacetyl radical recombines with NO_2 while the other 75 % is lost to the walls or did not react with NO_2.

The analysis of the measurements shows that (without correction) NO_2 would be overestimated by approximately 40 % for 3 ppb of PAN when sampling air containing 8 ppbv of NO. This is much lower that the ≈ 150 % reported by Thieser et al. (2016) for similar conditions in their ΣPNs channel, reflecting the increased loss of radicals on the glass surfaces.

In both series of experiments, the model reproduces the data for the whole range of [PAN], [NO_2] and [NO] explored. A set of experiments was carried out to investigate whether the formation (or loss) of NO_2 described above could be influenced by the presence of water vapour acting, for example, as a quencher of a surface reaction. A mixture of PAN plus NO_2 was humidified to 60 % RH, with other operating conditions similar to the previous experiments. The numerical model reproduced the measurement data without the need to modify the wall loss rates or add any chemical processes involving H_2O, suggesting that the gas and surface reactions taking place are not significantly influenced by adsorbed water at these temperatures. In order to correct field data for these biases, an iterative fitting procedure is used and described in detail in Sect. 4.2.

3.2.3 Reaction of radicals with NO / NO_2 in the ΣANs channel (648 K)

As first discussed by Thieser al. (2016), experimental and theoretical studies show that the higher temperature (648 K) of the ΣANs channel changes the chemical processes substantially compared to 448 K. ANs can now decompose to NO_2 and an alkyl radical fragment, whereas the peroxyacetyl radical (from PAN decomposition) is thermally unstable. The NO_2 generated in the ΣANs channel when adding NO_2 / NO to PAN samples is displayed in Fig. 6c and d. The results

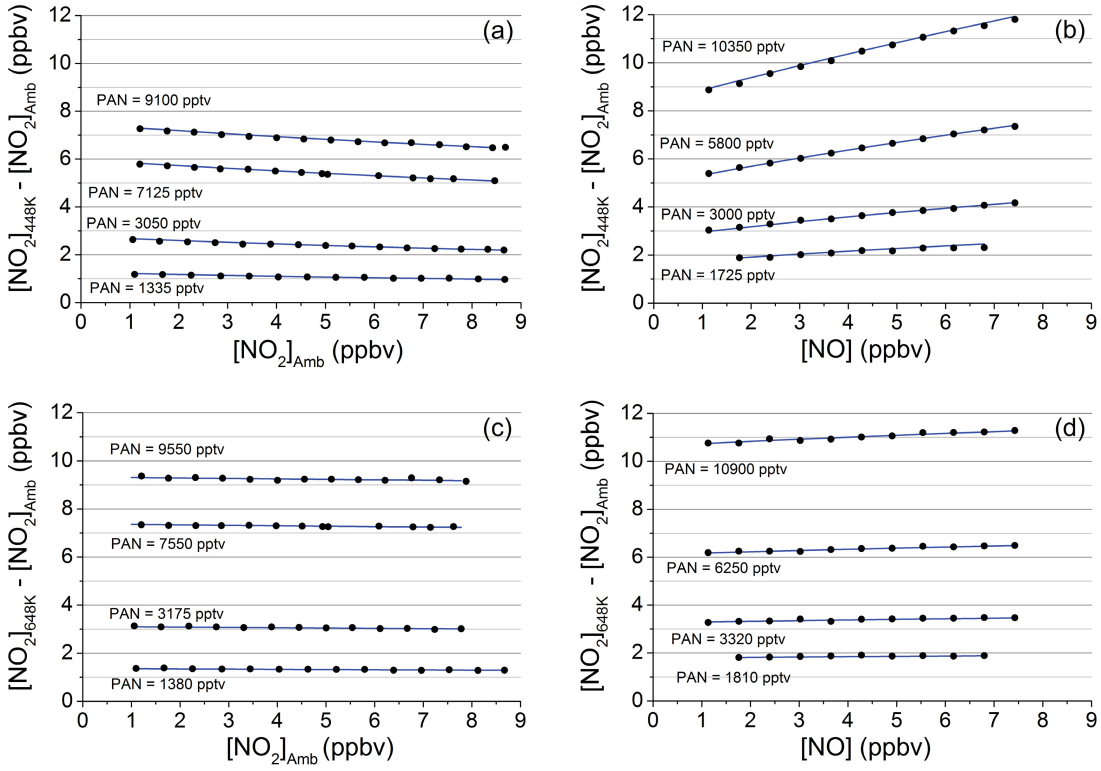

Figure 6. Modelled (lines) and measured difference between the NO_2 signal in the hot channels and ambient temperature channel for different PAN samples and different added amounts of NO and NO_2. **(a)** Addition of NO_2 to the 448 K (PNs) channel. **(b)** Addition of NO to the 448 K (PNs) channel. **(c)** Addition of NO_2 to the 648 K (ANs) channel. **(d)** Addition of NO_2 to the 648 K (ANs) channel.

show a greatly reduced effect of NO_2 recombination or NO oxidation compared to the ΣPNs channel (Fig. 6a, b), largely resulting from the instability of the of $CH_3C(O)O_2$ radical. The model takes into account two main pathways for the fate of the peroxyacetyl radical (Reactions R6, R7) in which the acetyl radical (CH_3CO) formed in Reaction (R6) can react further with O_2 to reform a peroxyacetyl radical or an OH radical and an α-lactone (Reactions R8, R9) (Carr et al., 2011). $CH_2C(O)OOH$ can also decompose to OH and an α-lactone (Reaction R10) (Carr et al., 2007, 2011; Chen and Lee, 2010). If not lost to the walls, OH can react with NO_2 to form HNO_3 according to Reaction (R5).

$$CH_3C(O)O_2 + M \rightarrow CH_3CO + O_2 + M \quad \text{(R6)}$$
$$CH_3C(O)O_2 \rightarrow CH_2C(O)OOH \quad \text{(R7)}$$
$$CH_3CO + O_2 + M \rightarrow CH_3C(O)O_2 + M \quad \text{(R8)}$$
$$CH_3CO + O_2 \rightarrow OH + C_2H_2O_2 \quad \text{(R9)}$$
$$CH_2C(O)OOH \rightarrow OH + C_2H_2O_2 \quad \text{(R10)}$$
$$CH_3CO + O_2 + M \rightarrow CH_3O_2 + CO + M \quad \text{(R11)}$$

The acetyl radical can also form a methylperoxy radical CH_3O_2 through the formation of a CH_3 radical and CO. The net reaction is given by Reaction (R11). In the presence of NO, the peroxy radicals ($CH_3C(O)O_2$, CH_3O_2 and HO_2), if not lost to the glass surface, can lead to the formation of NO_2. To simulate the reactions in the ΣANs channel, the temperature profile was determined in the same way as the ΣPNs channel profile. Due to the higher gas flow velocity at the elevated temperatures, the pressure profile is slightly different than in the ΣPNs channel and gives a cavity pressure that is about 10 mbar lower. The results of the experiments involving addition of NO_2 to PAN samples in the ANs channel are presented in Fig. 6c. For the range of PAN concentrations covered, the loss of NO_2 by chemical recombination is about 5 % of the initial PAN. The initial PAN concentration used as input variable for the numerical simulations is, for all four experiments, about 3–5 % higher than that needed to fit the data obtained in the PNs channel (Fig. 6a), which is most probably related to model uncertainties. Since this 3–5 % difference is the same for all four experiments and is apparently not correlated with the amount of PAN, it is added to the calculation of total uncertainty for the PNs measurement. The results of the NO addition experiments are shown in Fig. 6d. The thermal decomposition of the peroxyacetyl radical reduces the positive bias due to NO oxidation so that a maximum factor of only 1.04 (compared to 1.40 in the ΣPNs channel) is obtained. The initial PAN concentration required to fit the NO addition data set at 648 K is 5–10 % higher than at 448 K,

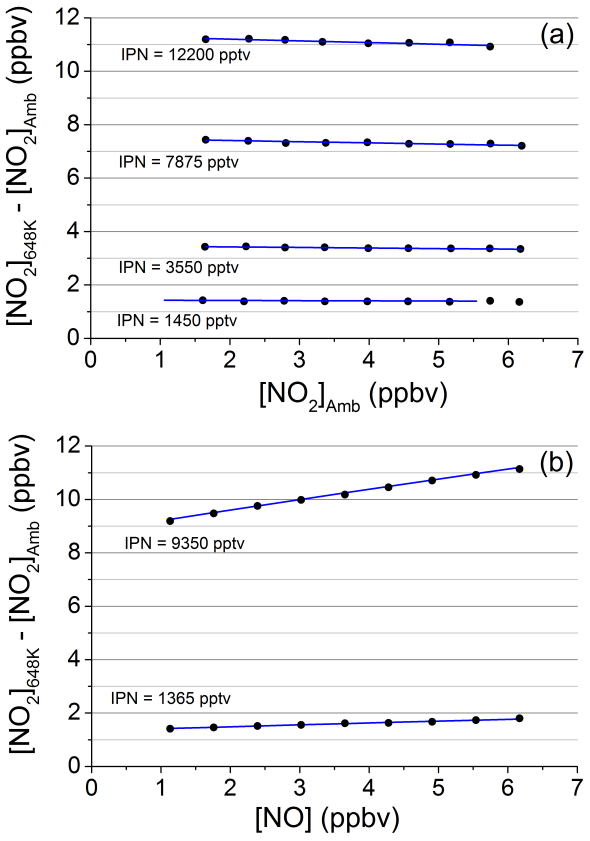

Figure 7. Modelled (lines) and measured difference between the NO_2 signal in the 648 K channels and ambient temperature channel for i-propyl nitrate (IPN) samples and different added amounts of NO_2 **(a)** or NO **(b)**.

which is related to uncertainty in the [NO] mixing ratio used or a bias in the simulation.

In order to investigate the role of organic (alkyl) radicals generated from the thermal decomposition of ANs, a set of experiments was conducted in which a sample of i-propyl nitrate ($C_3H_7ONO_2$) in synthetic air was mixed with different amounts of NO and NO_2. Thermal decomposition of i-propyl nitrate (Reaction R12) is followed by Reactions (R13) and (R14) that generate HO_2 and CH_3O_2, which can convert NO to NO_2 and sequester NO_2 as HO_2NO_2 and $CH_3O_2NO_2$.

$$C_3H_7ONO_2 \rightarrow C_3H_7O + NO_2 \quad \text{(R12)}$$
$$C_3H_7O + O_2 \rightarrow CH_3C(O)CH_3 + HO_2 \quad \text{(R13)}$$
$$C_3H_7O + M \rightarrow CH_3 + CH_3CHO + M \quad \text{(R14)}$$

Figure 7a and b show that the addition of NO increases the amount of NO_2 formed per AN, whereas the presence of NO_2 results in a negative bias to the data. These effects are captured well for both data sets by the model simulations (blue lines).

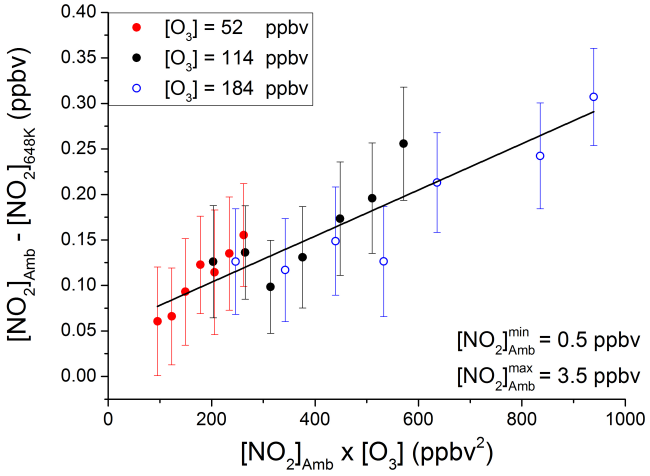

Figure 8. Influence of O_3 pyrolysis. Loss of NO_2 (in ppbv) in the heated ΣANs channel compared to the NO_2 channel vs. the product of the NO_2 and O_3 mixing ratios.

3.2.4 Effect of thermal decomposition of O_3

At high temperatures, O_3 decomposes according to Reaction (R15). Although most of the O atom produced reacts with O_2 to reform ozone (Reaction R16), it can form NO+O_2 in the presence of NO_2 (Reaction R17).

$$O_3 \rightarrow O_2 + O \quad \text{(R15)}$$
$$O + O_2 + M \rightarrow O_3 + M \quad \text{(R16)}$$
$$O + NO_2 \rightarrow O_2 + NO \quad \text{(R17)}$$

The importance of this process is strongly dependent on the operating conditions of the instrument, recent studies showing that higher temperatures or pressures may result in a significant, negative bias from the ozone-pyrolysis-initiated reduction of NO_2 (Lee et al., 2014; Thieser et al., 2016). Assuming that the steady-state concentration of the O atom in the heated inlets is dominated by Reactions (R15) and (R16) ($k_{16}[O_2] \gg k_{17}[NO_2]$), the loss of NO_2 can be approximated as follows:

$$-d[NO_2] = [NO_2][O_3]\left(\frac{k_{15}k_{17}}{k_{16}[O_2]}t\right). \quad (3)$$

The term in brackets is constant at constant temperature, pressure and flow rate through the heated inlet, and can be determined experimentally by sampling different mixtures of NO_2 and O_3 simultaneously through the ambient temperature channel and the two hot channels. Figure 8 shows the difference $[NO_2]_{Amb} - [NO_2]_{648\,K}$ (in ppbv) as a function of $[NO_2] \times [O_3]$ for three different levels of ozone (50, 115 and 185 ppbv). A linear fit through the data points yields a slope of $2.54 \pm 0.26 \times 10^{-4}$ ppbv^{-1}, which is $< 50\,\%$ of the value found by Thieser et al. (2016). The difference can be attributed mainly to the use of a lower oven temperature

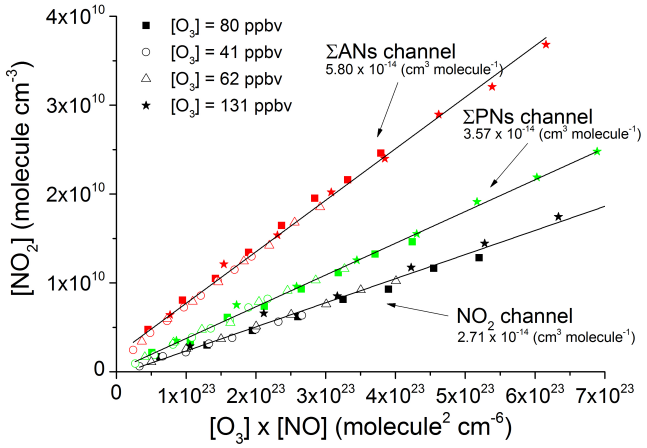

Figure 9. Production of NO_2 from the $O_3 + NO$ reaction when sampling into the three 405 nm channels with different amounts of NO and O_3. The numbers in parentheses are the slopes of least-squares fits (solid lines), which correspond to the product of the effective second-order rate constant and the reaction time.

(648 K in this work instead of 723 K). No reduction of NO_2 is observed in the ΣPNs channel because thermal decomposition of O_3 at 448 K is too slow. To illustrate the impact of the thermal dissociation of O_3 in the ANs channel, we note that 5 ppbv of total NO_2 in the presence of 50 ppbv of O_3 results in the removal of 75 pptv NO_2. Since the amount of O_3 decomposed and NO produced in this process is negligible compared to ambient amounts, it does not affect the input conditions for the numerical simulations, and can therefore be treated separately using Eq. (3).

3.2.5 Effect of NO oxidation by O_3

A positive bias to the measurement of NO_2 may result from NO oxidation by O_3 during the time it takes for the sampled air to flow through the inlets and cavities of the instrument (Reaction R18).

$$NO + O_3 \rightarrow NO_2 \qquad \text{(R18)}$$

The rate coefficient of this reaction is temperature-dependent, and the effect is larger at 448 and 648 K than at room temperature. To investigate this interference, different mixtures of O_3 and NO were sampled simultaneously through the three channels. The results are shown in Fig. 9 where data from four experiments with different O_3 mixing ratios (41, 62, 80 and 131 ppbv) are plotted. The solid lines are fits to the data, the slopes of which are second-order rate constants multiplied by a reaction time (cm^3 $molecule^{-1}$). The rate constant for the gas-phase reaction between NO and O_3 is listed as $k_{O_3+NO} = 9 \times 10^{-19} \exp(-850/T) \times T^{2.25}$ cm^3 $molecule^{-1}$ s^{-1} (Atkinson et al., 2004). For the ΣPNs channel (448 K), using this expression results in an underestimation of the effective (measured) production of NO_2 by a factor 1.06. For the ΣANs (648 K) channel the equivalent factor is 1.52. The most likely reason for this discrepancy is that some NO is oxidised in a surface catalysed process, presumably involving surface sites that are activated following interaction with O_3. To account for this extra source of NO_2, the O_3 plus NO reaction is implemented in the chemical model (with modified rate expressions) for the 448 and 648 K data corrections (see Sect. 3.2.2 and 3.2.3), and corrected manually for the NO_2 channel.

3.2.6 Detection of other species as NO_2 after thermal dissociation

Atmospheric trace gases other than PNs and ANs can potentially be detected as NO_2 in this instrument. As thermal decomposition of N_2O_5 to NO_3 and NO_2 has been shown to be 100 % efficient in our 383 K inlet in the 662 nm channels, we expect 100 % dissociation at the higher temperatures of the ΣPNs and ΣANs channels. This may represent a significant source of bias during the night when N_2O_5 mixing ratios can be large. However, as the five-channel instrument simultaneously monitors N_2O_5, this can be easily corrected. Here we consider possible HNO_3 and $ClNO_2$ interferences in the ΣANs channel.

HNO_3 is a major reservoir of tropospheric NO_x. Although HNO_3 is thermally stable at temperatures below 700 K, Wild et al. (2014) report ≈ 95 % conversion of HNO_3 to NO_2 at 648 K, whereas Thieser et al. (2016) found about 10 % at 723 K. In order to test for unwanted detection of HNO_3 when sampling from the hot inlets (with glass beads) in the five-channel instrument, we injected a sample of HNO_3 in synthetic air directly prior to the flow division before entering the three 405 nm channels. In this way, possible losses of HNO_3 in the inlet in front of the heated sections of the instrument were minimised. HNO_3 was generated in a custom-built permeation source, which was calibrated by absorption spectroscopy at 184.85 nm, where HNO_3 absorbs strongly. The permeation source generated several parts per million by volume of HNO_3 in a flow of 10 sccm, which, following dilution, provided a mixing ratio of ≈ 30 ppbv at the CRDS inlet. The permeation source also generated about 3 ppbv of NO_2. Figure 4 (open circles) shows that NO_2 arising from HNO_3 decomposition could not be observed in either heated inlet, enabling us to set an upper limit to the decomposition efficiency of HNO_3 to NO_2 of < 0.5 %. This is in broad agreement with the previous measurement by Thieser et al. (2016), who saw no evidence for HNO_3 decomposition below 650 K, and is in stark contrast to that reported by Wild et al. (2014). While we have no rigorous explanation of this, we note that the gas-phase thermal dissociation of HNO_3 to NO_2 at the temperature of these experiments is too slow to explain its formation, which suggests that it is probably surface-catalysed in the experiments of Wild et al. (2014), implying that different glass types or chemical history of the surface may influence the formation of NO_2 significantly.

As reported previously, $ClNO_2$, formed in the atmosphere in the reaction between N_2O_5 and chloride-containing particles, can be detected as NO_2 in TD-CRDS instruments (Thaler et al., 2011; Wild et al., 2014; Thieser et al., 2016) The $ClNO_2$ decomposition efficiency as a function of the oven temperature is plotted in Fig. 4. The $ClNO_2$ sample was generated by flowing Cl_2 in synthetic air over sodium nitrite crystals. In normal operating conditions (at 648 K), 90 ± 3 % of the $ClNO_2$ is decomposed to NO_2. As $ClNO_2$ mixing ratios are highly variable and can approach parts per billion by volume levels, $ClNO_2$ may thus represent a serious limitation to ANs measurements, unless independent measurements are available to enable correction.

3.2.7 Detection limit and total uncertainty for NO_2, PNs and ANs

The detection limit for the 405 nm channels can be estimated in a similar manner to that described for the 662 nm channels. The 2σ standard deviation for consecutive zeros for the NO_2, ΣPNs and ΣANs channels are respectively 59, 74 and 54 pptv. Using these values, we obtain detection limits for $[NO_2]$, [PNs] and [ANs] of 59, 94 and 80 pptv. The detection limits for [PNs] and [ANs] are obtained by error propagation on the NO_2 and PNs channels and NO_2 and ANs channel (see Sect. 4).

The total uncertainty associated with the $[NO_2]$ measurement is a combination of the uncertainties in the l-to-d ratio, humidity matching of the zero and ambient air and the correction for the $NO + O_3$ reaction on the absorption cross section of NO_2 and on N_2O_5 decomposition. The total uncertainty on the absorption cross section is estimated to 6 %, taking into account the error on the reference cross section (Voigt et al., 2002) and fluctuation in the laser emission spectrum. This value, when combined with the uncertainty associated with the l-to-d ratio, results in 6.5 % uncertainty. The uncertainty associated with the correction for NO_2 formation in the $NO + O_3$ reaction depends on ambient ozone and NO levels. Considering 10 % uncertainty for k_{O_3+NO} and 5 % uncertainty for $[O_3]$, [NO] and $[NO_2]$, [NO] and $[O_3]$ ambient levels of 1, 0.5 and 50 ppbv, we obtain an uncertainty for this correction of 0.1 % on the final $[NO_2]$ value. NO_2 can be formed at room temperature by the slow thermal decomposition of N_2O_5. Taking a decomposition rate constant of 4.4×10^{-2} s^{-1} at 303 K for N_2O_5 (Atkinson et al., 2016) and a residence time in the NO_2 channel of 1.7 s, we calculate that 0.08 of the N_2O_5 can decompose. The largest N_2O_5-to-NO ratio measured during NOTOMO was 0.17, which results in a maximum contribution of ≈ 1.5 % NO_2 from N_2O_5 decomposition. As mentioned in Sect. 2.2, the upper limit for bias caused by humidity matching errors when zeroing is 10 pptv, which results in a final uncertainty for $[NO_2]$ of $8\,\% + 10$ pptv.

The uncertainty of the total NO_2 detected in the ΣPNs and ΣANs channels is a combination of the same uncertainties involved in the $[NO_2]$ measurement plus the uncertainty of the NO_2 transmission through the heated glass beads. Taking the values listed in Sect. 3.2.1, we obtain an uncertainty for total NO_2 detected of 7 % pptv for both ΣPNs and ΣANs channels. To correct for the radical plus NO_x biases, the total NO_2 signals measured in the two hot channels are used to constrain the chemical model described earlier. The uncertainty arising from these calculations depends on the total $[NO_2]$ measured in each channel, and is thus highly variable. Note that uncertainty arising from the humidity difference is cancelled out by the subtraction to obtain [PNs] and [ANs]. The uncertainty added by the calculation of the ambient [PNs] and [ANs] depends on the model uncertainties, as well as on the uncertainty associated with the trace gas concentrations involved in this calculation. The uncertainty associated with [ΣPNs] and [ΣANs] is related to ambient $[NO_2]$, $[O_3]$ and [NO]. The fact that the corrections rely on PAN and IPN chemistry led Thieser et al. (2016) to estimate the uncertainty associated with the model-derived corrections to be 30 % (max) of the overall correction factor. The final uncertainties on the [ΣPNs] and [ΣANs] value depend on the total NO_2 signal in all three channels, and can vary significantly. Below, we discuss the correction factors required for the NO_2, ΣPNs and ΣANs data sets obtained during the first field deployment of the instrument.

4 First field deployment of the five-channel CRDS

The instrument described here was first deployed during the NOTOMO campaign (Nocturnal Observations at the Taunus Observatory; insights into Mechanisms of Oxidation) that took place during summer 2015. The site, previously described in detail (Crowley et al., 2010; Sobanski et al., 2016), is situated on top of the Kleiner Feldberg mountain (≈ 850 m a.s.l.) at the southern limit of the forested Taunus mountain range and north of the Frankfurt–Mainz–Wiesbaden agglomeration. The set of instruments deployed during NOTOMO was located in two research containers, and sampled from a common inlet. Approximately ≈ 10 m^3 min^{-1} air was drawn from a height of 8 m above ground through a 15 cm diameter stainless-steel pipe connected to an industrial fan. Gases were sampled (≈ 23 slm) in the TD-CRDS (located in the upper container) from the centre of the high-flow inlet via 1/2 in. PFA tubing (for the two 662 nm channels) and 1/3 in. PFA tubing (for the three 405 nm channels) ≈ 3.5 m from the top of the inlet. Residence times in the high flow inlet, in the 1/2 in. PFA tubing and in the 1/4 in. PFA tubing were 0.3, 0.05 and 0.1 s, respectively. In the following sections we shall not attempt to perform a detailed analysis of the entire campaign data set, which is beyond the scope of this paper, but provide a more qualitative description of the results, and indicate the size of corrections applied and the total uncertainty.

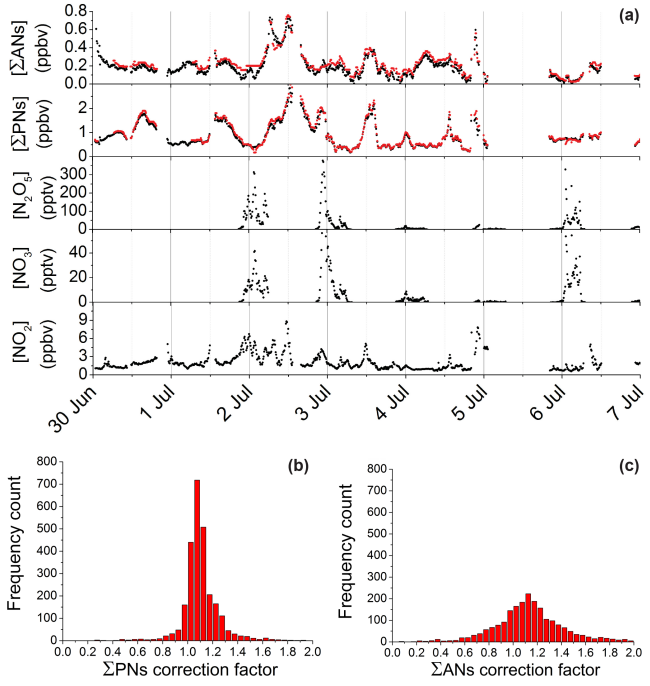

Figure 10. **(a)** Mixing ratios of NO_2, NO_3, N_2O_5, ΣPNs and ΣANs measured by the TD-CRDS instrument between 30 June and 7 July 2015 at the Kleiner Feldberg observatory, Germany, as part of the NOTOMO campaign. For the three lowest panels in ([NO_2], [NO_3] and [N_2O_5], the black points represent the final corrected data. For the ΣPNs panel, the black points correspond to uncorrected data obtained by subtracting [NO_2] measured in the NO_2 channel from the NO_2 measured in the ΣPNs channel. The red points have been corrected using the chemical model with the iterative fitting procedure. For the ΣANs panel, the black points correspond to the uncorrected data (obtained by subtracting the NO_2 signal measured in the ΣPNs channel from the NO_2 signal measured in the ΣANs channel). The red points have been corrected using the chemical model plus iterative fitting procedure. Panels **(b)** and **(c)** are frequency distributions for the correction factors applied using the iterative numerical simulations.

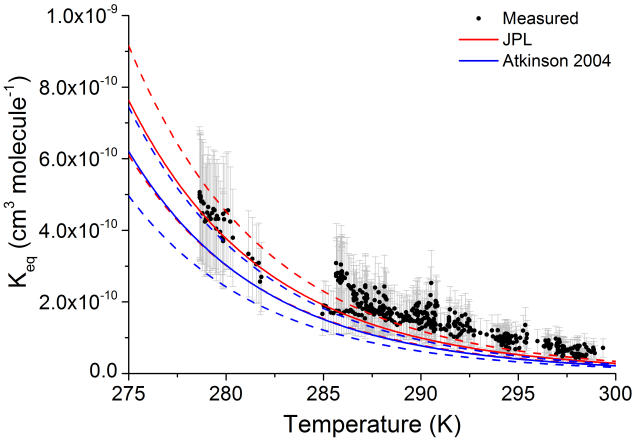

Figure 11. Equilibrium constant (K_{eq}) for the reaction $NO_2 + NO_3 = N_2O_5$ calculated from measurement of each trace gas (black points, with grey bars representing total uncertainty). The solid lines are values of K_{eq} recommended by the JPL evaluation panel (red line; Burkholder et al., 2016) and IUPAC evaluation committee (blue line; Atkinson et al., 2004). The dashed lines represent the minimum and maximum values according to the evaluations.

4.1 Mixing ratios of NO_2, NO_3, N_2O_5

Figure 10a shows the measured mixing ratios of NO_2, NO_3, N_2O_5, ΣPNs and ΣANs for 1 week between 30 June and 7 July. During this period, [NO_2] varied from 0.3 to 6 ppbv, with an average value of 1.8 ppbv. NO_3 and N_2O_5 mixing ratios reach up to 40 and 400 pptv at night, and are below the detection limit during the day. These values are in the range of previous measurements at this location (Crowley et al., 2010; Sobanski et al., 2016), in which NO_2, NO_3 and N_2O_5 mixing ratios of up to 20, ≈200 and ≈3000 pptv, respectively were measured. Within a few minutes after sunset, NO_2, NO_3 and N_2O_5 acquire thermal equilibrium and the equilibrium constant, K_{eq}, can be calculated from [N_2O_5] / [NO_2][NO_3]. In Fig. 11 we compare temperature-dependent values of the equilibrium constant using measured concentrations of NO_2, NO_3 and N_2O_5 as well as values from the literature that are based on laboratory measurements (Atkinson et al., 2004; Burkholder et al., 2016). Within combined uncertainty, the values agree, though we note that the parameterisation of Burkholder et al. (2016) results in values that are closer to those obtained by analysing the field measurements and that the agreement is better at lower temperatures. We are wary of over-interpretation of this fact and are aware that the laboratory determinations that led to the recommended values are expected to be more accurate, especially close to room temperature where many data sets exist and are in good agreement. In this context we note that small errors in the measurement of the ambient temperature or a 10–20 % inlet loss of NO_3 would have been difficult to observe but would have had a significant impact on the equilibrium constant calculated from the field data and may have contributed to the differences observed.

4.2 Mixing ratios of ΣPNs and ΣANs

By simply subtracting [NO_2] measured by the NO_2 channel from the total NO_2 signal measured by the PAN channel and the total NO_2 signal in the ΣPNs channel from the total NO_2 signal in ΣANs channel, we obtain uncorrected mixing ratios for ΣPNs and ΣANs, which are plotted (black data points) in Fig. 10. In this context, uncorrected means that no chemical corrections have been applied (e.g. for reformation of PNs in the presence of NO_2, or formation of NO_2 from NO oxidation with O_3 see Sect. 3) but physical corrections (e.g. *l*-to-*d* ratio) have been made.

The procedure used to correct the [ΣPNs] and [ΣANs] mixing ratios for the effects described in Sect. 3 utilises an iterative algorithm based on the chemical model used to simulate the laboratory data described in Sect. 3.2. To correct the ΣPNs data, a simulation using [NO_2], [O_3] and [NO] values and an initial guess for [ΣPNs] were performed. Values of O_3 were taken from ambient measurements, whereas, in the absence of NO measurements, we assumed that its mixing ratio was zero at night-time and during the day could be calculated from its photochemical steady state, $[NO]_{ss} = J_{NO_2}[NO_2]/k_{NO+O_3}[O_3]$, where J_{NO_2} is the photolysis frequency of NO_2 (measured using a spectral radiometer) and k_{NO+O_3} is the rate constant for reaction of NO with O_3. This method of estimating [NO] resulted in satisfactory agreement with measurements from the Hessian Agency for Nature Conservation, Environment and Geology (HLUG) for periods when NO was above the detection limit (> 1 ppb) of their instrument, which monitors NO permanently at the site.

In the iterative procedure, [ΣPNs] were tuned automatically until the simulated total [NO_2] matched the measured [NO_2] in the ΣPNs channel. This procedure was applied to each data point (10 min resolution) obtained during the campaign. The corrected [ΣPNs] were used as an additional input to correct the [ΣANs] data. In this case, constant values for [NO_2], [O_3], [NO_2] and [ΣPNs] and a variable value for [ΣANs] are inputted into the model to match the total NO_2 signal measured in the ΣANs channel. For the correction of the [ΣPNs] data, ambient N_2O_5 was taken into account by adding its mixing ratio to the initial [NO_2] values. This was also done also for the [ΣANs] correction. Measured $ClNO_2$ mixing ratio was decreased by a factor of 0.9 to account for the decomposition efficiency and was then added to the initial [NO_2] for simulation of the total NO_2 in the ΣANs channel. The corrected data are displayed as red data points in Fig. 10a.

The overall correction factor (corrected data/uncorrected data) required for the ΣPNs and ΣANs measurements are illustrated in Fig. 10b and c. The peak of the distributions is at ≈ 1.1 for both data sets, and the sigma values corresponding to a Gaussian fit are 0.06 and 0.18 for ΣPNs and ΣANs respectively, indicating that the corrections required are dominated by NO_2 rather than NO, and that the corrections for the ΣANs vary more due to the presence of more organic radicals in the ΣANs channel.

5 Conclusions

We have constructed and characterised a five-channel, thermal-dissociation cavity ring-down spectrometer for measurement of the reactive nitrogen traces gases, NO_2, NO_3, N_2O_5 peroxy nitrates and alkyl nitrates, which provides insight into the coupling of atmospheric, daytime and night-time NO_x and RO_x chemistry. The total measurement uncertainties and limits of detection are estimated at 25 % and 2 pptv for NO_3, 28 % and 10 pptv for N_2O_5 and 6.5 % +10 and 59 pptv for NO_2.

Chemical interferences in the measurements of PNs and ANs were reduced by the use of low TD temperatures and the use of glass beads as the radical scavenger. In combination with extensive laboratory tests to enable accurate correction for bias in PNs and ANs measurements resulting from reactions of organic radicals formed in the thermal-dissociation channels, this reduces overall uncertainty and extends the NO_x regime in which the instrument can be operated. The total uncertainty associated with the PNs and ANs measurements is dependent on NO_x levels and also on the presence (mainly at night) of $ClNO_2$ and N_2O_5. During the PARADE campaign the average correction was (1.1 ± 0.3) where the quoted uncertainty is an estimate of systematic error related to the use of a numerical model to simulate chemical processes in the TD sections of the instrument.

6 Data availability

The PARADE data can be obtained on request (via John Crowley) from the owners. The NOTOMO data will be released at the end of 2017.

The Supplement related to this article is available online at doi:10.5194/amt-9-1-2016-supplement.

Acknowledgements. We are grateful to the following: Bernard Brickwedde for technical/software assistance. We thank DuPont for provision of a sample of the FEP used to coat the cavity walls. We thank Heinz Bingemer for logistical support and use of the facilities at the Taunus Observatory during the NOTOMO campaign. This work was carried out in part fulfilment of the PhD of Nicolas Sobanski at the Johannes Gutenberg University in Mainz, Germany.

The article processing charges for this open-access publication were covered by the Max Planck Society.

Edited by: D. Toohey
Reviewed by: two anonymous referees

References

Allan, B. J., Carslaw, N., Coe, H., Burgess, R. A., and Plane, J. M. C.: Observations of the nitrate radical in the marine boundary layer, J. Atmos. Chem., 33, 129–154, 1999.

Arey, J., Aschmann, S. M., Kwok, E. S. C., and Atkinson, R.: Alkyl Nitrate, Hydroxyalkyl Nitrate, and Hydroxycarbonyl Formation from the NO_x Air Photooxidations of C_5-C_8 n-Alkanes, J. Phys. Chem. A, 105, 1020–1027, 2001.

Atkinson, R., Baulch, D. L., Cox, R. A., Crowley, J. N., Hampson, R. F., Hynes, R. G., Jenkin, M. E., Rossi, M. J., and Troe, J.: Evaluated kinetic and photochemical data for atmospheric chemistry: Volume I – gas phase reactions of O_x, HO_x, NO_x and SO_x species, Atmos. Chem. Phys., 4, 1461–1738, doi:10.5194/acp-4-1461-2004, 2004.

Beaver, M. R., Clair, J. M. St., Paulot, F., Spencer, K. M., Crounse, J. D., LaFranchi, B. W., Min, K. E., Pusede, S. E., Wooldridge, P. J., Schade, G. W., Park, C., Cohen, R. C., and Wennberg, P. O.: Importance of biogenic precursors to the budget of organic nitrates: observations of multifunctional organic nitrates by CIMS and TD-LIF during BEARPEX 2009, Atmos. Chem. Phys., 12, 5773–5785, doi:10.5194/acp-12-5773-2012, 2012.

Berden, G., Peeters, R., and Meijer, G.: Cavity ring-down spectroscopy: Experimental schemes and applications, Int. Rev. Phys. Chem., 19, 565–607, 2000.

Blanchard, P., Shepson, P. B., Schiff, H. I., and Drummond, J. W.: Development of a gas chromatograph for trace gas-chromatograph for trace-level measurement of peroxyacetyl nitrate using chemical amplification, Anal. Chem., 65, 2472–2477, doi:10.1021/ac00066a012, 1993.

Brown, S. S.: Absorption spectroscopy in high-finesse cavities for atmospheric studies, Chem. Rev., 103, 5219–5238, 2003.

Burkholder, J. B., Sander, S. P., Abbatt, J., Barker, J. R., Huie, R. E., Kolb, C. E., Kurylo, M. J., Orkin, V. L., Wilmouth, D. M., and Wine, P. H.: Chemical Kinetics and Photochemical Data for Use in Atmospheric Studies, Jet Propulsion Laboratory, Pasadena, Evaluation No. 18, JPL Publication 15-10, available at: http://jpldataeval.jpl.nasa.gov., 2016.

Carr, S. A., Baeza-Romero, M. T., Blitz, M. A., Pilling, M. J., Heard, D. E., and Seakins, P. W.: OH yields from the $CH_3CO + O_2$ reaction using an internal standard, Chem. Phys. Lett., 445, 108–112, 2007.

Carr, S. A., Glowacki, D. R., Liang, C.-H., Baeza-Romero, M. T., Blitz, M. A., Pilling, M. J., and Seakins, P. W.: Experimental and modeling studies of the pressure and temperature dependences of the kinetics and the OH yields in the acetyl $+ O_2$ reaction, J. Phys. Chem. A, 115, 1069–1085, 2011.

Chen, S.-Y. and Lee, Y.-P.: Transient infrared absorption of t-$CH_3C(O)OO$, c-$CH_3C(O)OO$, and α-lactone recorded in gaseous reactions of CH_3CO and O_2, J. Chem. Phys., 132, 114303, doi:10.1063/1.3352315, 2010.

Crowley, J. N., Schuster, G., Pouvesle, N., Parchatka, U., Fischer, H., Bonn, B., Bingemer, H., and Lelieveld, J.: Nocturnal nitrogen oxides at a rural mountain-site in south-western Germany, Atmos. Chem. Phys., 10, 2795–2812, doi:10.5194/acp-10-2795-2010, 2010.

Day, D. A., Wooldridge, P. J., Dillon, M. B., Thornton, J. A., and Cohen, R. C.: A thermal dissociation laser-induced fluorescence instrument for in situ detection of NO_2, peroxy nitrates, alkyl nitrates, and HNO_3, J. Geophys. Res., 107, ACH 4-1–ACH 4-14, doi:10.1029/2001jd000779, 2002.

Day, D. A., Dillon, M. B., Wooldridge, P. J., Thornton, J. A., Rosen, R. S., Wood, E. C., and Cohen, R. C.: On alkyl nitrates, O_3, and the "missing NO_y", J. Geophys. Res., 108, 4501, doi:10.1029/2003jd003685, 2003.

Dorn, H.-P., Apodaca, R. L., Ball, S. M., Brauers, T., Brown, S. S., Crowley, J. N., Dubé, W. P., Fuchs, H., Häseler, R., Heitmann, U., Jones, R. L., Kiendler-Scharr, A., Labazan, I., Langridge, J. M., Meinen, J., Mentel, T. F., Platt, U., Pöhler, D., Rohrer, F., Ruth, A. A., Schlosser, E., Schuster, G., Shillings, A. J. L., Simpson, W. R., Thieser, J., Tillmann, R., Varma, R., Venables, D. S., and Wahner, A.: Intercomparison of NO_3 radical detection instruments in the atmosphere simulation chamber SAPHIR, Atmos. Meas. Tech., 6, 1111–1140, doi:10.5194/amt-6-1111-2013, 2013.

Everest, M. A. and Atkinson, D. B.: Discrete sums for the rapid determination of exponential decay constants, Rev. Sci. Instrum., 79, 023108, doi:10.1063/1.2839918, 2008.

Flocke, F., Volz-Thomas, A., and Kley, D.: Measurements of alkyl nitrates in rural and polluted air masses, Atmos. Environ. A-Gen., 25, 1951–1960, 1991.

Fuchs, H., Dube, W. P., Lerner, B. M., Wagner, N. L., Williams, E. J., and Brown, S. S.: A Sensitive and Versatile Detector for Atmospheric NO_2 and NO_x Based on Blue Diode Laser Cavity Ring-Down Spectroscopy, Environ. Sci. Technol., 43, 7831–7836, doi:10.1021/es902067h, 2009.

Fuchs, H., Ball, S. M., Bohn, B., Brauers, T., Cohen, R. C., Dorn, H.-P., Dubé, W. P., Fry, J. L., Häseler, R., Heitmann, U., Jones, R. L., Kleffmann, J., Mentel, T. F., Müsgen, P., Rohrer, F., Rollins, A. W., Ruth, A. A., Kiendler-Scharr, A., Schlosser, E., Shillings, A. J. L., Tillmann, R., Varma, R. M., Venables, D. S., Villena Tapia, G., Wahner, A., Wegener, R., Wooldridge, P. J., and Brown, S. S.: Intercomparison of measurements of NO_2 concentrations in the atmosphere simulation chamber SAPHIR during the NO3Comp campaign, Atmos. Meas. Tech., 3, 21–37, doi:10.5194/amt-3-21-2010, 2010.

Fuchs, H., Simpson, W. R., Apodaca, R. L., Brauers, T., Cohen, R. C., Crowley, J. N., Dorn, H.-P., Dubé, W. P., Fry, J. L., Häseler, R., Kajii, Y., Kiendler-Scharr, A., Labazan, I., Matsumoto, J., Mentel, T. F., Nakashima, Y., Rohrer, F., Rollins, A. W., Schuster, G., Tillmann, R., Wahner, A., Wooldridge, P. J., and Brown, S. S.: Comparison of N_2O_5 mixing ratios during NO3Comp 2007 in SAPHIR, Atmos. Meas. Tech., 5, 2763–2777, doi:10.5194/amt-5-2763-2012, 2012.

Hanisch, F. and Crowley, J. N.: heterogeneous reactivity of NO and HNO_3 on mineral dust in the presence of ozone, Phys. Chem. Chem. Phys., 5, 883–887, 2003.

Johnston, H. S., Davis, H. F., and Lee, Y. T.: NO_3 photolysis product channels: Quantum yields from observed energy thresholds, J. Phys. Chem., 100, 4713–4723, doi:10.1021/jp952692x, 1996.

Kirchner, F., Mayer-Figge, A., Zabel, F., and Becker, K. H.: Thermal stability of peroxynitrates, Int. J. Chem. Kinet., 31, 127–144, 1999.

Lee, L., Wooldridge, P. J., Gilman, J. B., Warneke, C., de Gouw, J., and Cohen, R. C.: Low temperatures enhance organic nitrate formation: evidence from observations in the 2012 Uintah Basin Winter Ozone Study, Atmos. Chem. Phys., 14, 12441–12454, doi:10.5194/acp-14-12441-2014, 2014.

Lehmann, K. K. and Romanini, D.: The superposition principle and cavity ring-down spectroscopy, J. Chem. Phys., 105, 10263–10277, doi:10.1063/1.472955, 1996.

Murphy, J. G., Thornton, J. A., Wooldridge, P. J., Day, D. A., Rosen, R. S., Cantrell, C., Shetter, R. E., Lefer, B., and Cohen, R. C.: Measurements of the sum of HO_2NO_2 and $CH_3O_2NO_2$ in the remote troposphere, Atmos. Chem. Phys., 4, 377–384, doi:10.5194/acp-4-377-2004, 2004.

O'Keefe, A. and Deacon, D. A. G.: Cavity ring-down optical spectrometer for absorption measurements using pulsed laser sources, Rev. Sci. Instrum., 59, 2544–2551, doi:10.1063/1.1139895, 1988.

Orphal, J., Fellows, C. E., and Flaud, P. M.: The visible absorption spectrum of NO_3 measured by high-resolution Fourier transform spectroscopy, J. Geophys. Res., 108, 4077, doi:10.1029/2002JD002489, 2003.

Osthoff, H. D., Pilling, M. J., Ravishankara, A. R., and Brown, S S.: Temperature dependence of the NO_3 absorption cross-section above 298 K and determination of the equilibrium constant for $NO_3 + NO_2 <-> N_2O_5$ at atmospherically relevant conditions, Phys. Chem. Chem. Phys., 9, 5785–5793, 2007.

Paul, D. and Osthoff, H. D.: Absolute Measurements of Total Peroxy Nitrate Mixing Ratios by Thermal Dissociation Blue Diode Laser Cavity Ring-Down Spectroscopy, Anal. Chem., 82, 6695–6703, doi:10.1021/ac101441z, 2010.

Paul, D., Furgeson, A., and Osthoff, H. D.: Measurements of total peroxy and alkyl nitrate abundances in laboratory-generated gas samples by thermal dissociation cavity ring-down spectroscopy, Rev. Sci. Instrum., 80, 114101, doi:10.1063/1.3258204, 2009.

Perring, A. E., Pusede, S. E., and Cohen, R. C.: An observational perspective on the atmospheric impacts of alkyl and multifunctional nitrates on ozone and secondary organic aerosol, Chem. Rev., 113, 5848–5870, doi:10.1021/cr300520x, 2013.

Platt, U., Perner, D., Winer, A. M., Harris, G. W., and Pitts, J. N. J.: Detection of NO_3 in the polluted troposphere by differential optical absorption, Geophys. Res. Lett., 7, 89–92, doi:10.1029/GL007i001p00089, 1980.

Roberts, J. M.: The atmospheric chemistry of organic nitrates, Atmos. Environ. A-Gen., 24, 243–287, doi:10.1016/0960-1686(90)90108-y, 1990a.

Roberts, J. M.: The atmospheric chemistry of organic nitrates, Atmos. Environ. A-Gen., 24, 243–287, 1990b.

Roberts, J. M., Fajer, R. W., and Springston, S. R.: Capillary gas-chromatographic separation of alkyl nitrates and peroxycarboxylic nitric anhydrides, Anal. Chem., 61, 771–772, doi:10.1021/ac00182a026, 1989.

Schuster, G., Labazan, I., and Crowley, J. N.: A cavity ring down/cavity enhanced absorption device for measurement of ambient NO_3 and N_2O_5, Atmos. Meas. Tech., 2, 1–13, doi:10.5194/amt-2-1-2009, 2009.

Slusher, D. L., Huey, L. G., Tanner, D. J., Chen, G., Davis, D. D., Buhr, M., Nowak, J. B., Eisele, F. L., Kosciuch, E., Mauldin, R. L., Lefer, B. L., Shetter, R. E., and Dibb, J. E.: Measurements of pernitric acid at the South Pole during ISCAT 2000, Geophys. Res. Lett., 29, 2011, doi:10.1029/2002gl015703, 2002.

Sobanski, N., Tang, M. J., Thieser, J., Schuster, G., Pöhler, D., Fischer, H., Song, W., Sauvage, C., Williams, J., Fachinger, J., Berkes, F., Hoor, P., Platt, U., Lelieveld, J., and Crowley, J. N.: Chemical and meteorological influences on the lifetime of NO_3 at a semi-rural mountain site during PARADE, Atmos. Chem. Phys., 16, 4867–4883, doi:10.5194/acp-16-4867-2016, 2016.

Thaler, R. D., Mielke, L. H., and Osthoff, H. D.: Quantification of nitryl chloride at part per trillion mixing ratios by thermal dissociation cavity ring-down spectroscopy, Anal. Chem., 83, 2761–2766, doi:10.1021/ac200055z, 2011.

Thieser, J., Schuster, G., Schuladen, J., Phillips, G. J., Reiffs, A., Parchatka, U., Pöhler, D., Lelieveld, J., and Crowley, J. N.: A two-channel thermal dissociation cavity ring-down spectrometer for the detection of ambient NO_2, RO_2NO_2 and $RONO_2$, Atmos. Meas. Tech., 9, 553–576, doi:10.5194/amt-9-553-2016, 2016.

Voigt, S., Orphal, J., and Burrows, J. P.: The temperature and pressure dependence of the absorption cross-sections of NO_2 in the 250-800 nm region measured by Fourier-transform spectroscopy, J. Photoch. Photobio. A, 149, 1–7, doi:10.1016/s1010-6030(01)00650-5, 2002.

Wayne, R. P., Barnes, I., Biggs, P., Burrows, J. P., Canosa-Mas, C. E., Hjorth, J., Le Bras, G., Moortgat, G. K., Perner, D., Poulet, G., Restelli, G., and Sidebottom, H.: The nitrate radical: Physics, chemistry, and the atmosphere, Atmos. Environ. A-Gen., 25, 1–206, 1991.

Wild, R. J., Edwards, P. M., Dube, W. P., Baumann, K., Edgerton, E. S., Quinn, P. K., Roberts, J. M., Rollins, A. W., Veres, P. R., Warneke, C., Williams, E. J., Yuan, B., and Brown, S. S.: A measurement of total reactive nitrogen, NO_y, together with NO_2, NO, and O_3 via cavity ring-down spectroscopy, Environ. Sci. Technol., 48, 9609–9615, doi:10.1021/es501896w, 2014.

Wooldridge, P. J., Perring, A. E., Bertram, T. H., Flocke, F. M., Roberts, J. M., Singh, H. B., Huey, L. G., Thornton, J. A., Wolfe, G. M., Murphy, J. G., Fry, J. L., Rollins, A. W., LaFranchi, B. W., and Cohen, R. C.: Total Peroxy Nitrates (ΣPNs) in the atmosphere: the Thermal Dissociation-Laser Induced Fluorescence (TD-LIF) technique and comparisons to speciated PAN measurements, Atmos. Meas. Tech., 3, 593–607, doi:10.5194/amt-3-593-2010, 2010.

Appendix A2

A 5-channel cavity ring-down spectrometer for the detection of NO_2, NO_3, N_2O_5, total peroxy nitrates and total alkyl nitrates

N. Sobanski[1], J. Schuladen[1], G. Schuster[1], J. Lelieveld[1] and J. N. Crowley[1]

[1]Atmospheric Chemistry Department, Max-Planck-Institut für Chemie, 5 55128 Mainz, Germany.

Supplementary information

A 5-channel cavity ring-down spectrometer for the detection of NO_2, NO_3, N_2O_5, total peroxy nitrates and total alkyl nitrates

N. Sobanski[1], J. Schuladen[1], G. Schuster[1], J. Lelieveld[1] and J. N. Crowley[1]

[1]Atmospheric Chemistry Department, Max-Planck.Institut für Chemie, 55128 Mainz, Germany.

Correspondence to: John N. Crowley (john.crowley@mpic.de)

Supplementary Information

Heated inlets for the ΣPNs and ΣANs channels

The following schematic diagram outlines the construction of the heated inlets. Air at ambient temperature flows through section A before being heated in section B, which is filled with glass beads of ~ 0.5 mm diameter which rest on a on a glass frit support (section C). The temperature profile downstream of the heated volume (section D) was measured by insertion of a thermocouple, whereas those of sections B and C are estimated.

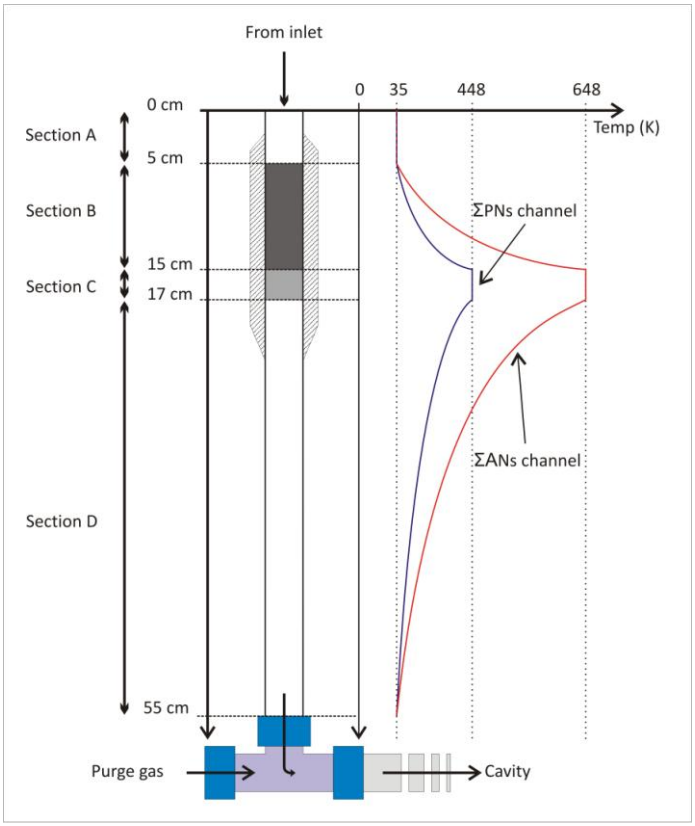

***l-to-d* ratio**

The distance between the cavity mirrors (*d*, optical length) is the same for all five cavities (approximately 93 cm). However, the length over which the sampled air circulates (*l*, absorbing length) is shorter and corresponds roughly to the distance between the inflow and outflow T-pieces (≈ 72 cm). For all five channels, the ambient air flowing through the cavity mixes with the purge gas stream and is thus diluted by a factor that depends on the relative flow rates of air and purge gas. The modification of the absorber length and dilution effects caused by using purge gas to protect the mirrors can be combined into one single correction factor which can be determined experimentally by comparing the NO_2 concentration in two channels, one being operated normally (with purge gas) while the second one is modified so that the NO_2 / air sample completely fills the cavity including the purge gas volume. The value l / d was found to be 0.69 ± 0.02 for the channels

detecting at 405 nm and 0.77 ± 0.04 for the channels detecting at 662 nm. These numbers are entirely in accord with simple calculations based on the construction of the cavities (i.e. distances between mirrors and inlet/outlet T-pieces) and purge gas flow rates suggesting that there is negligible mixing of purge gas and ambient air close to the mirrors.

NO_3 and N_2O_5 losses in the filter changer

The custom-built filter changer used in this instrument consists of a circular plate that transports filters from a supply stack in a cylinder (flushed with dry synthetic air or N_2) to a holder and from the holder to a used-filter-dump. The holder is made of two conical, FEP coated stainless steel parts that are pressed together by springs to hold the filters and forced apart pneumatically during filter changes.

Typically, filters are changed every hour during field deployment of the instrument, which has been sufficient to minimise the loss of NO_3 or N_2O_5 on contaminated filters (Dorn et al., 2013). Measurement of the loss of NO_3 and N_2O_5 on passing through the filter holder equipped with a fresh filter was performed by flowing a sample of NO_3 in synthetic air alternatively through the filter changer or through a short PFA bypass line. NO_3 was generated by mixing NO_2 and photochemically produced O_3. Under typical flow conditions (15 slm passing through the filter holder at ≈ 850 mbar) the loss of NO_3 was 30 ± 3% (statistical error) assuming no losses in the PFA ¼" bypass line. No losses of N_2O_5 on passage through the filter holder were observed.

NO_3 and N_2O_5 losses in the cavities

The cavities as well as the NO_3 titration volume and the N_2O_5 decomposition reactor are all coated with FEP. However, losses of radicals (especially NO_3) to surfaces during passage through the inlets and cavities remain non negligible. Different methods of estimating these losses are found in the literature (Dubé et al., 2006; Fuchs et al., 2008). The method used here consists of varying the individual flows of an NO_3 / synthetic air sample through both channels while keeping the total flow (and thus the NO_3 mixing ratio) constant. In this way, losses in the main inlet of the instrument and in the filter changer remain constant while the residence time in each channel is varied. The results of such an experiment are displayed in Fig. S2, which shows an exponential decrease in $[NO_3]$ in both channels as a function of the residence time. In this case, values of 0.1101 ± 0.0006 s^{-1} (2σ) and 0.28±0.01 s^{-1} were obtained for the NO_3 and the N_2O_5 channels, respectively. The values obtained are enhanced above that for wall loss alone by the reaction of NO_3 with NO_2, which is present in the gas-mixture used to generate NO_3. To account for this, a simulation of NO_3 loss processes using the initial $[NO_2]$ value and rate constants for the reaction of NO_2 with NO_3 (R2) and

the thermal decomposition of N_2O_5 (R3) was performed. The resulting wall loss rate was calculated to be 0.06 s^{-1} for the NO_3 channel. This value is retained to correct [NO_3] field data. The effective value of 0.28 s^{-1} can be used to correct the NO_3 losses in the N_2O_5 channel directly, as the loss of NO_3 via formation of N_2O_5 is offset by the large thermal dissociation rate constant of N_2O_5 at 383 K in comparison with the formation reaction of N_2O_5. The value 0.28 s^{-1} for the N_2O_5 channel was obtained using a reduced range of residence times due to the degradation of the signal when running this channel at flow rates lower than 4 slm. This effect is not documented in the literature and is thought to be specific to our instrument design and is likely due to flow patterns resulting in enhanced turbulence under some conditions. The wall loss rates obtained are of the same order of magnitude as previous values obtained for NO_3 uptake on Teflon coated surfaces or PFA tubing (Schuster et al., 2009). The difference in loss rate between the cold and the hot channel is likely due to enhanced rates of transport of NO_3 to the walls in the more turbulent conditions and to the increases uptake coefficient. Finally, the transmissions for NO_3 in the NO_3 and N_2O_5 channels are 97.4 ± 2.5 % and 90.2 + 5 %, respectively. The error of both values is a conservative estimation based on the variability of wall loss rate constants over time (i.e. prior to and after a campaign), which may reflect variation in the reactivity of the inlet and cavity walls after sampling different air masses.

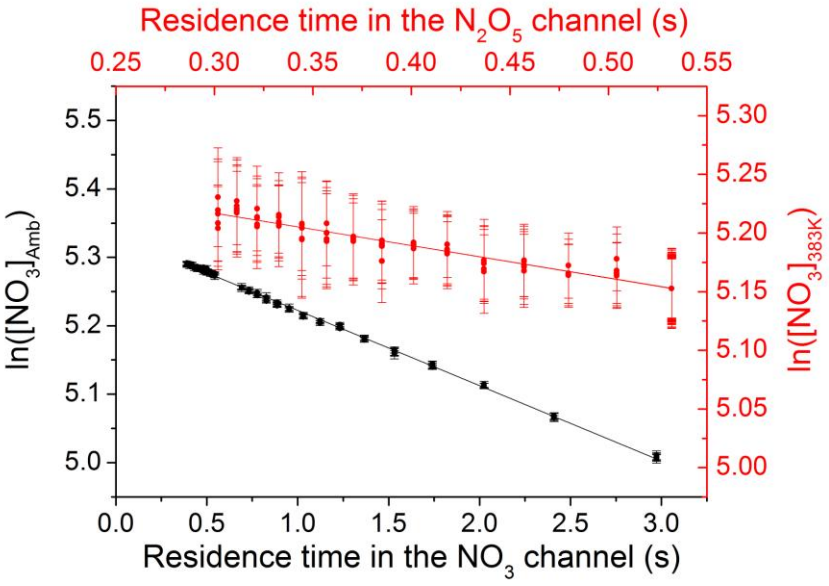

References:

Dorn, H. P., Apodaca, R. L., Ball, S. M., Brauers, T., Brown, S. S., Crowley, J. N., Dubé, W. P., Fuchs, H., Häseler, R., Heitmann, U., Jones, R. L., Kiendler-Scharr, A., Labazan, I., Langridge, J. M., Meinen, J., Mentel, T. F., Platt, U., Pöhler, D., Rohrer, F., Ruth, A. A., Schlosser, E., Schuster, G., Shillings, A. J. L., Simpson, W. R., Thieser, J., Tillmann, R., Varma, R., Venables, D. S., and Wahner, A.: Intercomparison

of NO3 radical detection instruments in the atmosphere simulation chamber SAPHIR, Atmospheric measurement techniques, 6, 1111-1140, doi:10.5194/amt-6-1111-2013, 2013.

Dubé, W. P., Brown, S. S., Osthoff, H. D., Nunley, M. R., Ciciora, S. J., Paris, M. W., McLaughlin, R. J., and Ravishankara, A. R.: Aircraft instrument for simultaneous, in situ measurement of NO3 and N2O5 via pulsed cavity ring-down spectroscopy, Rev. Sci. Instrum., 77, doi: 10.1063/1.2176058, 2006.

Fuchs, H., Dube, W. P., Cicioira, S. J., and Brown, S. S.: Determination of inlet transmission and conversion efficiencies for in situ measurements of the nocturnal nitrogen oxides, NO3, N2O5 and NO2, via pulsed cavity ring-down spectroscopy, Anal. Chem., 80, 6010-6017, 2008.

Schuster, G., Labazan, I., and Crowley, J. N.: A cavity ring down / cavity enhanced absorption device for measurement of ambient NO_3 and N_2O_5, Atmospheric measurement techniques, 2, 1-13, 2009.

Appendix B1

Chemical and meteorological influences on the lifetime of NO_3 at a semi-rural mountain site during PARADE

N. Sobanski[1], M. J. Tang[1,a], J. Thieser[1], G. Schuster[1], D. Pöhler[2], H. Fischer[1], W. Song[1], C. Sauvage[1], J. Williams[1], J. Fachinger[3], F. Berkes[4,b], P. Hoor[4], U. Platt[2], J. Lelieveld[1], and J. N. Crowley[1]

[1]Division of Atmospheric Chemistry, Max-Planck-Institut für Chemie, Mainz, Germany
[2]Institute of Environmental Physics, University of Heidelberg, Heidelberg, Germany
[3]Division of Particle Chemistry, Max-Planck-Institut für Chemie, Mainz, Germany
[4]Institute for Atmospheric Physics, Johannes Gutenberg University Mainz, Mainz, Germany
[a]present address: Chemistry Department, University of Iowa, Iowa City, USA
[b]present address: Institute of Energy and Climate, Forschungszentrum Jülich, Jülich, Germany

Atmos. Chem. Phys., 16, 4867–4883, 2016
www.atmos-chem-phys.net/16/4867/2016/
doi:10.5194/acp-16-4867-2016
© Author(s) 2016. CC Attribution 3.0 License.

Atmospheric Chemistry and Physics Open Access EGU

Chemical and meteorological influences on the lifetime of NO_3 at a semi-rural mountain site during PARADE

N. Sobanski[1], M. J. Tang[1,a], J. Thieser[1], G. Schuster[1], D. Pöhler[2], H. Fischer[1], W. Song[1], C. Sauvage[1], J. Williams[1], J. Fachinger[3], F. Berkes[4,b], P. Hoor[4], U. Platt[2], J. Lelieveld[1], and J. N. Crowley[1]

[1]Division of Atmospheric Chemistry, Max-Planck-Institut für Chemie, Mainz, Germany
[2]Institute of Environmental Physics, University of Heidelberg, Heidelberg, Germany
[3]Division of Particle Chemistry, Max-Planck-Institut für Chemie, Mainz, Germany
[4]Institute for Atmospheric Physics, Johannes Gutenberg University Mainz, Mainz, Germany
[a]present address: Chemistry Department, University of Iowa, Iowa City, USA
[b]present address: Institute of Energy and Climate, Forschungszentrum Jülich, Jülich, Germany

Correspondence to: J. N. Crowley (john.crowley@mpic.de)

Received: 15 January 2016 – Published in Atmos. Chem. Phys. Discuss.: 22 January 2016
Revised: 21 March 2016 – Accepted: 4 April 2016 – Published: 20 April 2016

Abstract. Through measurements of NO_2, O_3 and NO_3 during the PARADE campaign (PArticles and RAdicals, Diel observations of mEchanisms of oxidation) in the German Taunus mountains we derive nighttime steady-state lifetimes (τ_{ss}) of NO_3 and N_2O_5. During some nights, high NO_3 ($\sim$ 200 pptv) and N_2O_5 ($\sim$ 1 ppbv) mixing ratios were associated with values of τ_{ss} that exceeded 1 h for NO_3 and 3 h for N_2O_5 near the ground. Such long boundary-layer lifetimes for NO_3 and N_2O_5 are usually only encountered in very clean/unreactive air masses, whereas the PARADE measurement site is impacted by both biogenic emissions from the surrounding forest and anthropogenic emissions from the nearby urbanised/industrialised centres. Measurement of several trace gases which are reactive towards NO_3 indicates that the inferred lifetimes are significantly longer than those calculated from the summed loss rate. Several potential causes for the apparently extended NO_3 and N_2O_5 lifetimes are examined, including additional routes to formation of NO_3 and the presence of a low-lying residual layer. Overall, the most likely cause of the anomalous lifetimes are related to the meteorological conditions, though additional NO_3 formation due to reactions of Criegee intermediates may contribute.

1 Introduction

NO_3 and N_2O_5 are key species in the chemical removal of NO_x and of several hydrocarbons at night (Wayne et al., 1991; Atkinson and Arey, 2003). Traditionally, NO_3 is considered to be formed mainly by the reaction of NO_2 with O_3 (Reaction R1) with negligible contributions e.g. from reaction between OH and HNO_3 (Reaction R2) or the photolysis of halogen nitrates ($XONO_2$), where X may be Br or Cl (Reaction R3). N_2O_5 is produced in an association reaction between NO_3 and NO_2 (Reaction R4a), with which it is in thermal equilibrium (Reactions R4a, b).

$$NO_2 + O_3 \rightarrow NO_3 + O_2 \quad \text{(R1)}$$
$$OH + HNO_3 \rightarrow NO_3 + H_2O \quad \text{(R2)}$$
$$XONO_2 + h\nu \rightarrow NO_3 + X \quad \text{(R3)}$$

$$NO_2 + NO_3 + M \rightarrow N_2O_5 + M \quad \text{(R4a)}$$
$$N_2O_5 + M \rightarrow NO_3 + NO_2 + M \quad \text{(R4b)}$$

The production rate of NO_3 is therefore usually assumed to be the product of the NO_2 and O_3 concentrations and the rate constant (k_1):

$$P(NO_3) = k_1[NO_2][O_3]. \quad (1)$$

In general, equilibrium between N_2O_5, NO_3 and NO_2 is reached rapidly following sunset and holds until sunrise (Brown et al., 2003). During the day, NO_3 is photolysed (with a lifetime of a few seconds) to give $NO_2 + O$ (Reaction R5a, $\sim 90\,\%$) or $NO + O_2$ (Reaction R5b, $\sim 10\,\%$) (Johnston et al., 1996) and also reacts quickly with NO (Reaction R6) so that NO_3 and N_2O_5 mixing ratios are usually below the detection limit of most instruments. During the night, in the absence of light to regenerate it from NO_2 (Reaction R7) and with sufficient distance from emissions sources, NO levels approach 0 (due to Reaction R8) and NO_3 and N_2O_5 can accumulate in the atmosphere.

$$NO_3 + h\nu \rightarrow NO_2 + O \quad \text{(R5a)}$$

$$NO_3 + h\nu \rightarrow NO + O_2 \quad \text{(R5b)}$$

$$NO_3 + NO \rightarrow 2NO_2 \quad \text{(R6)}$$

$$NO_2 + h\nu \rightarrow NO + O \quad \text{(R7)}$$

$$NO + O_3 \rightarrow NO_2 + O_2 \quad \text{(R8)}$$

The mechanism and rate of removal of NO_3 and N_2O_5 from the atmosphere depend on the type of air mass. In areas impacted by local anthropogenic activity, NO can be a major sink of NO_3. The rate constant for this reaction of $2.6 \times 10^{-11}\,cm^3\,molecule^{-1}\,s^{-1}$ at 298 K (Atkinson et al., 2004) results, for example, in a chemical lifetime for NO_3 of about 16 s in the presence of 100 pptv of NO. NO_3 mixing ratios measured in situ at ground level in cities are sometimes low due to the high mixing ratio of NO. However, a few tens of kilometres downwind of urban areas or several tens of metres aloft, where [NO] can be significantly lower due to reduced mixing of ground-level emissions and titration by O_3, NO_3 mixing ratios can reach up to several hundred pptv and N_2O_5 up to a few ppbv (Asaf et al., 2009; Brown et al., 2009). Downwind of industrial activity, especially that related to petroleum production and storage, observed NO_3 lifetimes are limited by the presence of reactive hydrocarbons (Geyer et al., 2003; Stutz et al., 2010; Brown et al., 2011; Crowley et al., 2011).

In rural and forested environments, NO can be emitted from soils but is in general much less concentrated than in urban areas, and its mixing ratio is often close to 0 at night. In these environments, biogenic volatile organic compounds (BVOCs) can contribute a substantial fraction of the NO_3 reactivity. Unsaturated BVOCs such as monoterpenes have large rate constants for reaction with NO_3, e.g. $\sim 10^{-11}\,cm^3\,molecule^{-1}\,s^{-1}$ for limonene and $10^{-12}\,cm^3\,molecule^{-1}\,s^{-1}$ for α-pinene and β-pinene (Atkinson and Arey, 2003). In heavily forested areas with high monoterpene emission rates, NO_3 lifetimes may be reduced to a few tens of seconds (Rinne et al., 2012; Mogensen et al., 2015), resulting in efficient conversion of NO_x to organic nitrates and formation of secondary organic aerosol (Hallquist et al., 1999; Fry et al., 2014).

In the absence of any known, significant gas-phase reaction, the main sink of N_2O_5 at night is heterogeneous hydrolysis on aqueous aerosols, clouds and surfaces. The formation of particle-phase HNO_3 by this route results in repartitioning of NO_x from the gas to the condensed phase. Deposition of the particle nitrate formed is a substantial, permanent loss process for NO_x, resulting in reduced rates of photochemical O_3 production. Furthermore, if the aerosol particles contain chloride, the uptake of N_2O_5 can result in release of $ClNO_2$ and subsequently Cl atoms, which may enhance the rates of oxidation of hydrocarbons (Behnke et al., 1997; Osthoff et al., 2008; Bertram and Thornton, 2009; Thornton et al., 2010; Sarwar et al., 2012). The N_2O_5 uptake coefficient (overall efficiency of transfer from gas to particle phase) is largest for aqueous aerosols but depends on the composition of the aerosol (nitrate, sulfate and organic content) and humidity and possible organic coatings (Riemer et al., 2009) and is thus highly variable in time and space. Losses of NO_3 to aerosol or other surfaces are generally considered to be minor compared to its gas-phase losses and indirect losses via N_2O_5 uptake. In environments such as clean marine air masses where reactive partners for NO_3 are absent, lifetimes can become large and N_2O_5 losses to aerosol or surfaces may control the NO_3 levels via the equilibrium (Reactions R4a, b) (Heintz et al., 1996; Martinez et al., 2000).

Over the continents during the night, when the earth's surface does not receive energy by solar radiation, it cools down and the convective mixing which usually takes place during the day stops. This results in formation of a shallow, weakly mixed nocturnal boundary layer, with strong vertical stratification. Under such conditions, pronounced vertical gradients in NO_3 and N_2O_5 mixing ratios have been observed (von Friedeburg et al., 2002; Stutz et al., 2004; Brown et al., 2007) with ground-level emissions (both biogenic and anthropogenic) often resulting in lower NO_3 and N_2O_5 lifetimes, with cleaner air aloft (e.g. in the residual layer or free troposphere) often resulting in higher values. In all these different environments, the emission/formation rates of VOCs and aerosols and subsequent mixing are thus the key parameters controlling the NO_3 and N_2O_5 lifetimes.

In this paper, we describe a subset of an extensive suite of measurements obtained in the PARADE (PArticles and RAdicals, Diel observations of mEchanisms of oxidation) campaign (August–September 2011) at the top of a ~ 825 m high mountain situated between an urbanised flatland area and a forested mountainous area. A first campaign at this site (Crowley et al., 2010) during May 2009 found maximum NO_3 lifetimes of 10 to 15 min with mixing ratios up to 50 pptv for NO_3 and 500 pptv for N_2O_5. From the results of this first campaign it was concluded that at near-zero nighttime NO mixing ratios, the NO_3 lifetime was most likely controlled by emissions of BVOCs, which were, however, not measured. The heterogeneous loss of N_2O_5 was found to be only of limited importance in controlling NO_3 lifetimes. During PARADE, several hydrocarbons, both biogenic and an-

thropogenic, were measured as well as NO and also aerosol surface area (ASA) and chemical composition. We compare NO_3 lifetimes calculated using a steady-state approximation (based on the NO_3 production rate and mixing ratio) with those derived from the summed reactivity of individual trace gases and surfaces. For several campaign nights, we found that the steady-state lifetime significantly exceeded the lower limit of the NO_3 lifetime calculated from the summed reactivity and investigate potential causes of this.

2 Campaign location and measurement techniques

2.1 Site description

The PARADE campaign took place at the Taunus Observatory located on top of the Kleiner Feldberg mountain (50.22° N, 8.45° E) 825 m above sea level (a.s.l.). Local sites at the base of the mountains are at elevations of 120 ± 50 m. The station is used permanently by the environment and geological agency of the state of Hessen (HLUG) and the German weather service (DWD). The site has already been described (Handisides, 2001; Crowley et al., 2010), and only a short summary is given below. Directly (1–2 km) to the north-north-east and the south-east of the site are two similarly high mountains (Großer Feldberg at 878 m and Altkoenig at 798 m a.s.l.). The area in the north-west to north-east sector may be described as a relatively sparsely populated, partially forested rural region, whereas the south-west to south-east sector contains significant urban infrastructure including the densely populated cities of Frankfurt ($\sim$ 20 km to the south-east) and Mainz and Wiesbaden (20–30 km to the south-west). The site is directly surrounded (100 m radius) by a mix of coniferous trees (mainly spruce) and shrubs. Within a radius of 5 km from the site, the region is dominated by forest (coniferous, broad-leaved and mixed), especially to the north-east which has the lowest contribution from local agriculture and urban emissions. This is displayed in the land-use pie charts found in Fig. S1 in the Supplement. The same figure indicates that over a distance of 50 km, a significant fraction ($\sim$ 50 %) of the land area is used for agriculture.

The largest urban influence is found in the south-east sector for both 5 and 50 km distances to the site. In the northern sectors, the closest cities are located between 60 and 90 km away from the site and are significantly less populated than Frankfurt, Mainz and Wiesbaden. The heavily populated and industrialised *Ruhrgebiet* is about 130 km towards the north-west.

During the PARADE campaign, most instruments were located in the permanent laboratory facilities at the site. A platform on top of the building was used to house some instruments and the inlets outside at a height (from the ground) of about 8 m. Measurements central to this study (NO, NO_2, NO_3, N_2O_5, O_3, VOCs) were sampled via co-located inlets (< 5 m horizontal separation, < 1 m vertical separation). Aerosol measurements were made from a mobile laboratory (MoLa) (Drewnick et al., 2012) with its inlet at 10 m height, about 15 m distant from the main building. The instruments deployed are listed in Table 1, operational details, measurement uncertainties and detection limits are given in the next section. The MoLa also provided meteorological data (wind speed, wind direction, temperature, pressure relative humidity (RH) and global radiation) at 1 s resolution. The values were in generally good agreement with the lower frequency data sets reported by the DWD and HLUG.

Table 1. Instruments deployed during PARADE.

Species	Instrument	Inlet position
NO_3 and N_2O_5	CRDS	Tower
NO_3	LP-DOAS	Roof*
NO_2	CRDS	Tower
NO	CLD	Tower
VOCs	GC-MS/GC-FID	Tower
O_3	AirPointer	MoLa
Aerosol surface area	FMPS/APS	MoLa

* The telescope of the LP-DOAS set-up was located on the roof, about 2 m below the inlets of the point measurements. The retroreflectors were at different heights at a distance of $\sim$ 1.5 km towards the north (see Sect. 2.2.4).

2.2 Instrumentation

Below, we describe the instruments (and their overall uncertainties) used to make the critical measurements related to the calculation of NO_3 lifetimes. NO_2 and O_3, important for calculation of NO_3 production rates, were measured by multiple instruments, with good agreement. A comparison of three NO_2 data sets, including the one used here, is described in Thieser et al. (2016). Several O_3 data sets agreed to within about 10 % and the choice of data set for e.g. NO_2 or O_3 would not change the conclusions of this work.

2.2.1 NO_2, NO_3 and N_2O_5 measurements by cavity ring-down spectrometer (CRDS)

The two-channel thermal dissociation CRDS measuring NO_3 and N_2O_5 was deployed at this site during a previous campaign (Schuster et al., 2009; Crowley et al., 2010). Briefly, the CRDS uses a laser diode tuned to 662 nm to directly measure NO_3 in one channel at ambient temperature and the sum of ($NO_3 + N_2O_5$) in a second channel which is held at $\sim$ 100 °C, converting N_2O_5 to NO_3 (plus NO_2). Zeroing is performed by addition of NO (Reaction R6). The mixing ratio of N_2O_5 is then calculated from the difference in mixing ratios observed in each cavity. The CRDS instrument was located outside on the platform on top of the building in order to reduce inlet loss of NO_3. Air is drawn through a 1 m length of 0.5 in. (OD) PFA tube at 50 standard L min^{-1} and sampled (18 standard L min^{-1}) from the centre of the flow

via 0.25 in. PFA tubing into the two cavities of the CRDS. This set-up keeps inlet residence times short (≈ 0.1 s) and also helps avoid sampling of coarse particles and droplets. Corrections were applied to account for the losses of NO_3 on the filters, on the walls of the automatic filter changer and during passage through the cavities. The overall NO_3 transmission was ~ 68 % (Crowley et al., 2010). The instrument detection limit was 2 pptv in 1 s for NO_3 and approximately 5 pptv for N_2O_5. The total uncertainty was ~ 15 % for both NO_3 and N_2O_5, with the largest contributions arising from uncertainty in the NO_3 cross section (Orphal et al., 2003; Osthoff et al., 2007) and NO_3 losses.

During PARADE, NO_2 was measured using several instruments. We use data obtained using CRDS with a 405 nm diode laser as recently described in detail (Thieser et al., 2016). The instrument was zeroed using dry, synthetic air and corrections were made for humidity differences between the zero air and ambient. Typical ring-down times were ~ 30 µs and the instrument has a detection limit for NO_2 of ≈ 20 pptv in 1 min and an accuracy of 6 % where the dominant contribution is uncertainty in the NO_2 cross sections (Voigt et al., 2002).

2.2.2 VOC measurement by GC

VOCs were measured using two gas-chromatographic instruments with a mass spectrometer (GC-MS) and a flame ionisation detector (GC-FID). The GC-MS measured biogenic and aromatic hydrocarbons with online adsorption/thermal desorption (Markes International) connected to a gas chromatograph (Agilent GC 6890A) and a mass selective detector (Agilent MSD 5973 inert). The time resolution was ~ 1 h (35 min sampling time), and detection limits were around 1 pptv with an uncertainty of 10–15 %.

The GC-FID measured non-methane hydrocarbons (NMHC) using two coupled gas chromatographs (GC 5000 VOC and GC 5000 BTX; AMA instruments, Ulm, Germany). GC 5000 VOC was used for measurement of C2–C6 NMHCs and BTX for C6–C12. The detection limits ranged from 1 to 5 pptv, exceptions being ethane, ethene, propene, benzene and toluene with values of 8, 16, 9, 14 and 48 pptv respectively. The GC-FID was calibrated using a multi-gas mixture (National Physical Laboratory). Total uncertainty is close to 10 % for most trace gases with the exception of 1-pentane (15 %). The time resolution of the measurement is 60 min and the mixing ratio represents an average over a sampling period of 20 min.

2.2.3 NO, O_3 and CO_2

NO measurements were made with a modified commercial chemiluminescence detector (CLD 790 SR). Operation of this instrument during the PARADE campaign has recently been described (Li et al., 2015). The detection limit for this instrument is 4 pptv in 2 s with a total uncertainty of 4 %. The O_3 data set used in this work was obtained by a commercial AirPointer from Recordum Messtechnik GmbH. It was located in the MoLa and has a detection limit of ~ 1 ppbv (Drewnick et al., 2012) and an accuracy of 5 %. The O_3 inlet was situated a few metres above the MoLa, itself located 15 m metres away from the main tower. CO_2 was measured using non-dispersive differential broadband infrared absorption (LICOR 6262).

2.2.4 NO_2, O_3 and NO_3 measurements by long-path differential absorption spectroscopy (LP-DOAS)

In addition to the co-located point measurements described above, NO_2, O_3 and NO_3 were also measured by LP-DOAS over a light path of ~ 3 km. The telescope was situated on the same roof as the CRDS instruments (835 m a.s.l.) and was connected with a glass fibre to the laboratory where the light source, spectrometer and other components were located. Three reflectors were positioned at different heights (896.5, 927 and 959 m a.s.l.) to the north-north-east of the telescope on a tower at the Großer Felberg mountain (see Sect. 2.1) at a distance of 1.48 km from the light source. A fourth reflector was positioned on the Großer Feldberg mountainside at a distance of 1.23 km from the light source at 872 m a.s.l. A schematic showing the light paths in relation to the site topography is shown later when we discuss the results. The overall measurement accuracies are 2, 2 and 10 % for NO_2, O_3 and NO_3 respectively and are dominated by uncertainties in the absorption cross sections used.

2.2.5 Particle properties

Particle size information was obtained using MoLa instruments (see above). A fast mobility particle sizer (FMPS 3091, TSI, Inc.) and an aerodynamic particle sizer (APS 3321, TSI, Inc.) as well as an optical particle counter (OPC 1.109, Grimm) covered a particle size range from 5.6 nm to 32 µm. Aerosol was sampled at ambient RH and no correction was applied for hygroscopic growth. The ASA used for calculating rates of trace gas uptake was calculated from the combined FMPS and APS data sets or from the FMPS data alone (5–9 September). Generally, the bulk of the surface area (> 75 %) was found in particles of diameter < 450 nm as measured by the FMPS.

2.2.6 Radiosoundings

The planetary boundary-layer height was determined from radiosondes (GRAW, DFM-06), measuring temperature, relative humidity and position as already described for this campaign (Berkes et al., 2015). Each day, 4 to 10 radiosondes were launched from the summit of the Kleiner Feldberg starting approximately 1 h before sunrise and ending 1 h after sunset. From these data, the potential temperature was calculated and used to determine the type of the boundary layer (stable, neutral, turbulent).

3 Results and discussion

3.1 Meteorological conditions

During the 25 days of the PARADE campaign, the meteorological conditions were quite variable (see Fig. 1). As previously outlined (Phillips et al., 2012), the campaign can be separated broadly into three periods which are associated with different air-mass origins and the arrival of cold fronts. The first part of the campaign from 15 August to 26 August was characterized by a relatively high temperature (up to 25 °C) during the day and a variable day-to-day humidity and wind direction. The air originated from the sector between south and west, and back trajectory calculations using HYSPLIT (Draxler and Rolph, 2011) showed that it was located over the continent during the previous 48 h. Exceptions to this pattern occurred on a few days when air masses passed over the English Channel. The marine influence could be traced through the presence of enhanced $ClNO_2$ (measured using chemical ionisation mass spectrometry) during the night and early morning (Phillips et al., 2012).

The arrival of a cold front originating from the Atlantic on the evening of the 26 August marks the beginning of the second period of the campaign. Immediately following the arrival of this front, the daytime temperature decreased approximately by 10 °C and from 26 to 27 August the relative humidity was close to 100 % and the mountaintop was frequently in clouds. The average daily temperature then slowly increased to reach 20 °C on 3 September in the afternoon. Back trajectories of 48 h showed that from 28 August to 1 September the air was influenced by the Atlantic and the Benelux region. From 1 to 3 September, the 48 h air-mass origin was much closer to the site and stayed over the European continent. The arrival of another front on the evening of 2 September caused the temperature to drop again by 5 °C. Until the end of the campaign, the air originated from the UK and was characterised by low levels of solar radiation and high humidity as the mountaintop was frequently in clouds and fog.

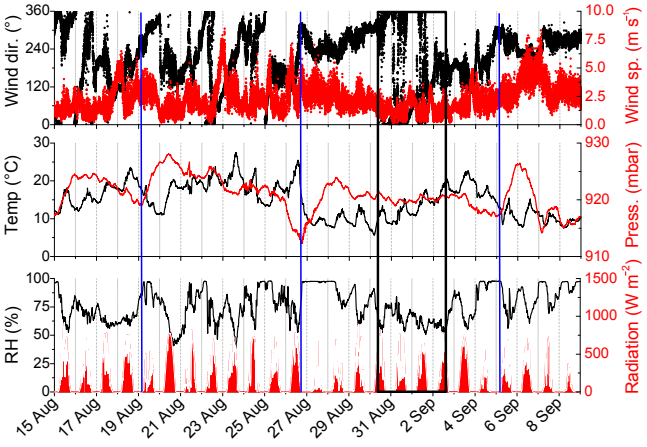

Figure 1. Meteorological parameters measured during the PARADE campaign. The vertical blue lines represent the arrival of cold fronts. The black box corresponds to the time period in which the longest NO_3 steady-state lifetimes were measured.

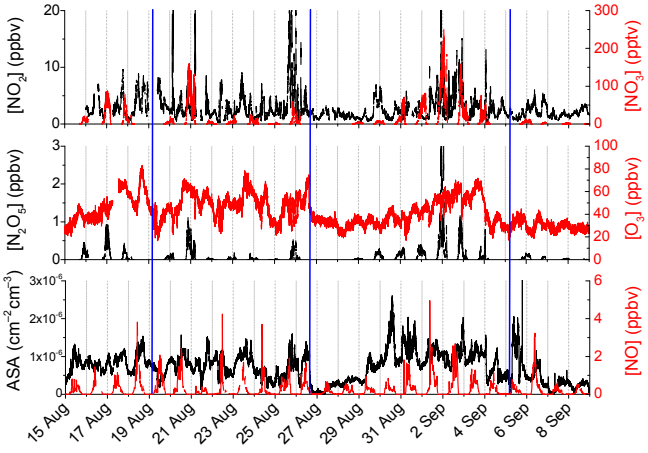

Figure 2. NO_2, NO_3, N_2O_5, O_3 and NO volume mixing ratios and aerosol surface area (ASA) measured during the PARADE campaign. The vertical, blue lines represent the arrival of cold fronts.

3.2 NO_2, NO_3 and N_2O_5 mixing ratios

The NO_3, N_2O_5 and NO_2 times series as well as that of O_3, NO and ASA are shown in Fig. 2. The mixing ratios of all measured nitrogen species were highly variable due to the close proximity of anthropogenic activity and its spatial/temporal heterogeneity (Crowley et al., 2010; Phillips et al., 2012). NO_2 mixing ratios were well above the detection limit during the whole campaign and ranged from 0.5 to more than 20 ppbv, with a campaign average of 2.7 ppbv during the day and 2.6 ppbv during the night. The highest, plume-like values of > 15 ppbv were spread over time periods of a few hours, occurred both day and night and were associated with polluted air masses arriving from the south-east (direction of Frankfurt). During passage of the cold fronts (vertical, blue lines in Fig. 2) the mountaintop was often in cloud with measured relative humidity close to 100 %. No N_2O_5 or NO_3 could be detected on these nights and O_3 levels were reduced to background levels of ∼ 25 ppbv during the following days. The low levels of solar radiation and photochemical activity reduced the maximum daytime mixing concentrations of NO to ∼ 0.5 ppbv.

As NO_2 is necessary for the formation of NO_3 and N_2O_5 (Reactions R1 and R4) and also because high levels are indicative of more polluted air masses which are usually associated with shorter NO_3 lifetimes, we examine the dependence of NO_2 on the local meteorological situation in more detail. A conventional wind rose is displayed in Fig. 3a; in Fig. 3b we plot the relative count frequency of the NO_2 mixing ratios indexed against wind direction. The north-east sec-

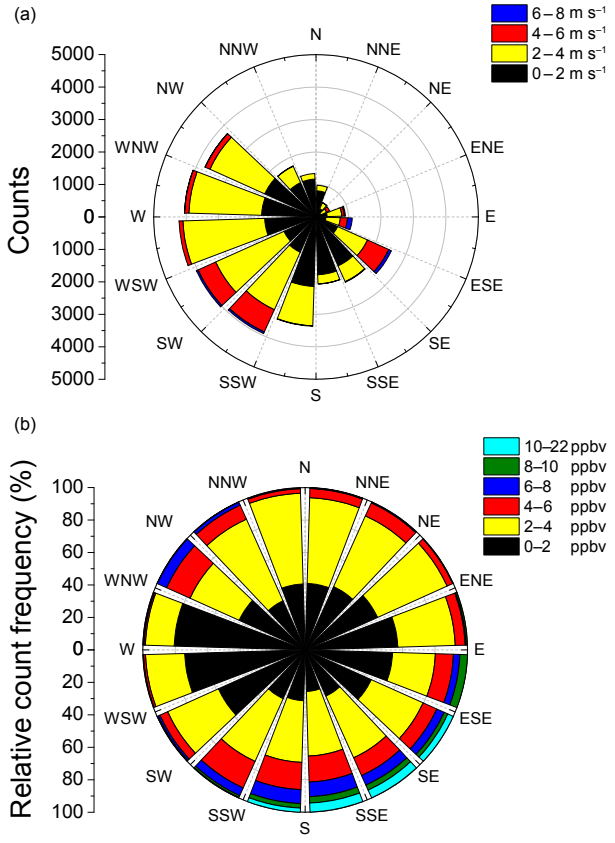

Figure 3. (a) Wind rose indicating the predominant wind direction and speeds throughout the campaign. **(b)** Relative count frequency of NO_2 mixing ratios against wind direction. Mixing ratios higher than 10 ppbv were encountered only for wind directions between east-south-east and south-south-west, reflecting the impact of the major local urban centres.

tor was the least represented with a time coverage of just 6 h. The most frequently encountered wind direction was west (≈ 200 h) but it is also where low NO_2 mixing ratios (< 2 ppbv, in black) were most frequently encountered. The sector east to south-south-west was characterised by frequent high NO_2 mixing ratios. It is the only sector which was associated with NO_2 mixing ratios greater than 10 ppbv, which reflects emissions originating from the three local cities of Frankfurt, Mainz and Wiesbaden. High NO_x levels measured in this sector were associated with the highest levels of anthropogenic hydrocarbons such as toluene.

$[NO_3]$ and $[N_2O_5]$ were highly variable during a single night and also from one night to the next, ranging from below the detection limit to 250 pptv for NO_3 and 3 ppbv for N_2O_5, which is significantly greater than previously measured at this site (Crowley et al., 2010). Precipitation periods were associated with $[NO_3]$ and $[N_2O_5]$ below the detection limit, which is likely a result of N_2O_5 uptake to droplets. The high variability in both $[NO_3]$ and $[N_2O_5]$ is partly due to the variability in their production rate. Figure 4 plots the mixing ratio of NO_3 (measured at night and at relative humidity lower than 97 %) and its production rate ($P(NO_3)$, in pptv s^{-1}; Fig. 4b) as calculated using Eq. (1) against the local wind direction. Both production rate and mixing ratio of NO_3 show higher values for air masses coming from the Frankfurt and the Mainz/Wiesbaden sectors.

3.3 NO_3 and N_2O_5 lifetimes

The steady-state method for estimating the lifetime of NO_3 is based on the assumption that, after a certain time following sunset, the NO_3 and N_2O_5 concentrations in a single air-mass build-up to a quasi-constant value. Steady state is reached when the sum of direct and indirect loss rate constants of NO_3, $L(NO_3)$ in s^{-1}, balances its production rate, $P(NO_3)$, so that

$$[NO_3]_{ss} = \frac{P\,(NO_3) + T_{in}\,(NO_3)}{L\,(NO_3) + T_{out}\,(NO_3)}, \quad (2)$$

where $P(NO_3)$ and $L(NO_3)$ are terms for NO_3 chemical formation and loss respectively and $T_{in}(NO_3)$ and $T_{out}(NO_3)$ represent the influence of transport of NO_3. Generally, the terms $T_{in}(NO_3)$ and $T_{out}(NO_3)$ are regarded as insignificant for radical species with chemical lifetimes on the order of minutes rather than hours or days. The simpler form, Eq. (3), for the steady-state approximation has therefore been used frequently in analysing NO_3 measurements (Noxon et al., 1980; Platt et al., 1980; Allan et al., 1999) and has been examined in detail (Brown et al., 2003). At steady state, the NO_3 lifetime (τ_{ss}) is then

$$\tau_{ss}\,(NO_3) = \frac{[NO_3]}{k_1\,[NO_2][O_3]} = \frac{1}{L_{ss}\,(NO_3)}. \quad (3)$$

The term $L_{ss}(NO_3)$ is the loss term of NO_3 corresponding to the steady-state lifetime. The loss term $L(NO_3)$ is the sum of processes removing NO_3 and is often simplified as in Eq. (4):

$$L\,(NO_3) \approx k_6[NO] + \sum([VOC]_i k_i) + 0.25\,K_{eq}[NO_2]\,\bar{c}\,ASA\,\gamma_{N_2O_5}, \quad (4)$$

where k_6 is the rate constant for Reaction (R6) (2.6×10^{-11} cm^3 $molecule^{-1}$ s^{-1} at 298 K; Atkinson et al., 2004) and K_{eq} is the equilibrium constant describing the relative concentrations of NO_3 and N_2O_5 under equilibrium for any given NO_2 concentration and temperature and is given by $K_{eq} = k_4/k_{-4}$. $\bar{c}$ is the mean thermal velocity of N_2O_5, k_i is the rate constant for reaction of NO_3 with a VOC, and $\gamma_{N_2O_5}$ is the uptake coefficient for N_2O_5 to aerosol with particle ASA (cm^2 cm^{-3}). Expressions (3) and (4) ignore loss of NO_3 via heterogeneous uptake and loss of N_2O_5 via gas-phase reactions, both of which are generally considered negligible, and consider NO_3 production path through oxidation of NO_2 by O_3 only. Later, we shall discuss the potential impact of other NO_3 production pathways.

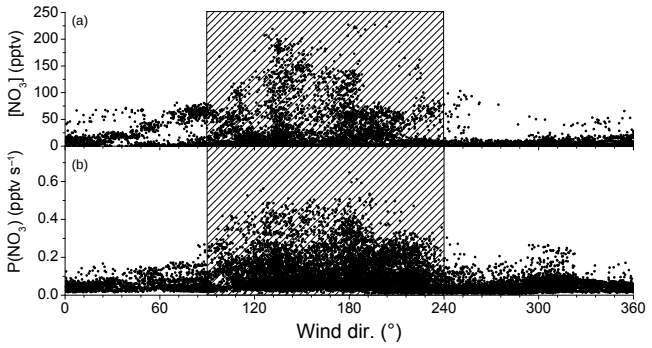

Figure 4. $[NO_3]$ and NO_3 production rate, $P(NO_3)$ from Reaction (R1), vs. wind direction. The grey areas correspond to the Frankfurt–Mainz–Wiesbaden sector. Temperature-dependent rate constants ($NO_2 + O_3$), used to calculate the NO_3 production term, were taken from an evaluation of kinetic data (Atkinson et al., 2004).

Implicit to this analysis is the assumption that steady state is achieved when the air mass reaches the measurement site. The strongest local sources of NO_2 and O_3 are likely to be the urban centres of Frankfurt, Mainz and Wiesbaden, all ~ 20 km distant in the southern sectors. As outlined above, there are no close, strong, continuous sources of anthropogenic pollution in the northern sectors. The NO_3 production rate as a function of wind direction in Fig. 4 confirms that the whole northern sector is relatively low in NO_3 precursors.

With typical wind speeds of between 2 and 5 m s^{-1} the transport times are at least 1 h from the major pollution sources. The time required to achieve steady state depends on the NO_3 production term and the overall loss frequency and is shorter when $P(NO_3)$ is low and the removal rate high. Numerical simulations were performed to test the validity of the steady-state approximation (Brown et al., 2003) and details are given in the Supplement (Fig. S2). The results indicate that achievement of steady state can indeed take longer than 1 h, when NO_3 lifetimes are long, especially when considering air masses with high NO_2 and O_3 e.g. as occasionally encountered from the southern sectors. During the first hours of nighttime, use of Eq. (3) may thus result in *underestimation* of the steady-state lifetime of NO_3.

The NO_3 lifetime can also be calculated from the production rate of NO_3 and the time derivatives of $[NO_3]$ and $[N_2O_5]$ as in Eq. (5) and thus does not require steady state to have been acquired (McLaren et al., 2010). The lifetime calculated via derivatives, $\tau_{DER}(NO_3)$, is given by

$$\tau_{DER}(NO_3) = \frac{[NO_3]}{k_1[NO_2][O_3] - \frac{d[NO_3]}{dt} - \frac{d[N_2O_5]}{dt}}. \quad (5)$$

As in the steady-state approximation, this method assumes that only chemical losses impact on NO_3 and N_2O_5 mixing ratios (negligible transport in and out of the sampled air mass) and that the sink terms are constant over the time step considered.

The campaign time series of the steady-state NO_3 lifetime is presented in Fig. 5a. The night-to-night variability of $\tau_{ss}(NO_3)$ is very high throughout the 3 weeks of the campaign, with an average value of 200 s (± 100 s) for NO_3. The longest lifetimes (~ 1 h for NO_3) were observed during 3 consecutive nights on 30 and 31 August and 1 September.

In Fig. S3 in the Supplement, we plot the NO_3 steady-state lifetime, $\tau_{ss}(NO_3)$ and the lifetime calculated using the derivatives method, $\tau_{DER}(NO_3)$. Both calculations agree well for the lowest NO_3 lifetimes (first period of the campaign from 15 to 26 August). This is expected, as the steady-state condition is readily fulfilled when the losses of NO_3 (or N_2O_5) are rapid. During the nights 30 and 31 August and 1 September, $\tau_{ss}(NO_3)$ is up to 2 times greater than $\tau_{DER}(NO_3)$. This is clearly not related to the effects outlined above which apply to the first hours of darkness but, as we discuss later, is associated with deviation from steady state during these periods. The derivatives method does not provide data for the whole campaign. $\tau_{DER}(NO_3)$ is sometimes very scattered and sometimes negative, which arises from noise on the derivative terms. However, on average, the ratio $\tau_{ss}(NO_3)/\tau_{DER}(NO_3)$ was 0.99 with ~ 66 % of the lifetimes agreeing within 30 %. The analysis and discussion below are based on the lifetimes obtained by the steady-state analysis.

The wind rose in Fig. 5b indicates that high values of $\tau_{ss}(NO_3)$ (≈ 1 h) were encountered irrespective of wind direction. This is initially surprising, as long NO_3 lifetimes values are not expected in air masses originating from the highly polluted sectors.

The short-term (hour-to-hour) variability was very high, as already described in Crowley et al. (2010) for this site. They describe the evolution of $\tau_{ss}(NO_3)$ over a single night in which the lifetime increased slowly after sunset to reach a roughly constant value around midnight. As steady state was predicted to be achieved on a much shorter timescale, and because other loss processes involving NO or heterogeneous loss of N_2O_5 were too slow, the increase in $[NO_3]$ and $\tau_{ss}(NO_3)$ was interpreted as being due to a slow decrease in the concentration of VOCs, though measurements of VOCs were not available to confirm this. During the PARADE campaign a number of VOCs and the ASA were measured, allowing us to calculate the overall loss rate constant of NO_3 using Eq. (4). As only a subset of the suite of organic species likely to be present at the site was measured, this calculation will provide a lower limit for the overall NO_3 loss rate (and thus an upper limit for its real lifetime).

3.3.1 Loss of NO_3 via reaction with NO

With an average O_3 mixing ratio of about 40 ppbv, the NO lifetime at night is about 5 min, so that, in the absence of local sources and photochemical degradation of NO_2, the NO mixing ratio will be close to 0 within an hour of sunset. This

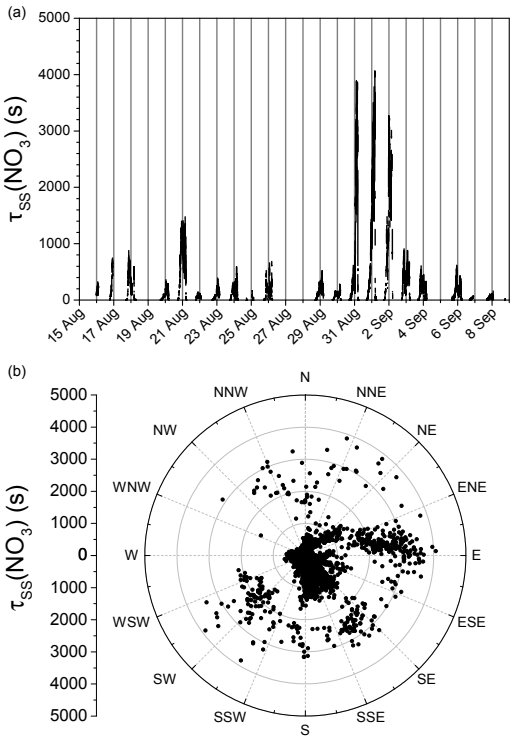

Figure 5. (a) $\tau_{ss}(NO_3)$ calculated according to Eq. (3). **(b)** $\tau_{ss}(NO_3)$ vs. wind direction.

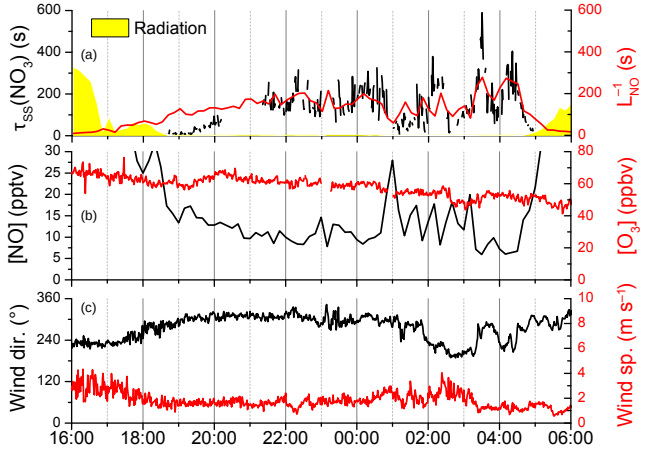

Figure 6. (a) $\tau_{ss}(NO_3)$ and inverse loss rate constant $(L_{NO})^{-1}$, for loss of NO_3 via reaction with NO during the night of 23 August. Panels **(b)** and **(c)** display the associated [NO], $[O_3]$, wind speed and wind direction data.

was the case for most of the nights during PARADE and NO measurements were below the (5 pptv) detection limit. On some nights, however, as exemplified in Fig. 6, 10–20 pptv of NO were measured, and between 21:00 UTC and sunrise $\tau_{ss}(NO_3)$ (Fig. 6a, black line) was consistent with that calculated from the NO reactivity as k_6[NO] (Fig. 6a, red line). During the period from 19:00 to 21:00 UTC the lifetime of NO_3 attributable to reaction with NO, τ(NO) is greater than $\tau_{ss}(NO_3)$, which may be due both to non-acquisition of steady state (for the first hour or so) and a contribution of other loss processes.

Figure 6 shows that the non-zero NO mixing ratios encountered on this night were in air masses associated with low wind speeds and may be a result of vehicle use on local roads or soil emissions.

3.3.2 Heterogeneous removal rate

The overall loss rate constant for NO_3 contains a contribution from indirect loss via the heterogeneous removal of N_2O_5 to particles as described by Eq. (4). In Fig. 7, we plot the calculated loss rate constant (s^{-1}) for NO_3 resulting from the uptake of N_2O_5 to particles (L_{HET} in blue) and compare it to the overall loss rate constant in steady state (L_{ss}, open circles) for two different nights. A simple temperature-dependent value of the uptake coefficient ($\gamma = 0.244–7.9 \times 10^{-4} T$) was used as recommended by IUPAC (Ammann et al., 2013). This expression is based on laboratory studies and results in a value at 283 K of $\sim 2 \times 10^{-2}$, which is larger than uptake coefficients obtained by analysis of both laboratory and field data in which the particle is not purely inorganic (Brown and Stutz, 2012). During periods when the NO_3 lifetime is long (e.g. $\tau_{ss}(NO_3) > 2000$ s or $L_{ss}(NO_3) < 5 \times 10^{-4}$ s^{-1}) as on the second period of the night of the 30 August (Fig. 7b), when using the γ parameterisation above, the losses of N_2O_5 to particles can account entirely for the observed lifetimes or even exceed the steady-state reactivity, which may be the result of using a high value for γ. On this night, NO was below the instrumental detection limit and was not considered for NO_3 losses. During periods when the NO_3 lifetime is shorter (e.g. on 5 September, Fig. 7a) the indirect, heterogeneous loss represents only a small fraction of the overall loss. More sophisticated parameterisations of the uptake coefficient, including e.g. the nitrate and chloride content of the particles and the existence of organic coatings (Bertram and Thornton, 2009), often fail to reproduce in situ measurements (Bertram et al., 2009) and indicate that γ is a large source of uncertainty in these calculations. However, even the use of values as large as 0.1 does not reproduce the shorter lifetimes and, as previously discussed for this site (Crowley et al., 2010), the remaining losses are likely due to direct reactions of NO_3 with VOCs.

3.3.3 Loss of NO_3 via reaction with VOCs

The VOCs measured during PARADE are listed in Table 2 together with their rate constants (at 298 K) for reaction with NO_3. Among the trace gases listed, only a few of them (at high concentrations or with large rate constants for reaction with NO_3) contributed significantly to the loss of NO_3 and

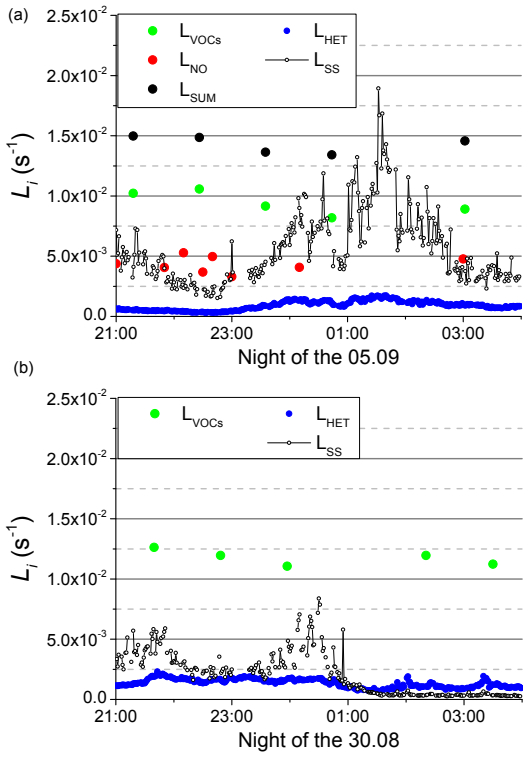

Figure 7. (a) Individual ($L_{VOCs} = \sum k_i[VOC]_i$, $L_{NO} = k_6[NO]$ and L_{HET}) and summed NO_3 loss terms (L_{SUM}) for the night of 5 September, together with the loss rate constant of NO_3 in steady state (L_{ss}). **(b)** Individual ($L_{VOCs} = \sum k_i[VOC]_i$, $L_{NO} = k_6[NO]$ and L_{HET}) and summed NO_3 loss terms (L_{SUM}) for the night of the 30 August, together with the inverse of the steady-state lifetime of NO_3 (L_{ss}). L_{VOCs}, L_{NO}, L_{HET} and L_{ss} are given in the original time resolutions (respectively 30, 10, 1 and 1 min). To calculate L_{SUM}, high-resolution L_{NO} and L_{HET} were interpolated to the L_{VOCs} time grid.

are highlighted in bold. Further discussion will focus on these VOCs. Apart from isoprene (up to 200 pptv), the mixing ratios of VOCs which are reactive towards NO_3 were generally below 100 pptv (see Supplement, Fig. S4). A clear diel cycle was observed for isoprene and during the warmer first and last parts of the campaign daytime mixing ratios were up to 5 times higher than during the night. For the monoterpenes the diel cycle was less pronounced and on two nights (4–5 September and 5–6 September) large mixing ratios were observed during the night (e.g. > 50 pptv for myrcene and limonene), which were not accompanied by increases in isoprene. As expected, during colder, rainy periods, the BVOCs were less abundant and showed a weaker diel variation.

For each monoterpene, the NO_3 loss rate constant for reaction with VOCs ($L_i = k_i[VOC]_i$ where k_i is the rate constant for each VOC) is plotted together with the steady-state NO_3 total reactivity ($L_{ss}(NO_3)$) and the VOCs summed reactivities (including alkanes and alkenes) in Figs. 7 and S5. The rate coefficients for reaction of NO_3 with the VOCs were derived from the temperature-dependent expressions given by IUPAC and were calculated at each time step of the data set. Figure S5 shows that, over almost the whole campaign, the steady-state loss rate constants L_{ss} (open circles) are significantly lower than those calculated by summing the individual contributions of the VOCs (L_{VOCs}, dashed line). Indeed, during the 3 nights in which very long NO_3 lifetimes were encountered, L_{ss} is approximately 4 to 5 times lower than that expected from the summed VOCs. In other words, within the steady-state framework used here and using the NO_3 production term, $k_1[NO_2][O_3]$, the observed mixing ratios and lifetimes of NO_3 are incompatible with the VOC measurements.

The divergence between the steady-state loss rates and that obtained by summing the losses with each VOC is exacerbated when one considers that the VOCs measured in PARADE cover only a fraction of those present in the air so that L_{VOCs} must strictly be regarded as a lower limit. As exemplified in Figs. 7 and S5, summing the individual loss rate constants due to reaction of NO_3 with NO (L_{NO}), the complete set of VOCs (L_{VOCs}) and indirect loss via heterogeneous uptake of N_2O_5 to available particles (L_{HET}) results in an air-mass reactivity that is larger than that derived from the steady-state calculations, i.e. the NO_3 lifetime is longer than expected (or its concentration higher). Generally, the opposite is observed and missing reactivity is assigned e.g. to VOCs that were not measured. Below, we examine possible explanations for this, including the breakdown of the steady-state assumption, the potential role of other chemical routes to NO_3 generation and meteorological effects.

3.3.4 NO_3 production rate

So far, our calculations have been based on the assumption that NO_3 is generated solely in the reaction between NO_2 and O_3 (Reaction R1, see Sect. 3.3). If NO_3 is only formed via Reaction (R1), the uncertainty associated with $P(NO_3)$, propagated from those of $[NO_2]$ and $[O_3]$ is approximately 8 %. The good agreement between several devices for measurement of both NO_2 and O_3 indicates that the term $k_1[NO_2][O_3]$ is indeed well defined. As indicated in Sect. 1, other sources of NO_3 are known but are generally regarded as negligible. The reaction of OH with HNO_3 (Reaction R2) generates NO_3 at ∼ 100 % yield but, even assuming nighttime concentrations of hydroxyl radicals of 1×10^5 molecule cm^3 and 2 ppbv of HNO_3, the NO_3 production rate is only ∼ 1 % of that from Reaction (R1). In the absence of sunlight, the formation of NO_3 from the photolysis (Reaction R3) of halogen nitrate, $XONO_2$ (where X = Cl, Br or I), will not contribute at nighttime. A further possible source of nighttime NO_3 and cause for error in steady-state lifetime estimations could be the rapid recycling of NO_3 from the products formed in its initial reaction with BVOCs, as has been seen for the OH radical (Lelieveld et al., 2008; Taraborrelli et al., 2012). The organic nitrates formed as first-generation products when NO_3 reacts with biogenic VOCs

Table 2. VOCs measured using GC-MS and GC-FID during PARADE.

GC-MS VOCs	$k(NO_3+VOC)$[a]	Maximum mixing ratio (pptv)	GC-FID VOCs	$k(NO_3+VOC)$[a]	Maximum mixing ratio (ppbv)
Isoprene	7.0×10^{-13}	220	Ethane	$<1\times10^{-17}$	7.2
α-Pinene	6.2×10^{-12}	170	Ethene	2.1×10^{-16}	15
Myrcene	1.1×10^{-11}	70	Propane	$<7\times10^{-17}$	2.5
Limonene	1.22×10^{-11}	130	Propene	9.5×10^{-15}	20
p-Cymene	1.0×10^{-15} [b]	20	*i*-Butane	1.1×10^{-16} [b]	1.3
Benzene	$<3\times10^{-17}$ [b]	230	*n*-Butane	4.6×10^{-17}	1.4
Toluene	7.0×10^{-17} [b]	420	cis-2-Butene	3.5×10^{-13}	0.6
Ethylbenzene	$<6\times10^{-16}$ [b]	80	*i*-Pentane	1.62×10^{-16} [b]	1
m-Xylene	2.6×10^{-16} [b]	130	*n*-Pentane	8.7×10^{-17} [b]	1
p-Xylene	5.0×10^{-16} [b]	65	1-Pentene	1.5×10^{-14} [b]	1.9
o-Xylene	4.1×10^{-16} [b]	75	Butadiene	1.0×10^{-13} [b]	10.6

[a] Rate constants (cm^3 $molecule^{-1}$ s^{-1}) at 298 K taken from the latest evaluation (Atkinson et al., 2006; Ammann et al., 2016) unless noted otherwise.
[b] Rate constants (cm^3 $molecule^{-1}$ s^{-1}) taken from Atkinson and Arey (2003).

are, however, believed to be chemically stable and there is no obvious pathway for rapid re-release of NO_3 once formed.

We now consider a further nighttime process forming NO_3 via the oxidation of NO_2 by stabilised Criegee intermediates (sCIs), which are formed in the atmosphere by the reaction of O_3 with biogenic and anthropogenic alkenes (Johnson and Marston, 2008). This may be especially relevant when observing apparently long NO_3 lifetimes (i.e. high concentrations) in the presence of reactive VOCs.

The possibility of NO_3 generation via sCI reaction with NO_2 was first raised several years ago (Fenske et al., 2000; Presto and Donahue, 2004), though in the early studies, which were unable to detect Criegee radicals directly, uncertainties regarding the products and the rate constant were large. In recent work (Welz et al., 2012) on the reaction between the simplest sCI (CH_2O_2) and NO_2, a large rate constant ($7^{+3}_{-2}10^{-12}$ cm^3 $molecule^{-1}$ s^{-1}) was determined. The authors hypothesised that the reaction between other sCI and NO_2 might have similar rate constants. A further study (Stone et al., 2014) reports a rate constant ($1.5\pm0.5\times10^{-12}$ cm^3 $molecule^{-1}$ s^{-1}) for the same reaction and detected HCHO as product, consistent with an O-atom transfer from sCI to NO_2 to form NO_3. Subsequently, the formation of NO_3 (and N_2O_5) resulting from the photolysis at 248 nm of a mixture of CH_2I_2, O_2 and NO_2 was attributed to the reaction between CH_2O_2 and NO_2 (Ouyang et al., 2013). Whether sCI can contribute significantly to nighttime NO_3 formation or not depends on the assumption that all sCIs react with a similar rate coefficient to CH_2O_2, that NO_3 is formed at high yield and that sufficient sCIs are present in the nighttime boundary layer. In Table 3, we assess the three reactions that could have contributed to NO_3 formation during PARADE. We take a generic rate coefficient for $sCI + NO_2$ that lies between the literature determinations (Welz et al., 2012; Stone et al., 2014) and assume 100 % product yield for formation of NO_3.

Table 3 shows that, whereas the reaction between OH and HNO_3 can safely be neglected, the reaction between sCI and NO_2 can represent a significant fraction of the total rate of production of NO_3 if sCIs are present at ~0.1 pptv during night. This reflects the fact that, although Criegee radicals are expected to be present at concentrations 4–6 orders of magnitude less than those of O_3, the rate constant for reaction with NO_2 is ~5 orders of magnitude larger.

The rate of formation of sCIs in the boundary layer depends on both the concentration and nature of the organics reacting with O_3 to form it and is expected to be very variable. Likewise, the sink reactions of sCIs are difficult to predict, though reactions with water vapour, SO_2 and NO_2 are expected to be important (Vereecken et al., 2012). Boundary-layer mixing ratios of sCIs are thus associated with great uncertainty. Based on a steady-state approach, sCI mixing ratio up to 0.03 pptv have ben calculated for the PARADE campaign (Bonn et al., 2014), i.e. within the range of values used in Table 3. Recent measurements in a Boreal forest environment estimated sCI mixing ratios to be 0.0025 to 0.04 pptv (Taipale et al., 2014) and sCIs have been tentatively identified (Mao et al., 2012) as the source of an interfering signal in ambient measurements of OH that may approach 0.2 pptv (Novelli et al., 2014). As not all ambient sCIs will decompose to OH within such instruments, the wider implication is that pptv amounts of sCI may be present.

To calculate the influence of sCI-induced formation of NO_3 during the PARADE campaign we recalculated the NO_3 production rate assuming two different sCI concentrations at the limits of the range listed in Table 3 and using the rate constant given. In Fig. 8 we display the calculated steady-state lifetime without sCI reactions forming NO_3 (black symbols) and the effect of using a low sCI concentration (τ_{LsCI}, blue

Table 3. Reactions producing NO_3.

Reaction	Mixing ratio first reactant	Mixing ratio second reactant	Rate coefficient (298 K)[a]	$P(NO_3)$[b]
$O_3 + NO_2$	20–50 ppbv	0.5–5 ppbv	3.5×10^{-17}	$(0.9–220) \times 10^{-3}$
$OH + HNO_3$	$(1–10) \times 10^{-2}$ pptv	0.5–5 ppbv	1.5×10^{-13}	$(1.9–190) \times 10^{-5}$
$sCI + NO_2$	0.01–0.1 pptv	0.5–5 ppbv	5.0×10^{-12}	$(0.6–6) \times 10^{-3}$

[a] Units of cm^3 $molecule^{-1}$ s^{-1}. [b] Units of pptv s^{-1}.

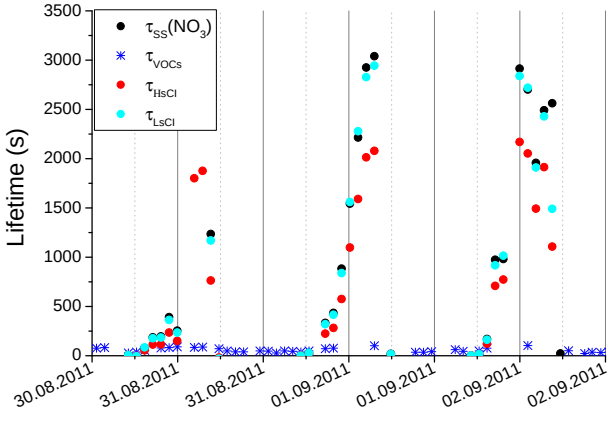

Figure 8. NO_3 steady-state lifetimes calculated using different production terms. Black data points: only $NO_2 + O_3$ forms NO_3. Blue circles: additional formation from 0.01 pptv sCI reacting with NO_2. Red data points: additional formation from 0.1 pptv sCI reacting with NO_2. The inverse of L_{VOCs} is indicated by the blue stars. Similar to Fig. 7, all data were interpolated to the VOC time axis; hence the low time resolution.

symbols) or a high concentration (τ_{HsCI}, red symbols). The resultant reduction in the calculated steady-state lifetime of NO_3 is significant when using the higher values of [sCI]. For example, on 31 August, the largest value of $\tau_{ss}(NO_3)$ would be reduced from 3000 s (black data points) to 2000 s (red data points) when assuming 0.1 pptv of sCI. However, in order to bring the steady-state lifetime into agreement with that based on the VOC measurements (green symbols), a sCI mixing ratio of 4 pptv would be required. Our present knowledge of Criegee formation and loss mechanisms under atmospheric conditions precludes accurate assessment of their role in forming NO_3 at nighttime, though sCI mixing ratios as large as 4 pptv appear (at present) unlikely, though not impossible.

3.3.5 Meteorological considerations

We have shown that, while uncertainties in some parameters required for calculation of NO_3 lifetimes exist, they are likely to be insufficient to explain the high concentrations (and lifetimes) of NO_3 during the nights of 30 August to 1 September. Close examination of the NO_3 lifetime on these nights (e.g. Fig. 9) reveals an especially strong gradient, with $\tau_{ss}(NO_3)$ values increasing e.g. by 500 to 600 % over the course of an hour. Simultaneously, $\tau_{ss}(N_2O_5)$ values (not shown) increase by 200 %. The smaller increase in $\tau_{ss}(N_2O_5)$ is due to a simultaneous decrease of $[NO_2]$ by 50 %, thus shifting the equilibrium towards NO_3. The large gradient in $\tau_{ss}(NO_3)$ cannot be attributed to a decrease in the mixing ratios of reactive trace gases, which were much less variable (see above). We therefore consider the possibility that the long lifetimes observed on these nights are related to sampling air masses from a low-lying residual layer (i.e. from above a particulary shallow nocturnal boundary layer) which, especially at low wind speeds, is decoupled from ground emissions of NO_x and VOCs, allowing NO_3 and N_2O_5 to build up to higher levels and would also help to explain the lack of dependence on wind direction.

The hypothesis that sampling of residual-layer air is responsible for the long steady-state lifetimes of NO_3 and their apparent incompatibility with the VOC measurements is examined in detail in Fig. 9. Here, the time profiles of $\tau_{ss}(NO_3)$, NO_2, O_3, CO_2, and ASA and some meteorological parameters are plotted for the night of 30 August. The night from 30 to 31 August can be divided into two distinct periods. Between 21:00 and 00:30 UTC (first period) $\tau_{ss}(NO_3)$ was roughly constant at an average value of about 150 s. After this, we observed a large increase in the NO_3 steady-state lifetime between ∼ 00:30 and 01:30 UTC, followed by period 2 (01:30 UTC until dawn) in which $\tau_{ss}(NO_3)$ was consistently close to 3000 s.

The transition from the shorter (period 1) to longer (period 2) lifetimes is accompanied by a decrease in the NO_2 mixing ratio from about 2.5 to 1 ppbv, a ∼ 2 ppmv decrease in CO_2, an increase in O_3 from ∼ 15 to 25 ppbv and a ∼ 30 % increase in particle surface area. Changes in the local wind direction (at ∼ 20 m height) between the clean northern sector to the anthropogenically polluted south sector during this second period did not impact the NO_x levels or the NO_3 lifetime.

These observations are consistent with air from the residual layer being sampled during the second period. Higher levels of O_3 and particles, formed during the previous day in the turbulently mixed boundary layer, are expected in the residual layer compared to the shallow, nocturnal boundary

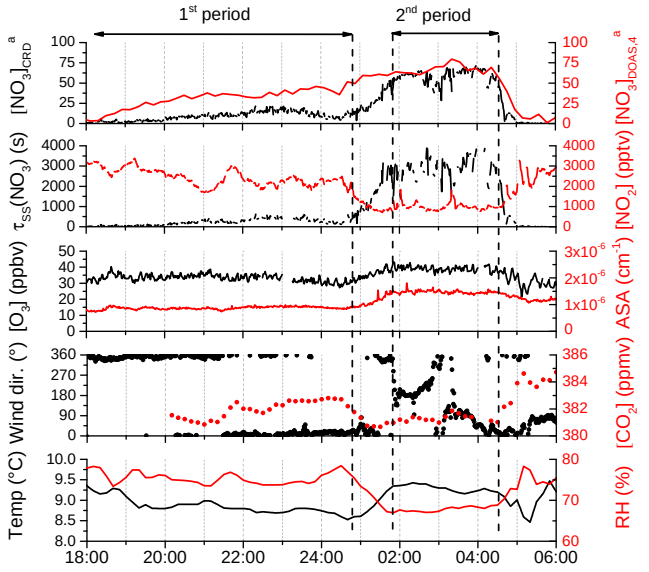

Figure 9. Detailed view of the night of the 30 August indicating two periods corresponding to different NO_3 lifetime regimes. The trends in NO_3 lifetime, CO_2, NO_2, O_3, RH and aerosol surface area (ASA) indicate a transition from boundary-layer to residual-layer air between ∼ 00:30 and 01:30 UTC in the morning. Sunrise was at about 05:00 UTC. [a] Units of pptv.

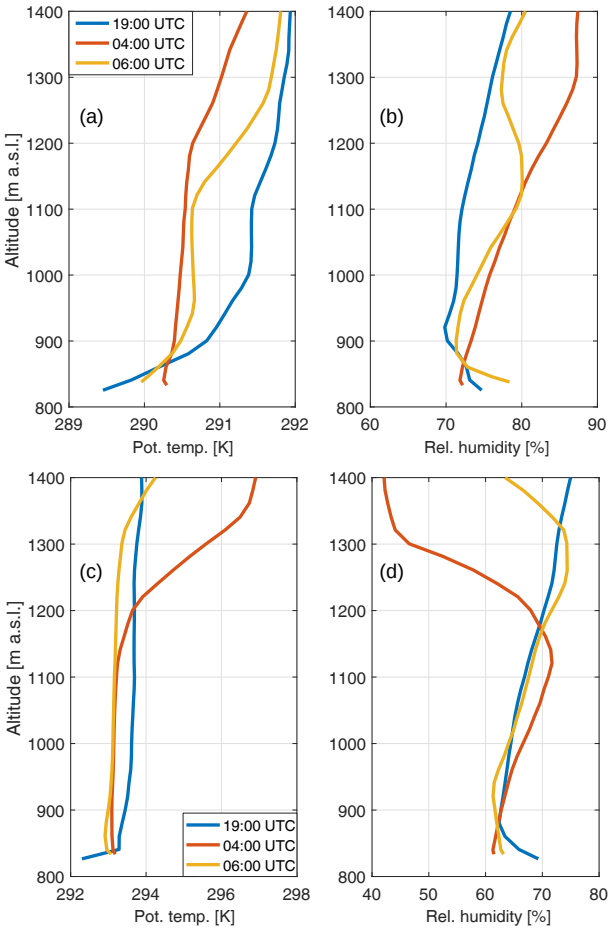

Figure 10. Vertical profiles of the potential temperature **(a)** and the relative humidity **(b)** during the first period on 30 August at 19:00 UTC (blue), as shown in Fig. 9, and on 31 August at 04:00 UTC (red) and 06:00 UTC (orange, after sunrise) during the second period. **(c, d)** Same as above but for 31 August to 1 September.

layer in which dry deposition is important for both. Conversely, levels of NO_2, formed from oxidation of ground-level NO emissions are expected to be higher in the lower levels (Stutz et al., 2004; Brown et al., 2007) and thus decrease when sampling air from the residual layer. The second period is also marked by a significant drop in relative humidity (from ∼ 80 to 65 %) and an increase in the temperature of ≈ 1 °C. The former is expected as relative humidity decreases above the nocturnal boundary layer. A correlation between increasing NO_3 lifetimes and temperature has been observed previously (Crowley et al. 2010) and was attributed to downward movement of higher air masses during an inversion.

Figure 10a and b show profiles of the potential temperature and relative humidity within the first period at 19:00 UTC and within the second period at 04:00 UTC from 30 to 31 August. The temporal development of the temperature and the relative humidity profiles agrees well with the near-surface observations. The profiles of the potential temperature show a change from stable stratification (potential temperature increase with height) to neutral stratification (potential temperature is constant with height) which is an additional indication that the measurements within period 2 were obtained within the residual layer. The same temporal development of the potential temperature profiles was observed 24 h later (Fig. 10a, b), when again the NO_3 lifetime was enhanced. On both nights, the lack of a switch in sign of the RH gradient with height at 04:00 UTC contrasts with the profiles at 19:00 and 06:00 UTC which show clear evidence for a switch from boundary layer to residual layer some 50 to 100 m above the summit. Between 31 August and 2 September we observed no nocturnal build-up of CO_2, which strongly contrasts the periods prior to and after this period (see Fig. S6) and again indicates that this period with the longest NO_3 lifetimes is associated with residual-layer air.

When sampling from the residual layer, we would expect that the observed increase in O_3 and ASA and simultaneous decrease in NO_2 and RH would be accompanied by a decrease in those biogenic trace gases, which are reactive towards NO_3. Indeed, if we take the measured NO_3 mixing ratio of 200 pptv on 2 September, we calculate that the lifetime of biogenics such as limonene should be of the order of only a few minutes in the residual layer. The simultaneous measurement of both high NO_3 steady-state lifetimes and terpene mixing ratios can now be explained if we consider that the terpene emissions are only local, i.e. from trees that are close

to the top of the mountain (and our inlet) and thus also within the residual layer. Such local emission (e.g. within 30 m of the inlet) does not allow the NO_3+ terpene chemistry to go to steady state so that only a fraction of the NO_3 (and terpene) are consumed. The extent of reaction will be related to the location of the emission relative to the inlet and local wind speeds and is likely to be highly variable.

So far, we have assumed that NO_3 (or N_2O_5) levels aloft (i.e. in the residual layer) are enhanced w.r.t. the boundary layer. As NO_3 (and also NO_2 and O_3) was measured by LP-DOAS at different heights, this data set should give some insight into the occurrence and extent of vertical gradients in NO_3 concentrations. In Fig. 9 we plot a data set obtained using the LP-DOAS. In the first period (until ∼ 00:30 UTC), the DOAS measurements of NO_3 at the highest altitude were significantly larger (factor of ∼ 5 at 24:00 UTC) than those measured by the CRDS. This difference in concentration disappeared during the second phase (01:30 until 04:00 UTC) when both instruments measured high NO_3, thus supporting the concept that the top of the mountain is in the residual layer during this period. Below, we compare the CRDS and DOAS measurements in more detail.

3.3.6 Comparison of NO_3 lifetimes derived from CRDS and LP-DOAS instruments

As mentioned in Sect. 2.2 the LP-DOAS measurements were conducted using a total of four light paths. For this analysis we compare data retrieved from only the lowest (835 to 872 m a.s.l.) and highest (835 to 959 m a.s.l.) levels (see Fig. 11). By comparison, the height of the CRDS inlet was ∼ 838 m a.s.l.

We refer to the lower and higher levels as DOAS 1 and DOAS 4 respectively. Steady-state NO_3 lifetimes were calculated in the same way as described above for the CRDS data set, using the NO_2 and O_3 data obtained from the DOAS instrument at those two different levels. Because of the short horizontal (1.5 km) and vertical (∼ 125 m) range of the DOAS light paths, the integrated temperature over both light paths is assumed to be the same as the temperature measured at the Kleiner Feldberg hilltop and these values were used to calculate the rate constant (k_1) for NO_3 production. Note that differences in temperature of a few Kelvin do not impact significantly the rate constant, k_1.

In Fig. 12 we plot the NO_3 mixing ratios and steady-state lifetimes obtained on two different nights, 1–2 and 5–6 September, by the CRDS and LP-DOAS instruments. While the night of 5–6 September shows large differences between the mixing ratios reported by the CRDS and LP-DOAS instruments, and a strong vertical gradient in NO_3, good agreement, i.e. a weak (or 0) gradient, is observed on 1–2 September. The LP-DOAS measurements of the NO_2 (Thieser et al., 2016) and O_3 mixing ratios (Fig. 13) reveal little or no difference between the highest and lowest light paths over the whole campaign, so that the NO_3 production term

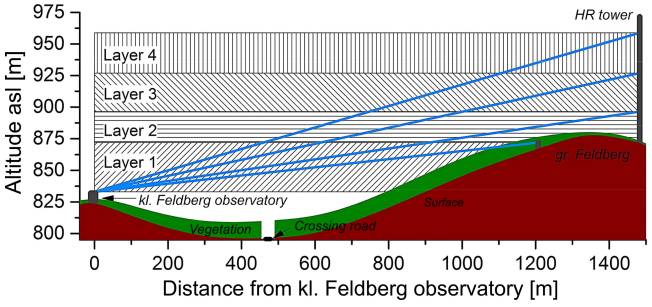

Figure 11. Schematic diagram of the LP-DOAS light paths deployed during the PARADE campaign, with the Kleiner Feldberg on the left and the Grosser Feldberg on the right. The LP-DOAS data sets used in this work are those obtained from the lower-most and upper-most light paths.

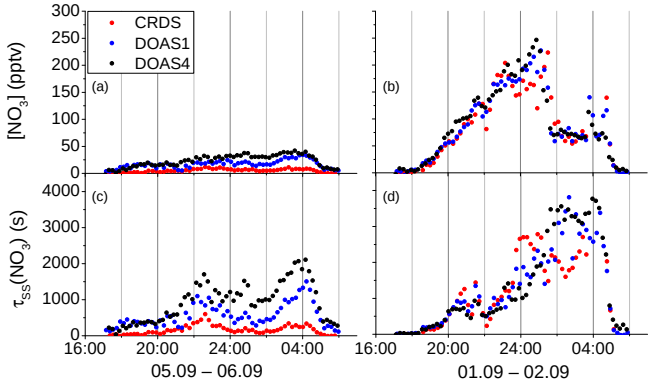

Figure 12. $[NO_3]$ **(a)** and $\tau_{ss}(NO_3)$ **(c)** using CRDS data (red), lowest LP-DOAS light path (DOAS 1) and highest LP-DOAS light path (DOAS 4) for the night of 5–6 September. **(b, d)** As for the left-hand plot but showing data for the night of 1–2 September.

was roughly constant with altitude. The clear dependence of the NO_3 mixing ratio on height on 5–6 September is thus due to variation in the NO_3 loss term. Figure 12c indicates a factor of up to ∼ 5 increase in NO_3 lifetime when comparing the LP-DOAS data at the highest level to the CRDS measurements.

In Fig. 14a we plot the campaign NO_3 mixing ratios measured by the CRDS and DOAS 4 vs. the DOAS 1 data set. As mentioned previously and illustrated in Fig. 11, the LP-DOAS light source and the CRDS inlet were co-located at a height of ∼ 835 m whilst the LP-DOAS retroreflectors were at ∼ 959 and 872 m. All data which were above the detection limit (10 pptv for LP-DOAS and 5 pptv for the CRDS) were included. The coloured lines (black, blue and red) represent slopes of 0.5, 1 and 2 respectively. Nearly all of the black data points $[NO_3]_{DOAS4}$ have slopes between 1 and 2, indicating that, on average, $[NO_3]$ is higher aloft, consistent with previous observations of positive vertical gradients in NO_3 (Stutz et al., 2004; Brown et al., 2007). At large mixing ratios, i.e. for $[NO_3]_{DOAS1} > 100$ pptv, the al-

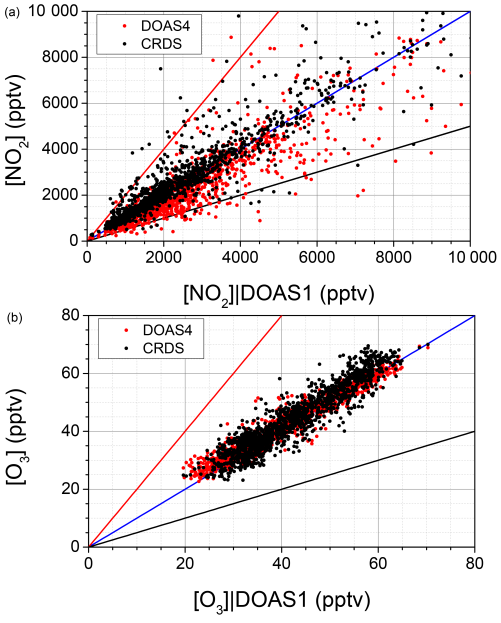

Figure 13. (a) Comparison between $[NO_2]_{CRDS}$, $[NO_2]_{DOAS4}$ and $[NO_2]_{DOAS1}$ (whole campaign). **(b)** Comparison between $[O_3]_{CRDS}$, $[O_3]_{DOAS4}$ and $[O_3]_{DOAS1}$ (whole campaign). Blue lines have a gradient of 1, red lines a gradient of 2 and black lines a gradient of 0.5.

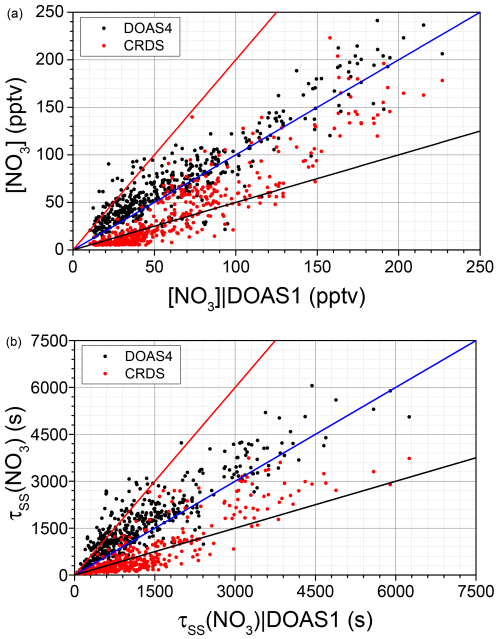

Figure 14. (a) $[NO_3]_{CRDS}$ (red) and $[NO_3]_{DOAS4}$ (black) vs. $[NO_3]_{DOAS1}$. **(b)** $\tau_{ss}(NO_3)_{CRDS}$ (red) and $\tau_{ss}(NO_3)_{DOAS4}$ (black) vs. $\tau_{ss}(NO_3)_{DOAS1}$. Coloured lines on both panels represent slopes of 0.5, 1 and 2 (black, blue and red respectively).

titude dependence on the $[NO_3]$ is weaker and the black points are closer to the blue line (slope of 1). The ratio between $[NO_3]_{CRDS}$ and $[NO_3]_{DOAS1}$ also shows some dependence on the NO_3 mixing ratio. When the NO_3 mixing ratios are low, the ratio CRDS / LP-DOAS is also low and generally less than 0.5. In extreme cases, the $[NO_3]_{CRDS}$ values are close to a few pptv or below the detection limit while $[NO_3]_{DOAS1}$ measured as high as 40 to 50 pptv. To illustrate this, for NO_3 steady-state lifetimes of < 1500 (i.e. all nights except for 30 August–2 September) the average value of the $[NO_3]_{DOAS4}/[NO_3]_{DOAS1}$ ratio is 1.23 ± 0.07, whereas for NO_3 steady-state lifetimes of > 1500 s we derive a $[NO_3]_{DOAS4}/[NO_3]_{DOAS1}$ ratio of 0.95 ± 0.05.

Both $\tau_{ss}(NO_3)_{CRDS}$ and $\tau_{ss}(NO_3)_{DOAS4}$ data sets (Fig. 14b) show the same trends as the one described for $[NO_3]$. At low $\tau_{ss}(NO_3)_{DOAS1}$ the black and red points are respectively closer to the black and red lines and as $\tau_{ss}(NO_3)_{DOAS1}$ increases to the highest values the data points are all closer to the blue line. The apparent dependence of the NO_3 mixing ratios and lifetime on the NO_3 concentrations reflects the fact that, when NO_3 is high, both instruments are sampling the residual layer in which NO_3 levels are expected to be higher and gradients in NO_3 are expected to be weaker than found close to the surface (Brown et al., 2007).

In summary, the data shown in Fig. 9 and the LP-DOAS measurements of NO_3 at different altitudes provide compelling evidence for a low-lying residual layer (or very shallow nocturnal boundary layer) being responsible for the occasional observation of high NO_3 mixing ratios seen by the ground-level CRDS instrument and the associated long steady-state lifetimes. This layer will be most stable and thus best decoupled from the underlying boundary layer when wind speeds are low. The DOAS measurement of concentration at different altitudes does not contain information about the vertical exchange and mixing itself. Any estimation of vertical mixing for a reactive trace gas like NO_3 would require a chemical model with transport, which would be difficult for such an environment with complex topography like the Kleiner Feldberg.

4 Conclusions

We observed highly variable NO_3 concentrations and lifetimes at a mountain site in south-west Germany. Measurements of NO_3, its precursors and its sink reactions (both direct and indirect) enabled assessment of the processes (both chemical and meteorological) influencing its steady-state lifetime. We found that, during several nights, the observed steady-state lifetime was frequently larger than expected based on measured gas-phase reactants such as VOCs and NO. We have shown that an enhancement in the NO_3 production term via the reaction between Criegee and NO_2 may be significant but unlikely to explain the discrepancy. The periods with the highest apparent NO_3 lifetimes were associated with the presence of a very shallow boundary layer at the mountaintop so that the instrument inlets sampled from

the residual layer and NO_3 (and N_2O_5) mixing ratios and lifetimes were larger than those calculated from measured sources and sink terms.

Data availability

The PARADE data can be obtained on request (via John Crowley) from the owners.

The Supplement related to this article is available online at doi:10.5194/acp-16-4867-2016-supplement.

Acknowledgements. This work was carried out in part fulfilment of the PhD of NS at the Johannes Gutenberg University, Mainz. We thank the following: Simone Stöppler and Thomas Elsinger of the *Hessischer Rundfunk* for mounting the DOAS retroreflectors on the tower at the Großer Feldberg, Dupont for proving a sample of the FEP suspension used to coat the inlets and cavities, Pablo Hidalgo for generation of land-use maps derived from the CORINE land-cover database, the HLUG for use of meteorological measurements and Heinz Bingemer for logistical support throughout the planning and execution of the campaign.

The article processing charges for this open-access publication were covered by the Max Planck Society.

Edited by: W. Bloss

References

Allan, B. J., Carslaw, N., Coe, H., Burgess, R. A., and Plane, J. M. C.: Observations of the nitrate radical in the marine boundary layer, J. Atmos. Chem., 33, 129–154, 1999.

Ammann, M., Cox, R. A., Crowley, J. N., Jenkin, M. E., Mellouki, A., Rossi, M. J., Troe, J., and Wallington, T. J.: Evaluated kinetic and photochemical data for atmospheric chemistry: Volume VI – heterogeneous reactions with liquid substrates, Atmos. Chem. Phys., 13, 8045–8228, doi:10.5194/acp-13-8045-2013, 2013.

Ammann, M., Cox, R. A., Crowley, J. N., Jenkin, M. E., Mellouki, A., Rossi, M. J., Troe, J., and Wallington, T. J.: IUPAC: Task Group on Atmospheric Chemical Kinetic Data Evaluation, available at: http://iupac.pole-ether.fr/index.html, last access: February 2016.

Asaf, D., Pedersen, D., Matveev, V., Peleg, M., Kern, C., Zingler, J., Platt, U., and Luria, M.: Long-term measurements of NO_3 radical at a semiarid, urban Site: 1. Extreme concentration events and their oxidation capacity, Environ. Sci. Technol., 43, 9117–9123, doi:10.1021/es900798b, 2009.

Atkinson, R. and Arey, J.: Atmospheric degradation of volatile organic compounds, Chem. Rev., 103, 4605–4638, doi:10.1021/cr0206420, 2003.

Atkinson, R., Baulch, D. L., Cox, R. A., Crowley, J. N., Hampson, R. F., Hynes, R. G., Jenkin, M. E., Rossi, M. J., and Troe, J.: Evaluated kinetic and photochemical data for atmospheric chemistry: Volume I – gas phase reactions of O_x, HO_x, NO_x and SO_x species, Atmos. Chem. Phys., 4, 1461–1738, doi:10.5194/acp-4-1461-2004, 2004.

Atkinson, R., Baulch, D. L., Cox, R. A., Crowley, J. N., Hampson, R. F., Hynes, R. G., Jenkin, M. E., Rossi, M. J., Troe, J., and IUPAC Subcommittee: Evaluated kinetic and photochemical data for atmospheric chemistry: Volume II – gas phase reactions of organic species, Atmos. Chem. Phys., 6, 3625–4055, doi:10.5194/acp-6-3625-2006, 2006.

Behnke, W., George, C., Scheer, V., and Zetzsch, C.: Production and decay of $ClNO_2$ from the reaction of gaseous N_2O_5 with NaCl solution: Bulk and aerosol experiments, J. Geophys. Res., 102, 3795–3804, 1997.

Berkes, F., Hoor, P., Bozem, H., Kunkel, D., Sprenger, M., and Henne, S.: Airborne observation of mixing across the entrainment zone during PARADE 2011, Atmos. Chem. Phys. Discuss., 15, 29171–29212, doi:10.5194/acpd-15-29171-2015, 2015.

Bertram, T. H. and Thornton, J. A.: Toward a general parameterization of N_2O_5 reactivity on aqueous particles: the competing effects of particle liquid water, nitrate and chloride, Atmos. Chem. Phys., 9, 8351–8363, doi:10.5194/acp-9-8351-2009, 2009.

Bertram, T. H., Thornton, J. A., Riedel, T. P., Middlebrook, A. M., Bahreini, R., Bates, T. S., Quinn, P. K., and Coffman, D. J.: Direct observations of N_2O_5 reactivity on ambient aerosol particles, Geophys. Res. Lett., 36, L19803, doi:10.1029/2009GL040248, 2009.

Bonn, B., Bourtsoukidis, E., Sun, T. S., Bingemer, H., Rondo, L., Javed, U., Li, J., Axinte, R., Li, X., Brauers, T., Sonderfeld, H., Koppmann, R., Sogachev, A., Jacobi, S., and Spracklen, D. V.: The link between atmospheric radicals and newly formed particles at a spruce forest site in Germany, Atmos. Chem. Phys., 14, 10823–10843, doi:10.5194/acp-14-10823-2014, 2014.

Brown, S. S. and Stutz, J.: Nighttime radical observations and chemistry, Chem. Soc. Rev., 41, 6405–6447, 2012.

Brown, S. S., Stark, H., and Ravishankara, A. R.: Applicability of the steady state approximation to the interpretation of atmospheric observations of NO_3 and N_2O_5, J. Geophys. Res.-Atmos., 108, 4539, doi:10.1029/2003JD003407, 2003.

Brown, S. S., Dubé, W. P., Osthoff, H. D., Wolfe, D. E., Angevine, W. M., and Ravishankara, A. R.: High resolution vertical distributions of NO_3 and N_2O_5 through the nocturnal boundary layer, Atmos. Chem. Phys., 7, 139–149, doi:10.5194/acp-7-139-2007, 2007.

Brown, S. S., deGouw, J. A., Warneke, C., Ryerson, T. B., Dubé, W. P., Atlas, E., Weber, R. J., Peltier, R. E., Neuman, J. A., Roberts, J. M., Swanson, A., Flocke, F., McKeen, S. A., Brioude, J., Sommariva, R., Trainer, M., Fehsenfeld, F. C., and Ravishankara, A. R.: Nocturnal isoprene oxidation over the Northeast United States in summer and its impact on reactive nitrogen partitioning and secondary organic aerosol, Atmos. Chem. Phys., 9, 3027–3042, doi:10.5194/acp-9-3027-2009, 2009.

Brown, S. S., Dube, W. P., Peischl, J., Ryerson, T. B., Atlas, E., Warneke, C., de Gouw, J. A., Hekkert, S. t. L., Brock, C. A., Flocke, F., Trainer, M., Parrish, D. D., Feshenfeld, F. C., and Ravishankara, A. R.: Budgets for nocturnal VOC oxidation by nitrate radicals aloft during the 2006 Texas Air Quality Study, J. Geophys. Res.-Atmos., 116, D24305, doi:10.1029/2011jd016544, 2011.

Crowley, J. N., Schuster, G., Pouvesle, N., Parchatka, U., Fischer, H., Bonn, B., Bingemer, H., and Lelieveld, J.: Nocturnal nitrogen oxides at a rural mountain-site in south-western Germany, Atmos. Chem. Phys., 10, 2795–2812, doi:10.5194/acp-10-2795-2010, 2010.

Crowley, J. N., Thieser, J., Tang, M. J., Schuster, G., Bozem, H., Beygi, Z. H., Fischer, H., Diesch, J.-M., Drewnick, F., Borrmann, S., Song, W., Yassaa, N., Williams, J., Pöhler, D., Platt, U., and Lelieveld, J.: Variable lifetimes and loss mechanisms for NO_3 and N_2O_5 during the DOMINO campaign: contrasts between marine, urban and continental air, Atmos. Chem. Phys., 11, 10853–10870, doi:10.5194/acp-11-10853-2011, 2011.

Draxler, R. R. and Rolph, G. D.: HYSPLIT (HYbrid Single-Particle Lagrangian Integrated Trajectory) Model access via NOAA ARL READY Website, NOAA Air Resources Laboratory, Silver Spring, MD, USA, available at: http://ready.arl.noaa.gov/HYSPLIT.php (last access: January 2012), 2011.

Drewnick, F., Böttger, T., von der Weiden-Reinmüller, S.-L., Zorn, S. R., Klimach, T., Schneider, J., and Borrmann, S.: Design of a mobile aerosol research laboratory and data processing tools for effective stationary and mobile field measurements, Atmos. Meas. Tech., 5, 1443–1457, doi:10.5194/amt-5-1443-2012, 2012.

Fenske, J. D., Hasson, A. S., Ho, A. W., and Paulson, S. E.: Measurement of absolute unimolecular and bimolecular rate constants for CH_3CHOO generated by the trans-2-butene reaction with ozone in the gas phase, J. Phys. Chem. A, 104, 9921–9932, doi:10.1021/jp0016636, 2000.

Fry, J. L., Draper, D. C., Barsanti, K. C., Smith, J. N., Ortega, J., Winkle, P. M., Lawler, M. J., Brown, S. S., Edwards, P. M., Cohen, R. C., and Lee, L.: Secondary Organic Aerosol Formation and Organic Nitrate Yield from NO_3 Oxidation of Biogenic Hydrocarbons, Environ. Sci. Technol., 48, 11944–11953, doi:10.1021/es502204x, 2014.

Geyer, A., Alicke, B., Ackermann, R., Martinez, M., Harder, H., Brune, W., di Carlo, P., Williams, E., Jobson, T., Hall, S., Shetter, R., and Stutz, J.: Direct observations of daytime NO_3: Implications for urban boundary layer chemistry, J. Geophys. Res.-Atmos., 108, 3619–3631, doi:10.1016/S1352-2310(00)00549-5, 2003.

Hallquist, M., Wangberg, I., Ljungstrom, E., Barnes, I., and Becker, K. H.: Aerosol and product yields from NO_3 radical-initiated oxidation of selected monoterpenes, Environ. Sci. Technol., 33, 553–559, doi:10.1021/es980292s, 1999.

Handisides, G. M.: The influence of peroxy radicals on ozone production, Fachbereich Geowissenschaften, Johann Wolfgang Goethe Universität, Frankfurt am Main, Germany, 2001.

Heintz, F., Platt, U., Flentje, H., and Dubois, R.: Long-term observation of nitrate radicals at the tor station, Kap Arkona (Rugen), J. Geophys. Res.-Atmos., 101, 22891–22910, 1996.

Johnson, D. and Marston, G.: The gas-phase ozonolysis of unsaturated volatile organic compounds in the troposphere, Chem. Soc. Rev., 37, 699–716, doi:10.1039/b704260b, 2008.

Johnston, H. S., Davis, H. F., and Lee, Y. T.: NO_3 photolysis product channels: Quantum yields from observed energy thresholds, J. Phys. Chem., 100, 4713–4723, doi:10.1021/jp952692x, 1996.

Lelieveld, J., Butler, T. M., Crowley, J. N., Dillon, T. J., Fischer, H., Ganzeveld, L., Harder, H., Lawrence, M. G., Martinez, M., Taraborrelli, D., and Williams, J.: Atmospheric oxidation capacity sustained by a tropical forest, Nature, 452, 737–740, 2008.

Li, J., Reiffs, A., Parchatka, U., and Fischer, H.: In situ measurements of atmospheric CO and its correlation with NO_x and O_3 at a rural mountain site, Metrol. Meas. Syst., XXII, 25–38, 2015.

Mao, J., Ren, X., Zhang, L., Van Duin, D. M., Cohen, R. C., Park, J.-H., Goldstein, A. H., Paulot, F., Beaver, M. R., Crounse, J. D., Wennberg, P. O., DiGangi, J. P., Henry, S. B., Keutsch, F. N., Park, C., Schade, G. W., Wolfe, G. M., Thornton, J. A., and Brune, W. H.: Insights into hydroxyl measurements and atmospheric oxidation in a California forest, Atmos. Chem. Phys., 12, 8009–8020, doi:10.5194/acp-12-8009-2012, 2012.

Martinez, M., Perner, D., Hackenthal, E. M., Kulzer, S., and Schutz, L.: NO_3 at Helgoland during the NORDEX campaign in October 1996, J. Geophys. Res.-Atmos., 105, 22685–22695, 2000.

McLaren, R., Wojtal, P., Majonis, D., McCourt, J., Halla, J. D., and Brook, J.: NO_3 radical measurements in a polluted marine environment: links to ozone formation, Atmos. Chem. Phys., 10, 4187–4206, doi:10.5194/acp-10-4187-2010, 2010.

Mogensen, D., Gierens, R., Crowley, J. N., Keronen, P., Smolander, S., Sogachev, A., Nölscher, A. C., Zhou, L., Kulmala, M., Tang, M. J., Williams, J., and Boy, M.: Simulations of atmospheric OH, O_3 and NO_3 reactivities within and above the boreal forest, Atmos. Chem. Phys., 15, 3909–3932, doi:10.5194/acp-15-3909-2015, 2015.

Novelli, A., Hens, K., Tatum Ernest, C., Kubistin, D., Regelin, E., Elste, T., Plass-Dülmer, C., Martinez, M., Lelieveld, J., and Harder, H.: Characterisation of an inlet pre-injector laser-induced fluorescence instrument for the measurement of atmospheric hydroxyl radicals, Atmos. Meas. Tech., 7, 3413–3430, doi:10.5194/amt-7-3413-2014, 2014.

Noxon, J. F., Norton, R. B., and Marovich, E.: NO_3 in the Troposphere, Geophys. Res. Lett., 7, 125–128, 1980.

Orphal, J., Fellows, C. E., and Flaud, P. M.: The visible absorption spectrum of NO_3 measured by high-resolution Fourier transform spectroscopy, J. Geophys. Res.-Atmos., 108, 4077, doi:10.1029/2002JD002489, 2003.

Osthoff, H. D., Pilling, M. J., Ravishankara, A. R., and Brown, S. S.: Temperature dependence of the NO_3 absorption cross-section above 298 K and determination of the equilibrium constant for $NO_3 + NO_2 \leftrightarrow N_2O_5$ at atmospherically relevant conditions, Phys. Chem. Chem. Phys., 9, 5785–5793, 2007.

Osthoff, H. D., Roberts, J. M., Ravishankara, A. R., Williams, E. J., Lerner, B. M., Sommariva, R., Bates, T. S., Coffman, D., Quinn, P. K., Dibb, J. E., Stark, H., Burkholder, J. B., Talukdar, R. K., Meagher, J., Fehsenfeld, F. C., and Brown, S. S.: High levels of nitryl chloride in the polluted subtropical marine boundary layer, Nat. Geosci., 1, 324–328, 2008.

Ouyang, B., McLeod, M. W., Jones, R. L., and Bloss, W. J.: NO_3 radical production from the reaction between the Criegee intermediate CH_2OO and NO_2, Phys. Chem. Chem. Phys., 15, 17070–17075, doi:10.1039/c3cp53024h, 2013.

Phillips, G. J., Tang, M. J., Thieser, J., Brickwedde, B., Schuster, G., Bohn, B., Lelieveld, J., and Crowley, J. N.: Significant concentrations of nitryl chloride observed in rural continental Europe associated with the influence of sea salt chloride and anthropogenic emissions, Geophys. Res. Lett., 39, L10811, doi:10.1029/2012GL051912, 2012.

Platt, U., Perner, D., Winer, A. M., Harris, G. W., and Pitts, J. N. J.: Detection of NO_3 in the polluted troposphere by differential optical absorption, Geophys. Res. Lett., 7, 89–92, 1980.

Presto, A. A. and Donahue, N. M.: Ozonolysis fragment quenching by nitrate formation: The pressure dependence of prompt OH radical formation, J. Phys. Chem. A, 108, 9096–9104, doi:10.1021/jp047162s, 2004.

Riemer, N., Vogel, H., Vogel, B., Anttila, T., Kiendler-Scharr, A., and Mentel, T. F.: Relative importance of organic coatings for the heterogeneous hydrolysis of N_2O_5 during summer in Europe, J. Geophys. Res.-Atmos., 114, D17307, doi:10.1029/2008JD011369, 2009.

Rinne, J., Markkanen, T., Ruuskanen, T. M., Petäjä, T., Keronen, P., Tang, M. J., Crowley, J. N., Rannik, Ü., and Vesala, T.: Effect of chemical degradation on fluxes of reactive compounds – a study with a stochastic Lagrangian transport model, Atmos. Chem. Phys., 12, 4843–4854, doi:10.5194/acp-12-4843-2012, 2012.

Sarwar, G., Simon, H., Bhave, P., and Yarwood, G.: Examining the impact of heterogeneous nitryl chloride production on air quality across the United States, Atmos. Chem. Phys., 12, 6455–6473, doi:10.5194/acp-12-6455-2012, 2012.

Schuster, G., Labazan, I., and Crowley, J. N.: A cavity ring down/cavity enhanced absorption device for measurement of ambient NO_3 and N_2O_5, Atmos. Meas. Tech., 2, 1–13, doi:10.5194/amt-2-1-2009, 2009.

Stone, D., Blitz, M., Daubney, L., Howes, N. U. M., and Seakins, P.: Kinetics of CH_2OO reactions with SO_2, NO_2, NO, H_2O and CH_3CHO as a function of pressure, Phys. Chem. Chem. Phys., 16, 1139–1149, doi:10.1039/c3cp54391a, 2014.

Stutz, J., Alicke, B., Ackermann, R., Geyer, A., White, A., and Williams, E.: Vertical profiles of NO_3, N_2O_5, O_3, and NO_x in the nocturnal boundary layer: 1. Observations during the Texas Air Quality Study 2000, J. Geophys. Res.-Atmos., 109, D12306, doi:10.1029/2003JD004209, 2004.

Stutz, J., Wong, K. W., Lawrence, L., Ziemba, L., Flynn, J. H., Rappenglueck, B., and Lefer, B.: Nocturnal NO_3 radical chemistry in Houston, TX, Atmos. Env., 44, 4099–4106, doi:10.1016/j.atmosenv.2009.03.004, 2010.

Taipale, R., Sarnela, N., Rissanen, M., Junninen, H., Rantala, P., Korhonen, F., Siivola, E., Berndt, T., Kulmala, M., Mauldin, R. L., Petaja, T., and Sipila, M.: New instrument for measuring atmospheric concentrations of non-OH oxidants of SO_2, Boreal Environ. Res., 19, 55–70, 2014.

Taraborrelli, D., Lawrence, M. G., Crowley, J. N., Dillon, T. J., Gromov, S., Groß, C. B. M., Vereecken, L., and Lelieveld, J.: Hydroxyl radical buffered by isoprene oxidation over tropical forests, Nat. Geosci., 5, 190–193, 2012.

Thieser, J., Schuster, G., Schuladen, J., Phillips, G. J., Reiffs, A., Parchatka, U., Pöhler, D., Lelieveld, J., and Crowley, J. N.: A two-channel thermal dissociation cavity ring-down spectrometer for the detection of ambient NO_2, RO_2NO_2 and $RONO_2$, Atmos. Meas. Tech., 9, 553–576, doi:10.5194/amt-9-553-2016, 2016.

Thornton, J. A., Kercher, J. P., Riedel, T. P., Wagner, N. L., Cozic, J., Holloway, J. S., Dube, W. P., Wolfe, G. M., Quinn, P. K., Middlebrook, A. M., Alexander, B., and Brown, S. S.: A large atomic chlorine source inferred from mid-continental reactive nitrogen chemistry, Nature, 464, 271–274, doi:10.1038/nature08905, 2010.

Vereecken, L., Harder, H., and Novelli, A.: The reaction of Criegee intermediates with NO, RO_2, and SO_2, and their fate in the atmosphere, Phys. Chem. Chem. Phys., 14, 14682–14695, doi:10.1039/c2cp42300f, 2012.

Voigt, S., Orphal, J., and Burrows, J. P.: The temperature and pressure dependence of the absorption cross-sections of NO_2 in the 250–800 nm region measured by Fourier-transform spectroscopy, J. Photoch. Photobiol. A, 149, 1–7, doi:10.1016/s1010-6030(01)00650-5, 2002.

von Friedeburg, C., Wagner, T., Geyer, A., Kaiser, N., Vogel, B., Vogel, H., and Platt, U.: Derivation of tropospheric NO_3 profiles using off-axis differential optical absorption spectroscopy measurements during sunrise and comparison with simulations, J. Geophys. Res.-Atmos., 107, 4168, doi:10.1029/2001JD000481, 2002.

Wayne, R. P., Barnes, I., Biggs, P., Burrows, J. P., Canosa-Mas, C. E., Hjorth, J., Le Bras, G., Moortgat, G. K., Perner, D., Poulet, G., Restelli, G., and Sidebottom, H.: The nitrate radical: Physics, chemistry, and the atmosphere, Atmos. Environ. A-Gen, 25A, 1–206, 1991.

Welz, O., Savee, J. D., Osborn, D. L., Vasu, S. S., Percival, C. J., Shallcross, D. E., and Taatjes, C. A.: Direct kinetic measurements of Criegee intermediate (CH_2OO) formed by reaction of CH_2I with O_2, Science, 335, 204–207, doi:10.1126/science.1213229, 2012.

Appendix B2

Chemical and meteorological influences on the lifetime of NO3 at a semi-rural mountain site during PARADE

N. Sobanski[1], M. J. Tang[1,a], J. Thieser[1], G. Schuster[1], D. Pöhler[2], H. Fischer[1], W. Song[1], C. Sauvage[1], J. Williams[1], J. Fachinger[3], F. Berkes[4,b], P. Hoor[4], U. Platt[2], J. Lelieveld[1], and J. N. Crowley[1]

[1]Division of Atmospheric Chemistry, Max-Planck-Institut für Chemie, Mainz, Germany
[2]Institute of Environmental Physics, University of Heidelberg, Heidelberg, Germany
[3]Division of Particle Chemistry, Max-Planck-Institut für Chemie, Mainz, Germany
[4]Institute for Atmospheric Physics, Johannes Gutenberg University Mainz, Mainz, Germany
[a]present address: Chemistry Department, University of Iowa, Iowa City, USA
[b]present address: Institute of Energy and Climate, Forschungszentrum Jülich, Jülich, Germany

Supplementary information

Supplement of Atmos. Chem. Phys., 16, 4867–4883, 2016
http://www.atmos-chem-phys.net/16/4867/2016/
doi:10.5194/acp-16-4867-2016-supplement
© Author(s) 2016. CC Attribution 3.0 License.

Atmospheric Chemistry and Physics
Open Access
EGU

Supplement of

Chemical and meteorological influences on the lifetime of NO_3 at a semi-rural mountain site during PARADE

N. Sobanski et al.

Correspondence to: J. N. Crowley (john.crowley@mpic.de)

The copyright of individual parts of the supplement might differ from the CC-BY 3.0 licence.

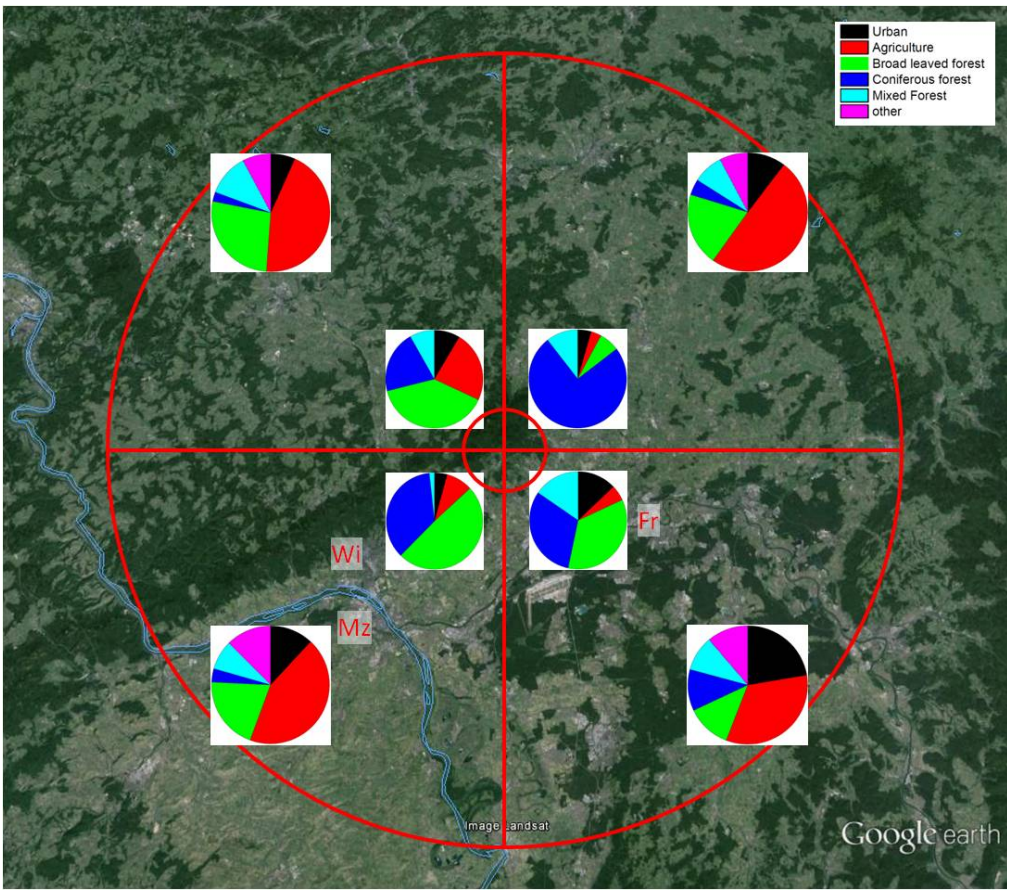

Fig. S1. Land-use in the area surrounding the PARADE campaign measurement site. The inner circle has a radius of 5 km, the outer circle a radius of 50 km. Both areas are divided into four sectors (North-East, South-East, South-West and North-West). For each of the 8 sectors the land-use is given by a pie chart. The Fr, Wi and Mz symbols represent the approximate location of the cities Frankfurt, Wiesbaden and Mainz, respectively. The map was generated from the CORINE Land Cover database by Dr. Pablo J. Hidalgo.

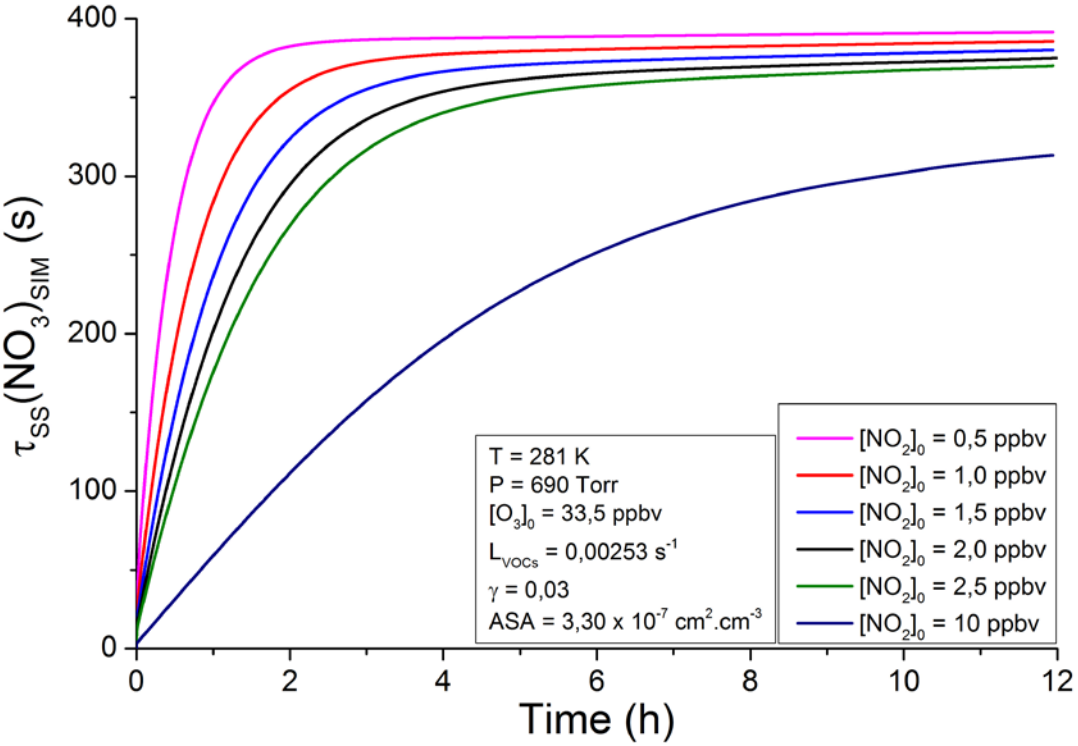

Fig. S2. Simulated evolution of the steady state lifetime of NO_3 assuming reaction of NO_2 with O_3 as the only NO_3 source, and both a homogeneous and a heterogeneous loss process. The simulation assumes variable $[O_3]$ and $[NO_2]$ as would be the case for a point source and a constant NO_3 reactivity in the gaseous phase (0.00253 s^{-1}, due e.g. to VOCs). The different curves each correspond to a different initial NO_2 mixing ratio (with a fixed initial $[O_3]$ for each simulation). The NO_3 losses through N_2O_5 uptake on aerosols is simulated by keeping the aerosol surface area (ASA) and the uptake coefficient γ constant at the values listed in the figure. The overall heterogeneous sink, depending on $[NO_2]$, is thus different for each simulation, which explains the slightly different effective lifetime ($\tau_{ss}(NO_3)$ for $t \rightarrow \infty$). At short times, the true steady state lifetime (350 to 380 s) is underestimated.

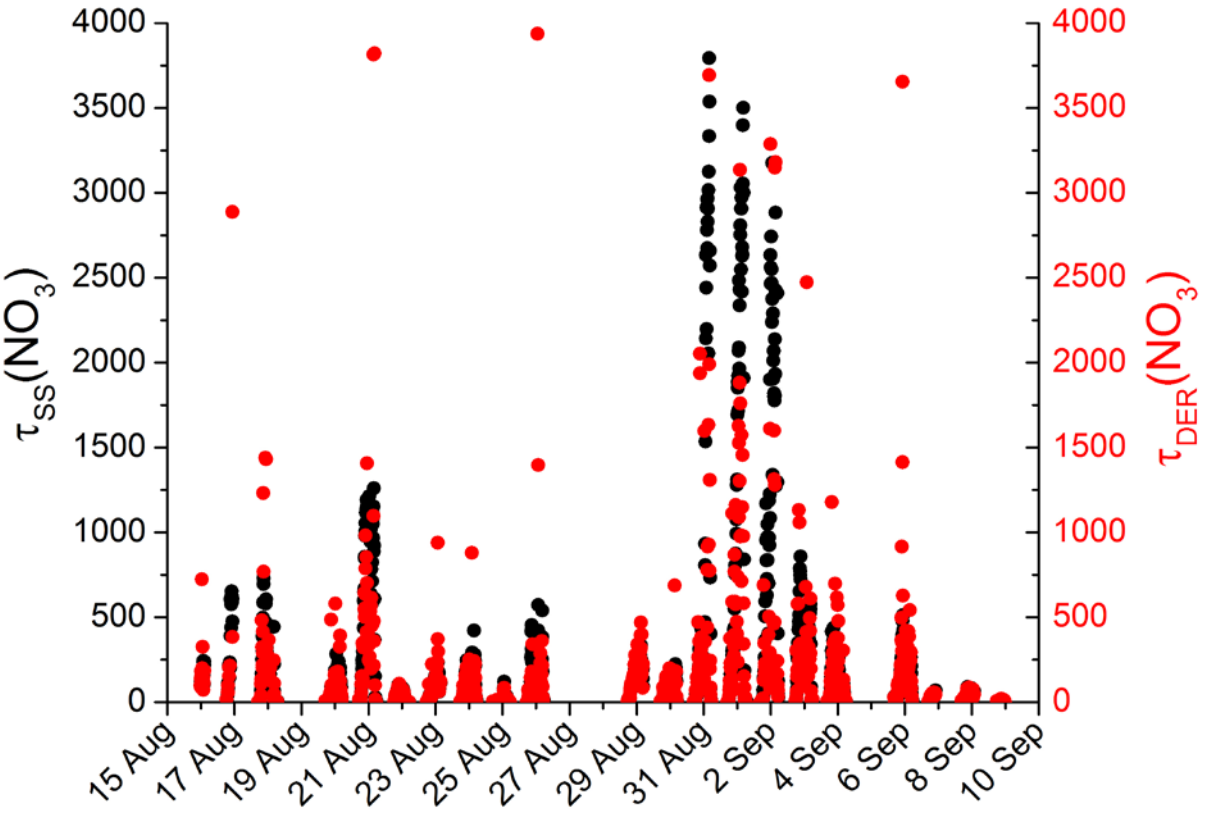

Fig. S3. Comparison between $\tau_{ss}(NO_3)$ and $\tau_{DER}(NO_3)$ using the same $[NO_3]$, $[NO_2]$ and $[O_3]$ datasets. For most of the nights both datasets agree even though outliers for $\tau_{DER}(NO_3)$ are sometimes calculated due to noise in the raw data.

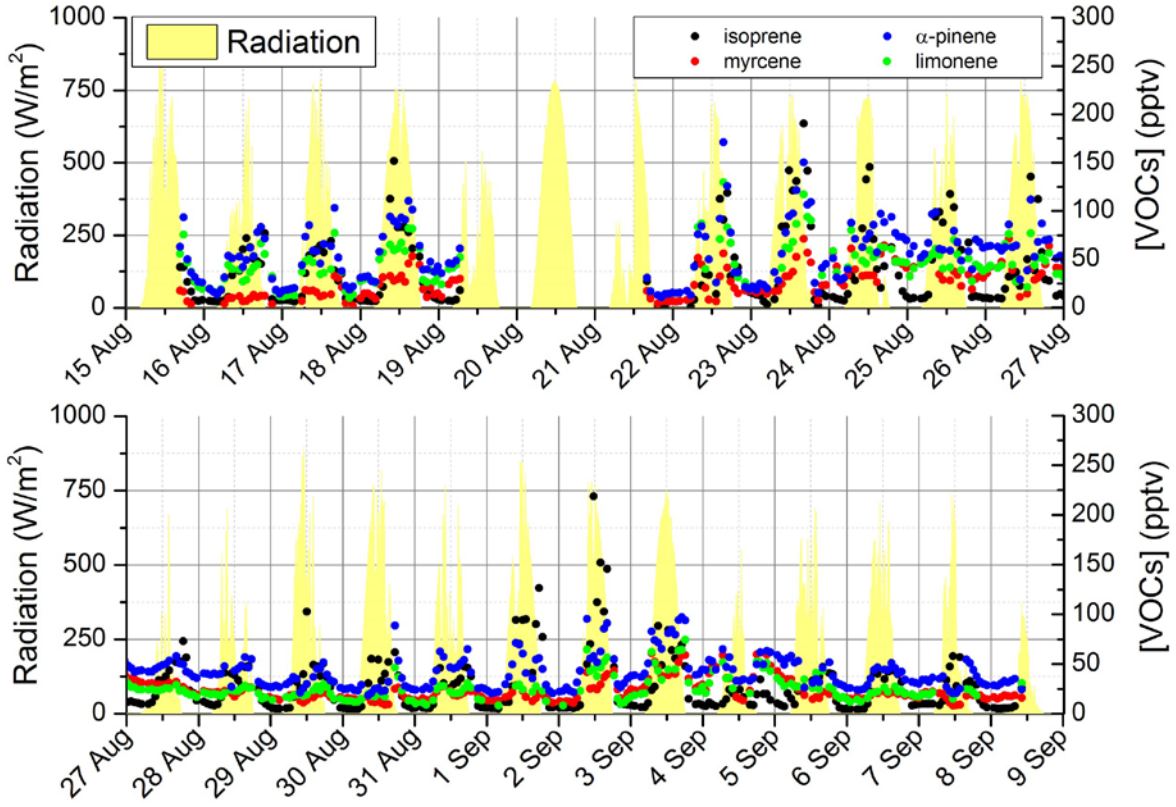

Fig. S4. Time series of the mixing ratios of the reactive (highlighted) VOCs in Table 2.

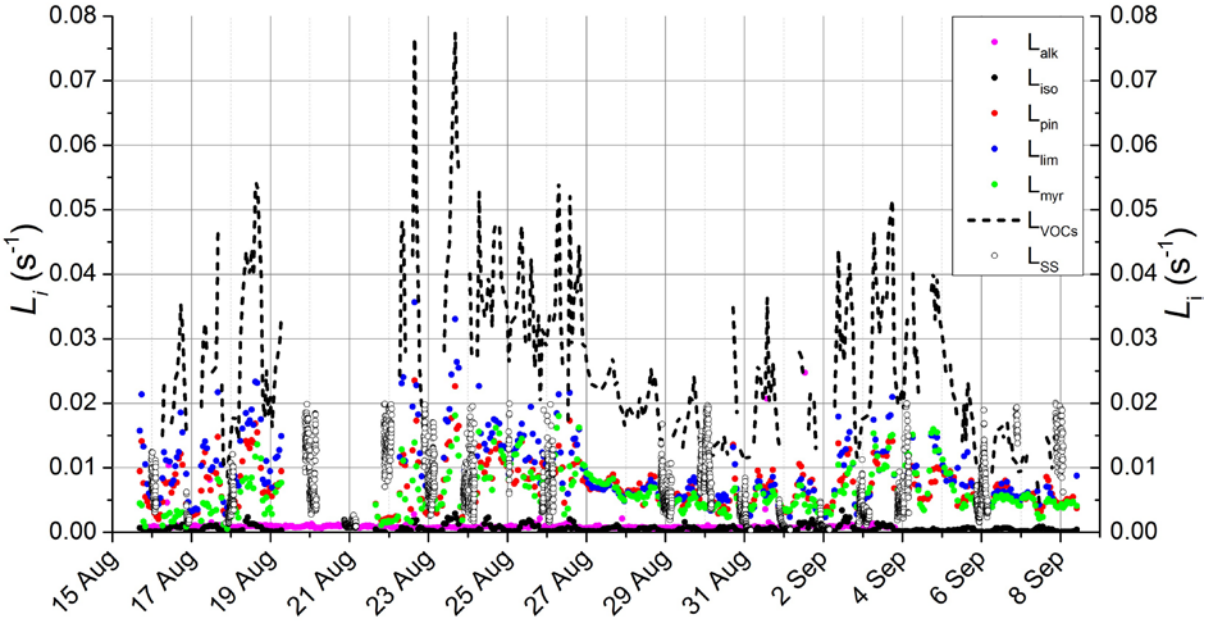

Fig. S5. Individual and summed reactivities (towards NO_3) of the VOCs listed in Table 2. L_{iso}, L_{pin}, L_{lim} and L_{myr} represent respectively the losses due to isoprene, α-pinene, limonene and myrcene. All the alkenes and alkanes reactivities are summed in the L_{alk} term. The L_{VOCs} term sums up the individual terms (L_{iso}, L_{pin}, L_{lim}, L_{myr} and L_{alk}). The steady-state loss rate constant for NO_3 (L_{ss}) is also plotted.

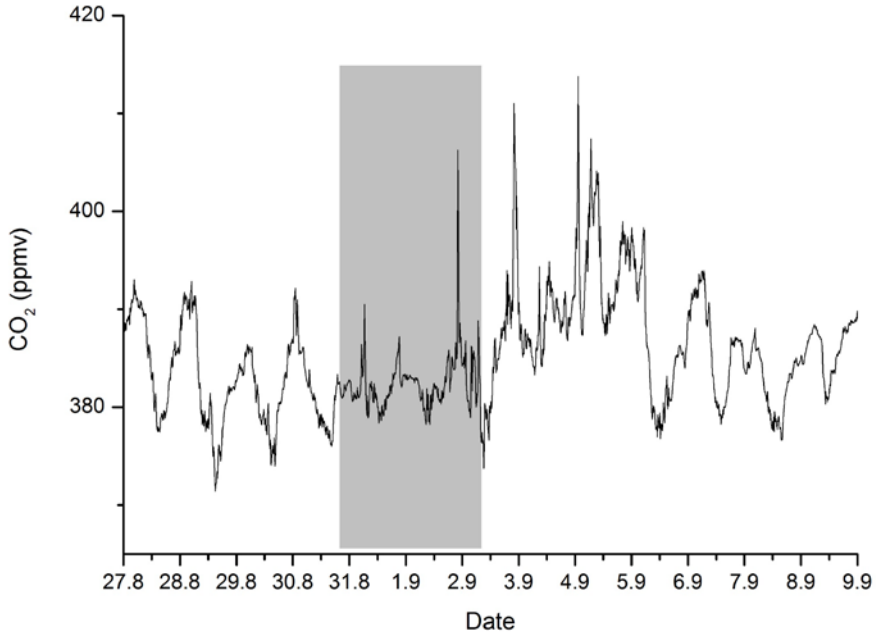

Fig. S6. CO_2 during PARADE. The grey shaded area indicates no significant nocturnal build-up of CO_2 (contrast e.g. the nights of 27.8 - 30.8 or 6.9 - 9.9) and is coincident with NO_3 lifetimes exceeding 2000 s.

Appendix C

Day- and night-time formation of organic nitrates at a forested mountain-site in south-west Germany

N. Sobanski[1], J. Thieser[1], J. Schuladen[1], C. Sauvage[1], W. Song[1], J. Williams[1], J. Lelieveld[1] and J.N. Crowley[1]

[1] Max-Planck-Institut für Chemie, Division of Atmospheric Chemistry, Mainz, Germany.

Submitted to Atmo. Chem. Phys. Discuss.
(30.09.2016)

Day- and Night-time Formation of Organic Nitrates at a Forested Mountain-site in South West Germany

N. Sobanski[1], J. Thieser[1], J. Schuladen[1], C. Sauvage[1], W. Song[1], J. Williams[1], J. Lelieveld[1] and J.N. Crowley[1]

[1] Max-Planck-Institut für Chemie, Division of Atmospheric Chemistry, Mainz, Germany.

Correspondence to: J. N. Crowley (john.crowley@mpic.de)

Abstract. We report in-situ measurement of total peroxy-nitrates (ΣPNs) and total alkyl nitrates (ΣANs) in a forested / urban location at the top of the Kleiner Feldberg mountain in South-West Germany. The data, obtained using Thermal Dissociation Cavity Ring Down Spectroscopy (TD-CRDS) in August-September 2011 (PARADE campaign) and July-August 2015 (NOTOMO campaign), represent the first detailed study of ΣPNs and ΣANs over continental Europe. We find that a significant fraction of NO*x* (up to 75 %) is sequestered as organics nitrates at this site. Futher, we also show that the night-time production of alkyl nitrates by reaction of NO_3 with biogenic hydrocarbons is comparable to that from day-time, OH-initiated oxidation pathways. The ΣANs-to-ozone ratio obtained during PARADE was used to derive an approximate, average yield of organic nitrates at noon time from the OH initiated oxidation of VOCs of 7 % at this site in 2011, which is comparable with that obtained from an analysis of VOCs at the site. A much lower yield, < 2 %, was observed in 2015, which may reflect a reduction in the fraction of biogenic hydrocarbons contributing to OH reactivity in that year.

1 Introduction

The gas- and aerosol-phase chemistry of the continental, tropospheric boundary layer is strongly influenced by reactive nitrogen oxides. The primary pollutants NO and NO_2 (constituting the NO*x* family) are mostly emitted by anthropogenic activity involving high temperature combustion or from microbial activity in soils and have a strong impact on tropospheric O_3 levels. Knowing the fate of NO*x* is paramount to prediction of O_3 production rates and oxidation capacity on regional and global scales (Lelieveld et al., 2016). Following emission, NO undergoes a series of reaction steps that ultimately lead either to the formation of short lived trace gases that can act as sinks for NO*x* (HNO_3) or to the formation of longer lived, reservoir species that can be transported over long disances and act as a source of NO*x* ($RONO_2$ and $RC(O)OONO_2$) in locations that are remote from anthropogenic emissions. In the troposphere, a significant amount of NO*x* can be temporarily sequestered as HNO_3 and organic nitrates. The former is produced predominantly by the oxidation of NO_2 by OH whereas organic nitrates are produced by the oxidation of both NO and NO_2 by organic peroxy radicals during the day (R3 and R4) or in the oxidation

of alkenes by NO_3 during the night (R6) (see below). Organic peroxy radicals are formed in the oxidation of hydrocarbons by OH (R1 and R2) (Atkinson, 2000; Atkinson and Arey, 2003a, b).

The products of NO*x* oxidation by organic radicals are peroxy nitrates (RO_2NO_2, abbreviated as PNs, R3) and alkyl nitrates ($RONO_2$ abbreviated called ANs, R4). Based on thermal lifetimes, PNs may be divided divided in two families, those with a carbonyl group adjacent to the peroxy entity (i.e. $RC(O)O_2NO_2$) and those without. The former are peroxyacyl nitric anhydrides, generally referered to as peroxyacyl nitrates or PANs, and have lifetimes with respect to thermal dissociation on the order of hours in the midlatitude boundary layer. Non-acyl PNs (RO_2NO_2) such as $CH_3O_2NO_2$ and HO_2NO_2 thermally decompose on timescales of seconds to minutes at temperatures close to 298 K and are thus only encountered in significant concentrations in cold regions of the atmosphere (Murphy et al., 2004; Browne et al., 2011; Nault et al., 2015). Alkyl nitrates are formed with variable branching ratio in a minor channel (R4) of the reaction between organic peroxy radicals and NO, the greater fraction of this reaction leading to formation of an alkoxy radical and NO_2 (R5) and thus (via NO_2 photolysis) ultimately to O_3. Alkyl nitrates are also formed at night during the NO_3 induced oxidation of unsaturated hydrocarbons, the first reaction step being addition of NO_3 to a double bond followed by formation of a nitrooxy alkylperoxy radical (R6), the fate of which includes reaction with HO_2, other peroxy radicals, NO_3, NO_2 or, if available, NO so that the final products are, hydroxy-, hydroxide- and carbonyl- substituted nitrates as well as dinitrates (Schwantes et al., 2015; IUPAC, 2016). The nitrate yields (per VOC reacted) can be high, especially for biogenic VOCs including the terpenoids, and can exceed 50 % (Ng et al., 2016).

Organic nitrates have highly variable lifetimes (from seconds to days) that are mainly controlled by rates of thermal decomposition and thus temperature for PNs. For ANs, OH oxidation, photolysis and deposition or scavenging by aerosol particles all play a role (Roberts, 1990; Browne et al., 2013; Rollins et al., 2013).

$OH + RH (+ O_2)$	$\rightarrow$	$RO_2 + H_2O$	(R1)
$R{=}R' + OH (+ O_2)$	$\rightarrow$	$R(OH)R'O_2$	(R2)
$RO_2 + NO_2 + M$	$\rightarrow$	$RO_2NO_2 + M$	(R3)
$RO_2 + NO + M$	$\rightarrow$	$RONO_2 + M$	(R4)
$RO_2 + NO$	$\rightarrow$	$RO + NO_2$	(R5)
$R{=}R' + NO_3 (+ O_2)$	$\rightarrow$	$R(ONO_2)R'O_2$	(R6)
$R(ONO_2)R'O_2 (+ROx, NOx)$	$\rightarrow$	ANs	(R7)

The first field measurements of organic nitrates were made using low time resolution methods (gas chromatography) (Roberts et al., 1989; Blanchard et al., 1993) and focused mostly on PAN (peroxy acetyl nitrate), PPN (peroxy propyl nitrate) and MPAN (methacryloyl peroxynitrate) (Williams et al., 1997; Williams et al., 2000) which are the most common peroxy nitrates in the continental boundary layer, and individual mono- and polyfunctional alkyl nitrates from alkane or alkene

precursors (Atlas, 1988; Flocke et al., 1991). More recently, mass spectrometry based methods have been developed to measure a wider range of organic nitrates at high time resolution (Beaver et al., 2012). Early attempts to compare speciated NO_y and total NO_y measurements (Fahey et al., 1986; Buhr et al., 1990; Ridley et al., 1990) revealed a substantial missing fraction of reactive nitrogen which was addresssed by the first measurements of ΣPNs and ΣANs by thermal dissociation coupled with laser induced fluorescence detection of NO_2 (Day et al., 2003). Those and subsequent measurements (Wooldridge et al., 2010; Perring et al., 2013) indicated that, depending on environment, the interaction between NO*x* and VOCs leads to a wide variety of compounds with different level of structural functionality and atmospheric lifetime which can have a variable and significant influence on the lifetime of NO*x* and also aerosol particles composition (Browne et al., 2013; Ayres et al., 2015).

We present here an analysis of organic nitrates and NO_2 measured using TD-CRDS during two field campaigns that took place at a forested, semi-rural mountain site in South-Western Germany. As far as we are aware, this work constitutes the first measurement and analysis of ΣPNs and ΣANs over continental Europe. We show that the daily variations of ΣANs and ΣPNs are both controlled by photo-chemical oxidation of VOCs, night-time production by NO_3 induced oxidation of biogenic VOCs and local meteorology. We also report an estimation of the effective branching ratios of AN formation in R4 and R5 using O_3 measurements and compare this with an estimation based on VOCs at the site and known, individual branching ratios.

2 Campaign site and meteorology

The PARADE (PArticles and RAdicals: Diel observations of the impact of urban and biogenic Emissions) and NOTOMO (NOcturnal chemistry at the Taunus Observatory: insights into Mechanisms of Oxidation) campaigns took place during August-September 2011 and July-August 2015 at the Taunus Observatory (50.22 N, 8.45 E) on top of the "Kleiner Feldberg" mountain, 850 m above sea-level and 500 m above nearby urban centres in the states of Hessen and Rheinland-Pfalz in South-Western Germany. This site has been described extensively in different publications (Crowley et al., 2010; Sobanski et al., 2016b) and only a short description is given here. A few km to the NNE and SE of the station are two mountains of similar height ("Großer Feldberg" 878 m and "Altkoenig" 798 m ASL). The nearby (10s of km) environment in the complete northern sector is a partially forested, rural region. The SW-SE sector is a more densely populated, industrialized region which includes the Frankfurt-Mainz-Wiesbaden urban agglomeration. Frankfurt is situated ≈ 20 km to the SE and Mainz and Wiesbaden ≈ 20 – 30 km to the SW. A detailed land-use analysis of the surrounding area was given by Sobanski et al. (2016b).

Reactive trace-gas measurements at the site are strongly influenced by the horizontal advection of different types of air masses, both on a local scale (forest/rural vs. urban) and on regional scales (continental vs. marine). On some nights during PARADE, the instruments sampled air from a low lying residual layer which resulted in very high NO_3 steady state lifetimes (≈ 1h) (Sobanski et al., 2016b). During both campaigns, the meteorological conditions were very variable and associated

with different air mass origins. The PARADE campaign can be divided in three periods (Phillips et al., 2012). The first period from the 15th to the 26th of August was influenced by air masses of continental origin and was associated with high temperature, and low humidity. A cold front arriving from the West resulted in two consecutive days of rain/fog conditions and a large decrease in temperature and ozone. The period 26th to 5th of September was influenced by advection from the Atlantic / UK region and during this period the temperature increased progressively together with ozone. A second cold front on the 5th of September again resulted in a fast temperature decrease followed by a period of low photochemical activity. The NOTOMO campaign was characterised by frequent fluctuation between cold/wet and warm/dry periods. Back trajectory calculations (48 hrs) showed that the warm/dry periods were generally associated with air masses of continental origin, the cold/wet periods with air masses coming from the West with Atlantic influence. In both campaigns, the highly variable photochemical activity and temperature strongly influenced the mixing ratios of both O_3 and organic nitrates, which is why this site was selected.

3 Instrumentation

The instruments deployed during both field campaigns have been described in Schuster et al. (2009) and Thieser et al. (2016) for PARADE and in Sobanski et al. (2016a) for NOTOMO. During the PARADE campaign, all instruments used collocated inlets of PFA piping. During the NOTOMO campaign, the instruments described here sampled from a common, high volume-flow inlet. Temperature, ozone, wind speed and wind direction data were measured by the permanent instrumentation of the state-run air pollution surveillance network (HLUG) at this site.

3.1 NO_2, NO_3, ΣPNs and ΣANs

PARADE: NO_2 and total organic nitrates were measured during both campaigns by Thermal Dissociation Cavity Ring-Down Spectroscopy (TD-CRDS). During PARADE, a two cavity TD-CRDS instrument was deployed (Thieser et al., 2016). The instrument was located in a container and sampled air from a 5 m ½" PFA tube acting as a bypass flow through which ambient air was drawn at ≈ 40 dm^3 (STP) min^{-1}, (hereafter SLM). The Teflon coated (DuPont, FEP, TE 9568) cavities were operated at 405 and 409 nm, and both were maintained at 35 °C to improve thermal stability. One cavity sampled air from the bypass flow at ambient temperature to measure NO_2 mixing ratios, the second channel sampled alternately through two heated inlets, one held at 200 °C and the other at 450 °C to thermally dissociate PNs and ANs respectively into NO_2. When sampling through the 200 ° C inlet, this channel measures the sum of ambient NO_2 + ΣPNs. Sampling via the 450 °C inlet results in detection of NO_2 + ΣPNs + ANs. Mixing ratios of ΣPNs and ΣANs were obtained by the difference in NO_2 measured in the two cavities and applying corrections to account for conversion (to NO_2) of $ClNO_2$ (measured by CIMS, Phillips et al. (2012)) and N_2O_5 (TD-CRDS, Sobanski et al. (2016b)) in the hot inlets and also for biases related to reactions involving peroxy radicals, NO, NO_2, and O_3 as outlined in detail in Thieser et al. (2016).

During PARADE, NO_3 was measured by the 662 nm, two channel TD-CRDS described in Schuster et al. (2009). One cavity sampled air at ambient temperature and measured NO_3, the second one measured the sum of NO_3 and N_2O_5 following the

thermal dissociation of N_2O_5 to NO_3 and NO_2 at 100 °C. This instrument was located on the roof top and sampled air from the centre of a bypass flow (50 SLM) through a 1 m long, ½-inch (12.7 mm) diameter PFA pipe. The detection limit for NO_3 and NO_2 were 2 and 30 pptv and the uncertainties 15 and 6 % respectively. As described in Thieser et al. (2016), the uncertainty associated with the NO_2 measurement is 6 % + 20pptv × RH/100 (where RH is the relative humidity in %). The detection limit and uncertainties for the organic nitrate meaurements depends on NO*x* levels and the reader is referred to Thieser et al. (2016) for more details.

NOTOMO: The 5 channel, TD-CRDS deployed during the NOTOMO campaign was recently decribed in detail by Sobanski et al. (2016a). This instrument has five identical cavities sampling from separate inlet lines. Two cavities operate at 662 nm for the detection of NO_3, the other three at 405 nm to detect NO_2. One 662 nm cavity samples 8 SLM from an inlet at ambient temperature to measure NO_3, the other draws 7 SLM through an inlet at 110 °C to measure the sum of NO_3 + N_2O_5 following thermal dissociation of N_2O_5 to NO_3. Of the three 405 nm cavities, one draws 2.5 SLM via an inlet at ambient temperature to measure NO_2, the other two each sample 2.5 SLM from inlets heated to 175 °C and 375 °C to measure NO_2 + ΣPNs and NO_2 + ΣPNs + ΣANs, respectively. The ¼ inch (6.35 mm) inlet line for the 662 nm cavities was attached ia a T-piece to a 60 cm long ½ inch PFA pipe sampling air at 100 L min^{-1} from the center of a large diameter (15 cm), high-flow inlet (10 m^3 min^{-1}), with its opening located 8 m above the ground and 3m above the top of the container. The 405 nm channels sampled air via a 1 m long, ¼ inch PFA tube protruding into the center of the high-flow inlet. Correction for $ClNO_2$ and N_2O_5 conversion to NO_2 were carried out as described for the PARADE campaign, the removal of the biases related to reactions by peroxy radicals, O_3 and NO*x* were carried out as described in Sobanski et al. (2016a). The detection limits were 1.5 and and 60 pptv for NO_3 and NO_2, respectively, with uncertainties of 25 % for NO_3 and 6.5 % for NO_2 (Sobanski et al., 2016a).

3.2 NO during PARADE / NOTOMO

During PARADE, NO measurements were made with a modified commercial chemiluminescence detector (CLD 790 SR), the operation of which during this campaign is described by Li et al. (2015). The detection limit for this instrument is 4 pptv in 2 s with a total uncertainty of 4 %. This instrument did not participate in NOTOMO and daytime NO mixing ratios were calculated from measurements of NO_2, O_3 and $J(NO_2)$ assuming photo stationary state:

$$[NO]_{calc} = J(NO_2)\,[NO_2] / k_{(NO+O3)}[O_3] \quad (1)$$

where $J(NO_2)$ is the photolysis frequency of NO_2 and $k_{(NO+O3)}$ is the rate constant for reaction of NO with O_3. This expression ignores the oxidation of NO to NO_2 via e.g. reactions of peroxy radicals and thus overestimates NO. However, this method of estimating [NO] resulted in satisfactory agreement (within ≈ 20 %) with measurements from the HLUG for periods when NO was above the detection limit (> 1ppb) of their instrument. Night-time concentrations of NO during NOTOMO were

assumed to be zero, as has been shown to be the case on many nights during previous campaigns at this site (Crowley et al., 2010; Sobanski et al., 2016b).

3.3 VOCs measurements during PARADE

VOCs were measured using two gas-chromatographic instruments with a mass spectrometer (GC-MS) and a flame ionisation detector (GC-FID). The GC-MS measured biogenic and aromatic hydrocarbons with online adsorption/thermal desorption (Markes International) connected to a gas chromatograph (Agilent GC 6890A) and a mass selective detector (Agilent MSD 5973 inert). The time resolution was ≈1 h (35 min sampling time), and detection limits were around 1 pptv with an uncertainty of 10–15 %. The GC-FID measured non-methane hydrocarbons (NMHC) using two coupled gas chromatographs (GC 5000 VOC and GC 5000 BTX; AMA instruments, Ulm, Germany) GC 5000 VOC was used for measurement of C2–C6 NMHCs and BTX for C6–C12. The detection limits range from 1 to 5 pptv, exceptions being ethane, ethene, propene, benzene and toluene with values of 8, 16, 9, 14 and 48 pptv respectively. The GC-FID was calibrated using a multi-gas mixture (National Physical Laboratory). The total uncertainty is close to 10% for most trace gases with the exception of 1-pentane (15 %). The time resolution of the measurement is 60 min and the mixing ratio represents an average over a sampling period of 20 min. The VOCs measured during PARADE are listed in Table 1 along with their rate constants for reaction with OH and also the associated alkyl nitrate yields and production rates, P(ANs) and P(O_3), for ANs and PNs, respectively (see Sect. 4.4).

4 Results and discussion

4. 1 NO*x* and organic nitrates at the Taunus Observatory

The temperature, humidity, wind direction, O_3, NO, NO_2, ΣPNs and ΣANs for the PARADE and NOTOMO campaigns are shown in Fig. 1 and Fig. 2., respectively. The reactive nitrogen species are plotted at 10 min resolution, and Table 2 summarizses selected minimum, maximum and mean values for the two datasets. The data provided by the HLUG (relative humidity, wind and O_3) are given at 30 min intervals.

During PARADE and NOTOMO, NO_2 varied between ≈ 1 to 15 ppbv with the highest mixing ratios (during PARADE) associated with air mass originating from the south and from the south - west, corresponding approximately to the urbanized Frankfurt and Wiesbaden/Mainz sectors. The ΣPNs mixing ratio varied from below the detection limit to ≈ 3 ppbv during NOTOMO. Low values approaching or below the detection limit were measured during episodes of persistent fog and rainfall. The campaign means for ΣPNs were 505 pptv for PARADE and 677 pptv for NOTOMO, respectively. ΣANs mixing ratios varied from below the detection limit to 1.2 ppbv (PARADE maximum) with campaign mean values of 297 pptv for PARADE and 116 pptv for NOTOMO, repectively. Figures 1 and 2 show that [ΣPNs] and [ΣANs] covary at the

Taunus Observatory and also show a correlation with O_3 both in terms of their diel profile (see later) and day-to-day variability.

Measurements of individual peroxyacyl nitrates are numerous, especially of PAN which usually represents ~ 80% of all peroxy-nitrates in the lower troposphere (Roberts, 1990; Roberts et al., 1998). This has been shown to also be the case at the Taunus Observatory (Thieser et al. 2016). Our measurements of [ΣPNs] are in the range of [PAN] or the sum of individual PANs mixing ratios observed in different urban/suburban locations (Roberts, 1990; Roberts et al., 2007; LaFranchi et al., 2009). Measurements of individual alkyl nitrates are more sparse. Early estimates for the total alkyl nitrate burden at rural locations influenced by urban emissions up to a few hundred pptv were derived by summing the mixing ratio of individually measured alkyl nitrates (C1 up to C8) by gas chromatography technics (Flocke et al., 1991; Flocke et al., 1998; Russo et al., 2010; Worton et al., 2010). Recent developments in chemical ionisation mass spectrometry have enabled measurement of more complex, multifunctionnal nitrates of biogenic origin and revealed the occassional presence of ppbv levels of the sum of measured alkyl nitrates (Beaver et al., 2012). Our measurements of ΣPNs and ΣANs can be more directly compared to those of the University of Califiornia at Berkeley, who have developed and applied the technique of TD-LIF over the last 15 years (Day et al., 2002; Wooldridge et al., 2010; Perring et al., 2013). The mixing ratios of ΣPNs and ΣANs at the Taunus Observatory are comparable to summertime measurements of ΣPNs and ΣANs (0 – 2 ppbv and 0 – 1 ppbv, respectively) at forested sites in California (Day et al., 2003; Murphy et al., 2006; Day et al., 2008).

4.2 Sequestering of NOx as organic nitrates

In this section, we examine how much NO*x* is sequestered as organic nitrates at this site. As HNO_3 was not measured during either campaign, we cannot examine the relative efficiency of NO*x* conversion to organic HNO_3, though we expect the former to dominate in air masses in the continental boundary layer that have significant anthropogenic or biogenic emissions of hydrocarbons (Day et al., 2008).

Figure 3 shows the fraction, *f*(NO*x*), of NO*x* sequestrered as organic nitrates (*f*(NO*x*) = ([ΣPNs] + [ΣANs]) / ([ΣPNs] + [ΣANs] + [NO*x*])), plotted versus [NO*x*] and color coded for temperature. It clearly shows that *f*(NO*x*) is higher at low NO*x*, and could be as high as 0.75 in air masses containing less than 2 ppbv of NO*x*. The lowest values of *f*(NO*x*) measured (< 0.08) were associated with levels of NO*x* in excess of 10 ppbv. At this location, high values of NO_2 are associated with freshly emitted anthopogenic pollution originating from the nearby urban centres. The high values of *f*(NO*x*) during periods of low NO*x* is the result of efficient conversion of NO*x* to longer lived organic nitrates in photochemically aged air masses at this site and also suggests that organic nitrate formation is not limited by NO*x*. For a given level of NO*x*, *f*(NO*x*) is larger when temperatures are higher, reflecting stronger biogenic emissions, and more intense photochemical activity and thus conversion rates of NO*x* to organic nitrates (Olszyna et al., 1994; Day et al., 2008). Low temperatures also increase the rate of transfer of soluble organic nitrates to the aerosol phase, which acts on *f*(NO*x*) in the same direction.

4.3 Diel profiles: Photochemical and meteorological influences

Figure 4 shows the mean diel profiles of $J(O^1D)$, $[O_3]$, temperature, humidity, $[NO_2]$, [ΣPNs] and [ΣANs] for both the PARADE (red lines) and NOTOMO (black lines) campaigns. A number of factors including highly variable (temporal and spatial) local emmisions, irradiance, wind-direction and the complex topography at the site all impose their influence on the diel profiles measured for the organic nitrates.

The mean, daily maxima in global radiation, temperature and O_3 mixing ratio were higher during NOTOMO, indicating on average warmer, sunnier and drier conditions in 2015. Lower average levels of NO_2 were measured during NOTOMO. The mean PARADE NO_2 profile shows two maxima during the day (at ~ 10:00 UTC and ~ 19:00 UTC) which correspond approximately to local rush-hour traffic increases during the working week. These NO_2 maxima are less clearly defined but still apparent in the averaged diel profiles in NOTOMO. A close inspection of the NOTOMO data revealed that the days can be divided into two types, those which display the rush-hour peaks in NO_2 (type 1, altogether seven in a total of thirty days) and those which do not (type 2) As illustrated in Fig. 5, type 1 days were associated with higher temperaures and levels of O_3 and local wind direction that has a large, daytime component from the South, whereas type 2 days were cooler, had less O_3 and the local wind had a dominant westerly component. Air masses arriving from the southerly sectors are influenced by rush-hour traffic from the nearby urban centres, whereas those arriving from the west are cleaner, with an Atlantic influence and more distant emissions of NO*x*. Up-slope winds, resulting from enhanced rates of heating of the mountainside during the warmer periods can also play a role in enhancing rates of transport of NO*x* and photochemically produced trace gases to the site compared to the cooler, cloudier days under the influence of westerly winds. During the PARADE campaign, no clear differentiation in meteorological/photo-chemical situation was possible and the diel profiles represent the entire campaign. The mean ΣPNs profiles during both campaigns (Fig. 4) indicate a growth in mixing ratio starting at about sunrise with a broad daily maxima between ≈ 12:00 and 14:00 for NOTOMO. The mean daily maximum for NOTOMO was about 1.2 ppbv, a factor of two or more than for PARADE. In contrast, during PARADE the mean daily maximum of ΣANs (≈ 0.6 ppbv) was about a factor of three larger than during NOTOMO. The ratio of the mean daily maximum of ANs to PNs, ($[ANs]_{max}$ / $[PNs]_{max}$) was thus very different for the two campaigns, with values of close to one for PARADE and ≈ 0.2 for NOTOMO.

A number of factors influence the relative concentrations of PNs and ANs. In general, higher temperatures are the result of higher levels of insolation and are thus usually related to higher O_3 concentrations and rates of photochemical processing of VOCs. This should lead to higher concentrations of both PNs and ANs. Higher levels of insolation will lead to higher NO to NO_2 ratios and elevated temperaures will reduce the lifetimes of PNs so higher temperature and more insolation both favour AN production over PN production. This is essentially the opposite to what we observe and we conclude that other factors, including the mechanism of organic nitrate production from oxidation of different VOC types and rates of depositional loss of the organic nitrates play a major role in contolling the relative abundance of ANs and PNs at this site (see later).

4.4 Daytime and night-time production of alkyl nitrates

During PARADE, the diel profiles of [ΣANs] show a maximum around 12:00 UTC, similar to the maximum in global radiation which drives primary OH formation, VOCs oxidation and peroxy radical production rates. However, as indicated in Sect. 1, ANs can also be formed by the reaction of NO_3 radicals with biogenically emitted VOCs, which can impact on their diel profile. Figure 6 shows median profiles of [ΣANs] obtained by filtering out periods with fog and rain at the site in which NO_3 would have been absent due to the rapid, heterogeneous scavenging of N_2O_5, with which the former is in thermal equililibrium. We also plot the mean profiles of NO_3 during these nights (representing 16 nights for PARADE and 13 nights for NOTOMO). The most notable changes compared to Fig. 4 are the increase in [ΣANs] during the night. Indeed, for the NOTOMO campaign, the night-time [ΣANs] represent almost 50 % of the day-time value. As described in Thieser et al. (2016) and Sobanski et al. (2016a), the potential artefact caused by thermal decomposition of either $ClNO_2$ or N_2O_5 (present during some nights in amounts up to several hundred pptv) in the hot inlets of the TD-CRDs was accounted for by the simultaneous measurement of both of these trace gases and therefore does not contribute to the night-time signal we ascribe to ANs.

We now explore potential meteorological and chemical contributions to the night-time increases in [ΣANs]. Sobanski et al. (2016b) report occassionally extended NO_3 lifetimes (> 1000 s) at this site that result from sampling from a low-lying residual layer. Compared to the lowest levels, the residual layer is likely to contain higer levels of photochemically generated trace gases (e.g. ANs) which would otherwise be lost by deposition. During PARADE and NOTOMO, the majority of nights were however characterised by NO_3 lifetimes of the order of minutes and less, which indicate that NO_3 is removed by reaction with VOCs, presumably mainly reactive terpenoids with double bonds. Those nights with long NO_3 lifetimes during PARADE were excluded for calculating the [NO_3]and [ΣANs] profiles in Fig. 6.

The reaction between NO_3 and unsaturated VOCs is known to produce alkyl nitrates with a higher yield than the day-time pathway through OH induced oxidation of VOCs and is a plausible explanation of the night-time maxima in ΣANs shown in Fig. 6. In order to assess this, we calculated the day and night-time production of alkyl nitrates during PARADE using measured VOCs (see Table 1). We took values from Atkinson and Arey (2003b) for the rate constants and the alkyl nitrate yields from Perring et al. (2013). For some VOCs, the alkyl nitrate yield is unknown and values were estimated based on the known yield of other, structurally similar compounds.

To estimate the night time-production of ANs, we consider the reaction between NO_2 and O_3 to be the only NO_3 precursor. Of the measured VOCs, isoprene, α-pinene, myrcene and limonene account for > 95% of the NO_3 reactivity and have large yields of ANs. The mean night-time mixing ratios for these four compounds are ≈ 15, 30, 15 and 20 ppt, respectively. The corresponding alkyl nitrate yields are 0.7, 0.15, 0.5 and 0.67, respectively, which allows us to derive a value of 0.47 for the effective alkyl nitrate yield for this VOC mixture. In the absence of laboratory investigations, the alkyl nitrate yield from NO_3 + myrcene is estimated as 50 %. Assuming that each NO_3 generated reacts rapidly with a BVOC, (this implies no significant, indirect loss of NO_3 via the heterogeneous loss of N_2O_5) and taking typical night-time [NO_2] and [O_3] mixing

ratios of 2 and 40 ppbv as observed during PARADE, we calculate the production rate of ANs (Eqn. 2) to be $P(\Sigma ANs)_{night} \approx$ 70 pptv hr^{-1} which is consistent with the increase in ANs observed in the two hours following sunset during either the PARADE or NOTOMO campaigns.

$$P(\Sigma ANs)_{night} = 0.47 k_{(NO_2+O_3)}[NO_2][O_3] \quad (2)$$

To compare the estimated night-time production with the maximum day-time production, it is necessary to know the OH concentration. During the PARADE campaign, OH was measured on only a few days that did not cover those used to derive our diel profiles. Following Bonn et al. (2014), who performed a detailed analysis of OH measurements and their correlation with $J(O^1D)$ during PARADE, we calculate $[OH] = 1.8 \times 10^{11} \times J(O^1D) \approx 3 \times 10^6$ molecule cm^{-3} for the mean [OH] between 11:00 and 13:00 UTC. For an approximate estimate of day-time ANs prodution, we take the campaign mean mixing ratios of each VOC between 11:00 and 13:00 UTC as listed in Table 1. Based on the rate coefficients and mean concentrations of the VOCs, we calculate that ≈ 54 % of production of ANs is due to terpenes, 34 % to alkenes and 7 % to alkanes.

$$P_{\Sigma ANs} = \Sigma_i \alpha_i k_{OH+RH_i}[OH][RH_i] \quad (3)$$

Using equation (3) we thus obtain a total ANs production rate of $P(ANS)_{day} \approx$ 68 pptv hr^{-1} which is very similar to the estimated night-time production. The relative rates of day- and night-time generation of ANs depends on the relative levels of OH and NO_3 (a factor ≈ 200 in favour of NO_3), the yields of ANs (generally larger for NO_3) and the rate constant for reaction with VOCs. The large night-time production rate from NO_3 degradation of VOCs in this forested enviromnent is largely a result of the selective reactivity of NO_3 towards terpenes, which have large AN yields.

Although we calculate similar production rates of ANs during the night when NO_3 is present, the daytime maximum in the ANs mixing ratio is significantly larger in both campaigns. This may be explained if the lifetime of ΣANs with respect to chemical or depositional loss is longer during the day than during the night, a consequence of enhanced deposition in a stably stratified, shallow nocturnal boundary layer and the different chemical composition and volatility of the ANs generated. The addition of NO_3 to the double bonds of terpenoids results in the generation of multifunctional, branched alkyl nitrates, with low volatility and a high propensity for condensation on aerosol. The reaction of NO_3 with e.g. limonene results in a substantial yield of organic nitrates and a mass based, secondary organic aerosol yield of ≈ 30 % (Fry et al., 2011; Fry et al., 2014). As ≈ 50 % of OH reactivity is with non-terpenoid VOCs at this site (see above), a higher fraction of mono-functionnal, linear chained alkyl nitrates are formed, which have larger vapour pressures and are less likely to condense onto particles. The lower lifetime of night-time generated ΣANs at this and other forested sites is thus likely to be the result of increased rate of aerosol scavanging of the low volatilitly ANs compared to those generated in the day, which will also be enhanced by the lower temperatures and higher relative humidities encountered at night-time. This result is consistent with

ideas that the NO_3 oxidation of biogenic VOCs can lead to appreciable organo-nitrate content in atmospheric particulate matter (Fry et al., 2011; Fry et al., 2014).

4.5 ANs yield from OH initiated VOC oxidation.

A positive correlation between organic nitrates and O_3 has been observed (Kourtidis et al., 1993; Williams et al., 1997; Roberts et al., 1998; Schrimpf et al., 1998; Day et al., 2003) and is due to the common production pathways of these trace gases. In rural and semi-rural locations, the build up of O_3 during the day is related to the NO*x* catalysed photo-oxidation of VOCs, including the reaction of organic peroxy radicals with NO*x*. These processes also dominate the daytime production of organic nitrates. As discussed in Sect. 1, alkyl nitrates are produced via a minor branch of the reaction between NO and organic peroxy radical, while the majority of reactive collisions result in the formation of NO_2 and (via its photolysis) the formation of O_3 (reaction R4 to R5). Laboratory experiments have shown that the branching ratio to ANs is strongly dependent on the identity of the peroxy radical and also varies with temperature and pressure (Perring et al., 2013). As we measure total alkyl nitrates, the effective branching ratio is determined by the particular VOC mixture encountered. Following the methodology developed by the Berkeley group (Day et al., 2003; Rosen et al., 2004) the production rates of O_3 (P_{O3}) is given by eqn. (4).

$$P_{O3} = \Sigma_i \gamma_i (1 - \alpha_i) k_{(OH+RH_i}[OH][RH_i] \quad \text{Eq. (4)}$$

where α is the branching ratio to nitrate formation in the reaction between the organic peroxy radical and NO, and γ is the number of O_3 produced per VOC oxidized, which can be between one and three but is equal to two for many atmospherically relevant VOCs, given sufficient NO (see Table 1) (Rosen et al., 2004). This can be combined with eqn. (3) to give:

$$\frac{\Delta O_3}{\Delta \Sigma ANs} = \frac{\int (P_{O3} - D_{O3} + E_{O3}) dt}{\int (P_{\Sigma ANs} - D_{\Sigma ANs} + E_{\Sigma ANs}) dt} \quad \text{Eq. (5)}$$

$$\frac{\Delta O_3}{\Delta \Sigma ANs} = \frac{2(1-\alpha)}{\alpha} \approx \frac{2}{\alpha} \quad \text{Eq. (6)}$$

In which D and E represent terms for deposition and entrainment, respectively. The ratio of O_3 to ΣANs after the OH oxidation of a VOC mixture has proceeded for a certain time, *dt*, is given by Eq. (5). At sufficiently high levels of OH, VOCs and NO, the photochemical production terms can be assumed to be larger than the loss terms and Eq. (5) simplifies to Eq. (6). In principal, a plot of [O_3] versus [ΣANs] should then yield a straight line, with a slope that is proportional to an average value of the branching ratio to ANs. The values of α we calculate using the measurement of ΣANs and O_3 is designated $\alpha_{av}^{\Sigma ANs}$. Alternatively, an average value of α can be calculated from measurement of the VOCs that react with OH, their rate constant and the individual yield of alkyl nitrate from each reaction and the O_3 yield, which we then designate α_{av}^{VOCi}.

For both the PARADE and NOTOMO campaigns, we analysed the mixing ratios of ANs and O_3 between 11:00 and 13:00 UTC (around the peak in OH levels) to calculate $\alpha_{\mathrm{av}}^{\Sigma\mathrm{ANs}}$. The results, displayed in Fig. 7, indicate a value of $\alpha_{\mathrm{av}}^{\Sigma\mathrm{ANs}}\ (PARADE) = 7.2 \pm 0.5$ % ($R^2 = 0.49$). The intercept, 28.6 ± 1.2 ppbv, is indicative of background levels of O_3. In the NOTOMO dataset, the yield of ANs is low and the data very scattered with a poor correlation coefficient, hence no fit was carried out and we simply plot (black lines) two lines which encompass the whole dataset with corresponding values of α equal to 0.5 % and 1.7 % which is significantly lower than the derived α for PARADE. For NOTOMO, in which low mixing ratios of ANs were encountered, the vertical grouping of the data apparent in Fig. 7 (i.e. low resolution in concentration) is a result of the corrective procedure for extracting mixing ratios from raw data obtained in the hot and cold inlets, which involves iterative numerical simulation which converges when 1% agreement between observation and simulation is achieved (Sobanski et al., 2016a).

For the PARADE campaign, during which VOCs were measured, we derive a value of $\alpha_{\mathrm{av}}^{\mathrm{VOCi}}(PARADE) = 5.9$ % for the same period around noon (UTC) which is consistent with that derived from measured ΣANs and [O_3]. Irrespective of method used to derive the branching ratio to AN formation, the high values obtained reflect the fact that a significant fraction of OH reactivity is due to biogenic VOCs (especially terpenoids including isoprene, monoterpenes and sesquiterpenes), that have large yields of alkyl nitrates.

To some extent, the agreement may be fortuitous as both methods to derive α_{av} involve assumptions that may be only partially applicable. The value of $\alpha_{\mathrm{av}}^{\mathrm{VOCi}}$ calculated using individual VOC measurements and their respective alkyl nitrate yields is associated with a rather large uncertainty as it assumes that all VOCs with which OH reacts were actually measured during the campaign and that their alkyl nitrate yields are well known. For example, the products of isoprene oxidation, methyl-vinyl-ketone and methacrolein have high reported α values (Paulot et al., 2009) and high rate constants for reaction with OH which, if taken into account would increase the overall calculated α value. Regarding the individual nitrate yields, some values used to calculate the average (see Table 1) are not precisely determined in the literature while others are estimated. For example, the reported yields of alkyl nitrates in the reaction of OH with isoprene in the presence of NO*x* ranges from 4 to 15% (Perring et al., 2013). This analysis will also be biased if e.g. local emissions of biogenics are larger than those averaged over the time period over which O_3 and ANs were formed (i.e. when plumes containing pollution from urban areas are transported to the site).

Likewise, neglecting terms for entrainment and deposition of ANs and O_3 will introduce a variable bias into calculations of $\alpha_{av}^{\Sigma\mathrm{ANs}}$. In the absence of information regarding the deposition rate of a mixture of multi-functional nitrates or O_3 to the topographically complex terrain at the Taunus Observatory a more detailed analysis is however not warranted. The analysis does however make comparison with similar analyses for ΣANs measurements possible, and our derived values of $\alpha_{av}^{\Sigma\mathrm{ANs}}$ are consistent with those summarised by Perring et al (Perring et al., 2013) who list values obtained both by observation of ANs (7.1 % > $\alpha_{av}^{\Sigma\mathrm{ANs}}$ > 0.8 %) and calculated from VOC measurements (10.6 % > $\alpha_{av}^{\mathrm{VOCi}}$ > 0.1 %) in various rural and urban locations.

The difference in $\alpha_{av}^{\Sigma ANs}$ between PARADE (7.2 ± 0.5 %) and NOTOMO (< 2 %) is significant. The cause for this difference may be related to a breakdown of the assumption that depositional losses and/or entrainment of ANs and O_3 are negligible. Dry deposition is often regarded as a major sink of alkyl nitrates especially for those derived from biogenic VOCs, and enhanced rates of deposition loss of ANs during NOTOMO would help explain the divergence between the results obtained. The relative humidity, an important factor influencing the deposition velocity for soluble species like isoprene derived alkyl nitrates, was very similar during both campaigns with a median humidity at noon of 60% for PARADE and 57% for NOTOMO (see Fig. 4) and therefore is unlikely to have caused different deposition rates. Likewise, rates of radiative heating for the photochemically active days during both campaigns were similar, so that boundary layer evolution is also expected to be similar. A more likely explanation for the different values of α_{av} obtained is that the VOC mixture at the mountain top was different between the two years. No VOCS were measured during NOTOMO, but the recurrent damp and foggy conditions are likely to have significantly decreased emissions of BVOCs in 2015, resulting in lower rates of alkyl nitrate formation.

4. Conclusions

By measuring total organic nitrates, NO, NO_2 and NO_3 we have shown that a significant fraction (up to 75 %) of NO*x* is sequestered as gas-phase organic nitrates at this forested site with urban influence. During the 2011 PARADE campaign, ΣANs and ΣPNs were measured in similar concentrations, whereas in NOTOMO (2015) formation of ΣANs was weaker, presumably due to weaker biogenic emissions associated with lower temperatures. Based on an estimate of the OH concentration and the NO_3 production term we show that both night-time (NO_3 initiated) and daytime (OH initiated) chemistry contributes to the formation of ANs, which is reflected in their diel profile. Despite the similar production rate, daytime ANs are more abundant, possibly reflecting their lower rates of loss by deposition, a result of differing night-time versus daytime boundary layer dynamics and chemical properties of the ANs formed. The effective branching ratio to ANs formation from the OH initiated oxidation of VOCs, estimated by comparing ANs and O_3 concentrations and also from VOC analysis, is ~ 5-7 %.

Acknowledgements

We thank Heinz Bingemer for logistical support and use of the facilities at the Taunus Observatory during the NOTOMO and PARADE campaigns. We thank Horst Fischer for making the PARADE NO dataset available and the HLUG for provision of meteorological data as well as O_3 measurements. We thank DuPont for provision of a sample of the FEP TE 9568 suspension used to coat the cavity walls. This work was carried out in part fulfilment of the PhD of Nicolas Sobanski at the Johannes Gutenberg University in Mainz, Germany.

References

Atkinson, R.: Atmospheric chemistry of VOCs and NOx, Atmos. Env., 34, 2063-2101, 2000.

Atkinson, R., and Arey, J.: Gas-phase tropospheric chemistry of biogenic volatile organic compounds: a review, Atmos. Env., 37, S197-S219, 2003a.

Atkinson, R., and Arey, J.: Atmospheric degradation of volatile organic compounds, Chem. Rev., 103, 4605-4638, doi:10.1021/cr0206420, 2003b.

Atlas, E.: Evidence for > C_3 alkyl nitrates in rural and remote atmosphere, Nature, 331, 426-428, 1988.

Ayres, B. R., Allen, H. M., Draper, D. C., Brown, S. S., Wild, R. J., Jimenez, J. L., Day, D. A., Campuzano-Jost, P., Hu, W., de Gouw, J., Koss, A., Cohen, R. C., Duffey, K. C., Romer, P., Baumann, K., Edgerton, E., Takahama, S., Thornton, J. A., Lee, B. H., Lopez-Hilfiker, F. D., Mohr, C., Wennberg, P. O., Nguyen, T. B., Teng, A., Goldstein, A. H., Olson, K., and Fry, J. L.: Organic nitrate aerosol formation via NO_3 + biogenic volatile organic compounds in the southeastern United States, Atmos. Chem. Phys., 15, 13377-13392, doi:10.5194/acp-15-13377-2015, 2015.

Beaver, M. R., St Clair, J. M., Paulot, F., Spencer, K. M., Crounse, J. D., LaFranchi, B. W., Min, K. E., Pusede, S. E., Wooldridge, P. J., Schade, G. W., Park, C., Cohen, R. C., and Wennberg, P. O.: Importance of biogenic precursors to the budget of organic nitrates: observations of multifunctional organic nitrates by CIMS and TD-LIF during BEARPEX 2009, Atmos. Chem. Phys., 12, 5773-5785, doi:doi:10.5194/acp-12-5773-2012, 2012.

Blanchard, P., Shepson, P. B., Schiff, H. I., and Drummond, J. W.: Development of a gas chromatograph for trace gas-chromatograph for trace-level measurement of peroxyacetyl nitrate using chemical amplification, Anal. Chem., 65, 2472-2477, doi:10.1021/ac00066a012, 1993.

Bonn, B., Bourtsoukidis, E., Sun, T. S., Bingemer, H., Rondo, L., Javed, U., Li, J., Axinte, R., Li, X., Brauers, T., Sonderfeld, H., Koppmann, R., Sogachev, A., Jacobi, S., and Spracklen, D. V.: The link between atmospheric radicals and newly formed particles at a spruce forest site in Germany, Atmos. Chem. Phys., 14, 10823-10843, doi:10.5194/acp-14-10823-2014, 2014.

Browne, E. C., Perring, A. E., Wooldridge, P. J., Apel, E., Hall, S. R., Huey, L. G., Mao, J., Spencer, K. M., St Clair, J. M., Weinheimer, A. J., Wisthaler, A., and Cohen, R. C.: Global and regional effects of the photochemistry of $CH_3O_2NO_2$: evidence from ARCTAS, Atmos. Chem. Phys., 11, 4209-4219, doi:doi:10.5194/acp-11-4209-2011, 2011.

Browne, E. C., Min, K. E., Wooldridge, P. J., Apel, E., Blake, D. R., Brune, W. H., Cantrell, C. A., Cubison, M. J., Diskin, G. S., Jimenez, J. L., Weinheimer, A. J., Wennberg, P. O., Wisthaler, A., and Cohen, R. C.: Observations of total $RONO_2$ over the boreal forest: NO*x* sinks and HNO_3 sources, Atmos. Chem. Phys., 13, 4543-4562, doi:10.5194/acp-13-4543-2013, 2013.

Buhr, M. P., Parrish, D. D., Norton, R. B., Fehsenfeld, F. C., Sievers, R. E., and Roberts, J. M.: Contribution of Organic Nitrates to the Total Reactive Nitrogen Budget at a Rural Eastern U.S. Site, J. Geophys. Res., 95, 9809-9816, 1990.

Crowley, J. N., Schuster, G., Pouvesle, N., Parchatka, U., Fischer, H., Bonn, B., Bingemer, H., and Lelieveld, J.: Nocturnal nitrogen oxides at a rural mountain site in south-western Germany, Atmos. Chem. Phys., 10, 2795-2812, 2010.

Day, D. A., Wooldridge, P. J., Dillon, M. B., Thornton, J. A., and Cohen, R. C.: A thermal dissociation laser-induced fluorescence instrument for in situ detection of NO_2, peroxy nitrates, alkyl nitrates, and HNO_3, J. Geophys. Res. -Atmos., 107, doi:doi:10.1029/2001jd000779, 2002.

Day, D. A., Dillon, M. B., Wooldridge, P. J., Thornton, J. A., Rosen, R. S., Wood, E. C., and Cohen, R. C.: On alkyl nitrates, O_3, and the "missing NOy", J. Geophys. Res. -Atmos., 108, 4501, doi:doi:10.1029/2003jd003685, 2003.

Day, D. A., Wooldridge, P. J., and Cohen, R. C.: Observations of the effects of temperature on atmospheric HNO3, Sigma ANs, Sigma PNs, and NOx: evidence for a temperature-dependent HOx source, Atmos. Chem. Phys., 8, 1867-1879, 2008.

Fahey, D. W., Hübler, G., Parrish, D. D., Williams, E. J., Norton, R. B., Ridley, B. A., Singh, H. B., Liu, S. C., and Fehsenfeld, F. C.: Reactive Nitrogen Species in the Troposphere: Measurements of NO, NO_2, HNO_3, Particulate Nitrate, Peroxyacetyl Nitrate (PAN), O_3, and Total Reactive Odd Nitrogen (NO_y) at Niwot Ridge, Colorado, J. Geophys. Res., 91, 9781-9793, 1986.

Flocke, F., Volz-Thomas, A., and Kley, D.: Measurements of alkyl nitrates in rural and polluted air masses, Atmospheric Environment. Part A. General Topics, 25, 1951-1960, 1991.

Flocke, F., Volz-Thomas, A., Buers, H. J., Patz, W., Garthe, H. J., and Kley, D.: Long-term measurements of alkyl nitrates in southern Germany 1. General behavior and seasonal and diurnal variation, J. Geophys. Res. -Atmos., 103, 5729-5746, 1998.

Fry, J. L., Kiendler-Scharr, A., Rollins, A. W., Brauers, T., Brown, S. S., Dorn, H. P., Dube, W. P., Fuchs, H., Mensah, A., Rohrer, F., Tillmann, R., Wahner, A., Wooldridge, P. J., and Cohen, R. C.: SOA from limonene: role of NO3 in its generation and degradation, Atmos. Chem. Phys., 11, 3879-3894, doi:10.5194/acp-11-3879-2011, 2011.

Fry, J. L., Draper, D. C., Barsanti, K. C., Smith, J. N., Ortega, J., Winkle, P. M., Lawler, M. J., Brown, S. S., Edwards, P. M., Cohen, R. C., and Lee, L.: Secondary Organic Aerosol Formation and Organic Nitrate Yield from NO_3 Oxidation of Biogenic Hydrocarbons, Env. Sci. Tech., 48, 11944-11953, doi:10.1021/es502204x, 2014.

IUPAC: Task Group on Atmospheric Chemical Kinetic Data Evaluation, (Ammann, M., Cox, R.A., Crowley, J.N., Jenkin, M.E., Mellouki, A., Rossi, M. J., Troe, J. and Wallington, T. J.) http://iupac.pole-ether.fr/index.html., http://iupac.pole-ether.fr/index.html., 2016.

Kourtidis, K. A., Fabian, P., Zerefos, C., and Rappengluck, B.: Peroxyacetyl Nitrate (Pan), Peroxypropionyl Nitrate (Ppn) and Pan Ozone Ratio Measurements at 3 Sites in Germany, Tellus Series B-Chemical and Physical Meteorology, 45, 442-457, doi:DOI 10.1034/j.1600-0889.1993.t01-3-00004.x, 1993.

LaFranchi, B. W., Wolfe, G. M., Thornton, J. A., Harrold, S. A., Browne, E. C., Min, K. E., Wooldridge, P. J., Gilman, J. B., Kuster, W. C., Goldan, P. D., de Gouw, J. A., McKay, M., Goldstein, A. H., Ren, X., Mao, J., and Cohen, R. C.: Closing the peroxy acetyl nitrate budget: observations of acyl peroxy nitrates (PAN, PPN, and MPAN) during BEARPEX 2007, Atmos. Chem. Phys., 9, 7623-7641, doi:doi:10.5194/acp-9-7623-2009, 2009.

Lelieveld, J., Gromov, S., Pozzer, A., and Taraborrelli, D.: Global tropospheric hydroxyl distribution, budget and reactivity, Atmos. Chem. Phys. Discuss., 2016, 1-25, doi:10.5194/acp-2016-160, 2016.

Li, J., Reiffs, A., Parchatka, U., and Fischer, H.: In situ measurements of atmospheric CO and its correlation with NOx and O_3 at a rural mountain site, Metrol. Meas. Sys. , XXII, 25-38, 2015.

Murphy, J. G., Thornton, J. A., Wooldridge, P. J., Day, D. A., Rosen, R. S., Cantrell, C., Shetter, R. E., Lefer, B., and Cohen, R. C.: Measurements of the sum of HO_2NO_2 and $CH_3O_2NO_2$ in the remote troposphere, Atmos. Chem. Phys., 4, 377-384, 2004.

Murphy, J. G., Day, A., Cleary, P. A., Wooldridge, P. J., and Cohen, R. C.: Observations of the diurnal and seasonal trends in nitrogen oxides in the western Sierra Nevada, Atmos. Chem. Phys., 6, 5321-5338, 2006.

Nault, B. A., Garland, C., Pusede, S. E., Wooldridge, P. J., Ullmann, K., Hall, S. R., and Cohen, R. C.: Measurements of $CH_3O_2NO_2$ in the upper troposphere, Atmos. Meas. Tech., 8, 987-997, doi:doi:10.5194/amt-8-987-2015, 2015.

Ng, N. L., Brown, S. S., Archibald, A. T., Atlas, E., Cohen, R. C., Crowley, J. N., Day, D. A., Donahue, N. M., Fry, J. L., Fuchs, H., Griffin, R. J., Guzman, M. I., Hermann, H., Hodzic, A., Iinuma, Y., Jimenez, J. L., Kiendler-Scharr, A., Lee, B. H., Luecken, D. J., Mao, J., McLaren, R., Mutzel, A., Osthoff, H. D., Ouyang, B., Picquet-Varrault, B., Platt, U., Pye, H. O. T., Rudich, Y., Schwantes, R. H., Shiraiwa, M., Stutz, J., Thornton, J. A., Tilgner, A., Williams, B. J., and Zaveri, R. A.: Nitrate radicals and biogenic volatile organic compounds: oxidation, mechanisms and organic aerosol, Atmos. Chem. Phys. Discuss., 2016, 1-111, doi:10.5194/acp-2016-734, 2016.

Olszyna, K. J., Bailey, E. M., Simonaitis, R., and Meagher, J. F.: O_3 and NOy relationships at a rural Site, J. Geophys. Res. -Atmos., 99, 14557-14563, doi:Doi 10.1029/94jd00739, 1994.

Paulot, F., Crounse, J. D., Kjaergaard, H. G., Kroll, J. H., Seinfeld, J. H., and Wennberg, P. O.: Isoprene photooxidation: new insights into the production of acids and organic nitrates, Atmos. Chem. Phys., 9, 1479-1501, 2009.

Perring, A. E., Pusede, S. E., and Cohen, R. C.: An observational perspective on the atmospheric impacts of alkyl and multifunctional nitrates on ozone and secondary organic aerosol, Chem. Rev., 113, 5848-5870, doi:doi:10.1021/cr300520x, 2013.

Phillips, G. J., Tang, M. J., Thieser, J., Brickwedde, B., Schuster, G., Bohn, B., Lelieveld, J., and Crowley, J. N.: Significant concentrations of nitryl chloride observed in rural continental Europe associated with the influence of sea salt chloride and anthropogenic emissions, Geophys. Res. Lett., 39, L10811, doi:10.1029/2012GL051912, 2012.

Ridley, B. A., Shetter, J. D., Walega, J. G., Madronich, S., Elsworth, C. M., Grahek, F. E., Fehsenfeld, F. C., Norton, R. B., Parrish, D. D., Hübler, G., Buhr, M., Williams, E. J., Allwine, E. J., and Westberg, H. H.: The Behavior of Some Organic Nitrates at Boulder and Niwot Ridge, Colorado, J. Geophys. Res., 95, 13949-13961, 1990.

Roberts, J. M., Fajer, R. W., and Springston, S. R.: Capillary gas-chromatographic separation of alkyl nitrates and peroxycarboxylic nitric anhydrides Anal. Chem., 61, 771-772, doi:10.1021/ac00182a026, 1989.

Roberts, J. M.: The atmospheric chemistry of organic nitrates, Atmospheric Environment. Part A. General Topics, 24, 243-287, 1990.

Roberts, J. M., Bertman, S. B., Parrish, D. D., Fehsenfeld, F. C., Jobson, B. T., and Niki, H.: Measurement of alkyl nitrates at Chebogue Point, Nova Scotia during the 1993 North Atlantic Regional Experiment (NARE) intensive, J. Geophys. Res. -Atmos., 103, 13569-13580, 1998.

Roberts, J. M., Marchewka, M., Bertman, S. B., Sommariva, R., Warneke, C., de Gouw, J., Kuster, W., Goldan, P., Williams, E., Lerner, B. M., Murphy, P., and Fehsenfeld, F. C.: Measurements of PANs during the New England air quality study 2002, J. Geophys. Res. -Atmos., 112, doi:Artn D20306, 10.1029/2007jd008667, 2007.

Rollins, A. W., Pusede, S., Wooldridge, P., Min, K. E., Gentner, D. R., Goldstein, A. H., Liu, S., Day, D. A., Russell, L. M., Rubitschun, C. L., Surratt, J. D., and Cohen, R. C.: Gas/particle partitioning of total alkyl nitrates observed with TD-LIF in Bakersfield, J. Geophys. Res. -Atmos., 118, 6651-6662, doi:10.1002/jgrd.50522, 2013.

Rosen, R. S., Wood, E. C., Wooldridge, P. J., Thornton, J. A., Day, D. A., Kuster, W., Williams, E. J., Jobson, B. T., and Cohen, R. C.: Observations of total alkyl nitrates during Texas Air Quality Study 2000: Implications for O_3 and alkyl nitrate photochemistry, J. Geophys. Res. -Atmos., 109, Art. Nr D07303, doi:doi:10.1029/2003jd004227, 2004.

Russo, R. S., Zhou, Y., Haase, K. B., Wingenter, O. W., Frinak, E. K., Mao, H., Talbot, R. W., and Sive, B. C.: Temporal variability, sources, and sinks of C_1-C_5 alkyl nitrates in coastal New England, Atmos. Chem. Phys., 10, 1865-1883, 2010.

Schrimpf, W., Linaerts, K., Muller, K. P., Koppmann, R., and Rudolph, J.: Peroxyacetyl nitrate (PAN) measurements during the POPCORN campaign, J. Atmos. Chem., 31, 139-159, doi:Doi 10.1023/A:1006004031055, 1998.

Schuster, G., Labazan, I., and Crowley, J. N.: A cavity ring down / cavity enhanced absorption device for measurement of ambient NO_3 and N_2O_5, Atmos. Meas. Tech., 2, 1-13, 2009.

Schwantes, R. H., Teng, A. P., Nguyen, T. B., Coggon, M. M., Crounse, J. D., St Clair, J. M., Zhang, X., Schilling, K. A., Seinfeld, J. H., and Wennberg, P. O.: Isoprene NO_3 Oxidation Products from the RO_2 + HO_2 Pathway, J. Phys. Chem. A, 119, 10158-10171, doi:10.1021/acs.jpca.5b06355, 2015.

Sobanski, N., Schuladen, J., Schuster, G., Lelieveld, J., and Crowley, J.: A 5-channel cavity ring-down spectrometer for the detection of NO_2, NO_3, N_2O_5, total peroxy nitrates and total alkyl nitrates, Atmos. Meas. Tech. Discuss., 2016, 1-32, doi:10.5194/amt-2016-191, 2016a.

Sobanski, N., Tang, M. J., Thieser, J., Schuster, G., Pöhler, D., Fischer, H., Song, W., Sauvage, C., Williams, J., Fachinger, J., Berkes, F., Hoor, P., Platt, U., Lelieveld, J., and Crowley, J. N.: Chemical and meteorological influences on the lifetime of NO_3 at a semi-rural mountain site during PARADE, Atmos. Chem. Phys., 16, 4867-4883, doi:10.5194/acp-16-4867-2016, 2016b.

Thieser, J., Schuster, G., Phillips, G. J., Reiffs, A., Parchatka, U., Pöhler, D., Lelieveld, J., and Crowley, J. N.: A two-channel, thermal dissociation cavity-ringdown spectrometer for the detection of ambient NO_2, RO_2NO_2 and $RONO_2$, Atmos. Meas. Tech., 9, 553-576, 2016.

Williams, J., Roberts, J. M., Fehsenfeld, F. C., Bertman, S. B., Buhr, M. P., Goldan, P. D., Hubler, G., Kuster, W. C., Ryerson, T. B., Trainer, M., and Young, V.: Regional ozone from biogenic hydrocarbons deduced from airborne measurements of PAN, PPN, and MPAN, Geophys. Res. Lett., 24, 1099-1102, 1997.

Williams, J., Roberts, J. M., Bertman, S. B., Stroud, C. A., Fehsenfeld, F. C., Baumann, K., Buhr, M. P., Knapp, K., Murphy, P. C., Nowick, M., and Williams, E. J.: A method for the airborne measurement of PAN, PPN, and MPAN, JGR, 105, 28943-28960, 2000.

Wooldridge, P. J., Perring, A. E., Bertram, T. H., Flocke, F. M., Roberts, J. M., Singh, H. B., Huey, L. G., Thornton, J. A., Wolfe, G. M., Murphy, J. G., Fry, J. L., Rollins, A. W., LaFranchi, B. W., and Cohen, R. C.: Total Peroxy Nitrates (ΣPNs) in the atmosphere: the Thermal Dissociation-Laser Induced Fluorescence (TD-LIF) technique and comparisons to speciated PAN measurements, Atmos. Meas. Tech., 3, 593-607, doi:doi:10.5194/amt-3-593-2010, 2010.

Worton, D. R., Reeves, C. E., Penkett, S. A., Sturges, W. T., Slemr, J., Oram, D. E., Bandy, B. J., Bloss, W. J., Carslaw, N., Davey, J., Emmerson, K. M., Gravestock, T. J., Hamilton, J. F., Heard, D. E., Hopkins, J. R., Hulse, A., Ingram, T., Jacob, M. J., Lee, J. D., Leigh, R. J., Lewis, A. C., Monks, P. S., and Smith, S. C.: Alkyl nitrate photochemistry during the tropospheric organic chemistry experiment, Atmos. Env., 44, 773-785, 2010.

Table 1. VOCs measured during the PARADE campaign by GC-MS/FID

VOC	Mean noon time mixing ratios (pptv)	$k_{(OH + VOC)}$ cm^3 $molecule^{-1}$	α(ANs)	P(ANs) pptv hr^{-1}	$P(O_3)$ pptv hr^{-1}
limonene	28	1.71×10^{-10}	0.28	15	75
butadiene	240	6.6×10^{-11}	0.07	12	320
1-pentene	560	3.14×10^{-11}	0.05[b]	9.5	358
myrcene	20	2.15×10^{-10}	0.18[b]	8.5	75
α-pinene[a]	49	5.37×10^{-11}	0.18	5.3	66
i-pentane[a]	282	3.9×10^{-12}	0.35[b]	4.3	22
isoprene	85	1.01×10^{-10}	0.044	4	178
ethylbenzene	26	7.10×10^{-11}	0.1[b]	2	36
benzene	78	1.23×10^{-11}	0.1[b]	1.1	19
n-Pentane[a]	211	3.9×10^{-12}	0.105	1	23
i-Butane[a]	131	2.33×10^{-112}	0.255	0.85	7
toluene	126	6.0×10^{-12}	0.1[b]	0.83	15
m-xylene	46	1.43×10^{-11}	0.1[b]	0.73	13
p-xylene	46	1.43×10^{-11}	0.1[b]	0.73	13
n-Butane[a]	265	2.54×10^{-12}	0.077	0.6	19
hexane	56	5.61×10^{-12}	0.141	0.48	8.3
propene	105	2.63×10^{-11}	0.015	0.45	58
o-xylene	21	1.37×10^{-11}	0.0086	0.33	5.8
cis-2-Butene	15	5.6×10^{-11}	0.037[b]	0.33	17
propane	330	1.15×10^{-12}	0.036	0.15	7.9
ethane	590	2.6×10^{-13}	0.019	0.033	3.3
p-cymene	5	1.51×10^{-11}	0.03	0.025	1.5
ethene	246	8.5×10^{-12}	0.0086	0.02	45
methane	1.8×10^{6}	6.9×10^{-15}	0	0	268
HCHO	1940	8.5×10^{-12}	0	0	358
CO	1.2×10^{5}	2.4×10^{-13}	0	0	303
Sum				**68.3**	**2314.8**

The production rate of alkyl nitrates and O_3 are calculated based on an OH concentration of 3×10^6 molecule cm^{-3}. VOCs are sorted by decreasing production rate of alkyl nitrates. The number of ozone molecules produced per VOC oxidized is taken to be two unless otherwise designated. [a] 2.85 O_3 per VOC oxidised (Rosen et al., 2004). [b] the alkyl nitrate yield is estimated based on the compound structure similarity with other alkyl nitrate yield known coumpounds (Rosen et al., 2004).

Table 2. Minimum, mean and maximum values for relative humidity, temperature, ozone, NO, NO_2 and organic nitrates during the PARADE and NOTOMO campaign.

	PARADE (2011)			NOTOMO (2015)		
Species	Minimum	Maximum	Mean	Minimum	Maximum	Mean
Relative humidity (%)	38	100	77	27	100	70
Temperature (°C)	6	27	15	6	33	17
O_3 (ppbv)	8	81	41	17	150	48
NO_2 (ppbv)	0.3	21	2.7	0.1	15	2
NO (ppbv)	< LOD	5	0.3	0[a]	3[a]	0.3[a]
ΣPNs (ppbv)	< LOD	2	0.5	< LOD	3.2	0.7
ΣANs (ppbv)	< LOD	1.2	0.3	< LOD	0.8	0.1

[a] calculated from photo-stationary state (see text for details).

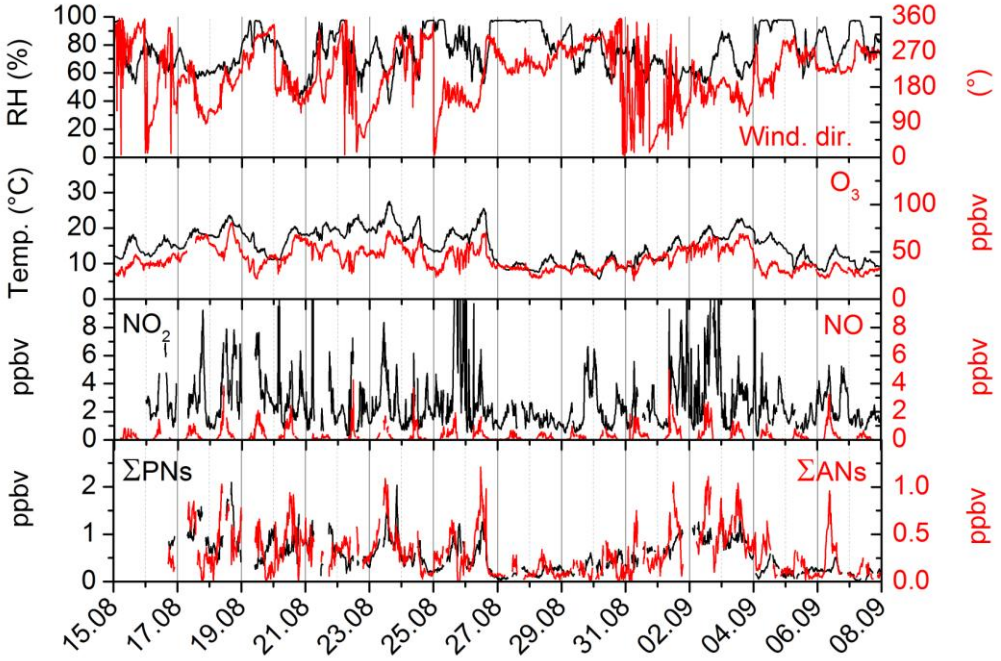

Fig. 1. PARADE 2011: Time-series of relative humidity (RH), wind direction, temperature, and the O_3, NO_2, NO, ΣPNs, and ΣANs mixing ratios.

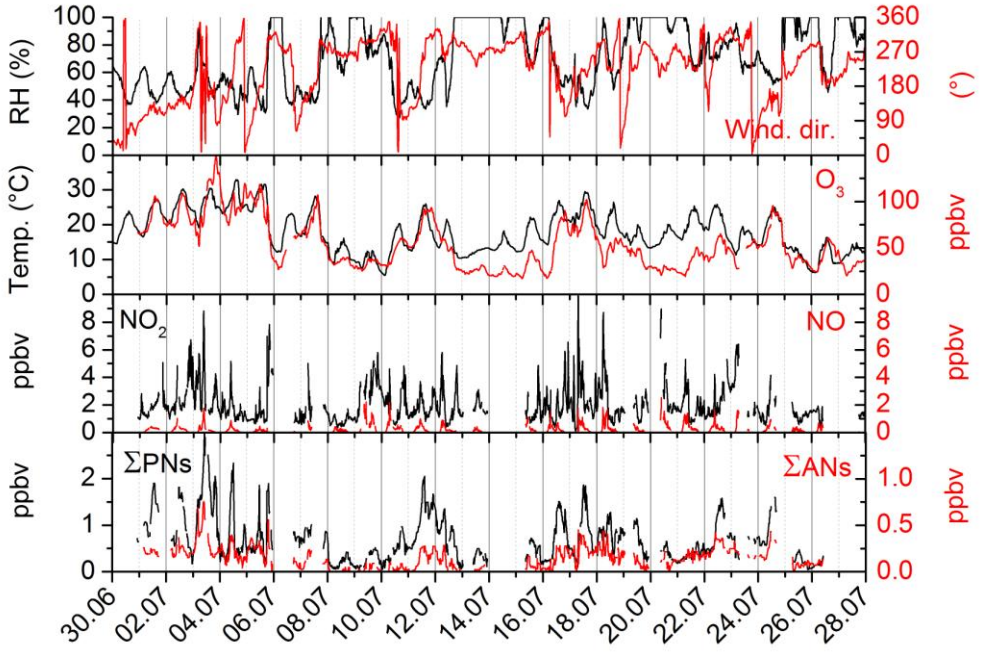

Fig. 2. NOTOMO 2015: Time-series of relative humidity (RH), wind direction, temperature, and the O_3, NO_2, NO, ΣPNs, and ΣANs mixing ratios. The NO mixing ratios were calculated assuming photo-stationary state as described in the text.

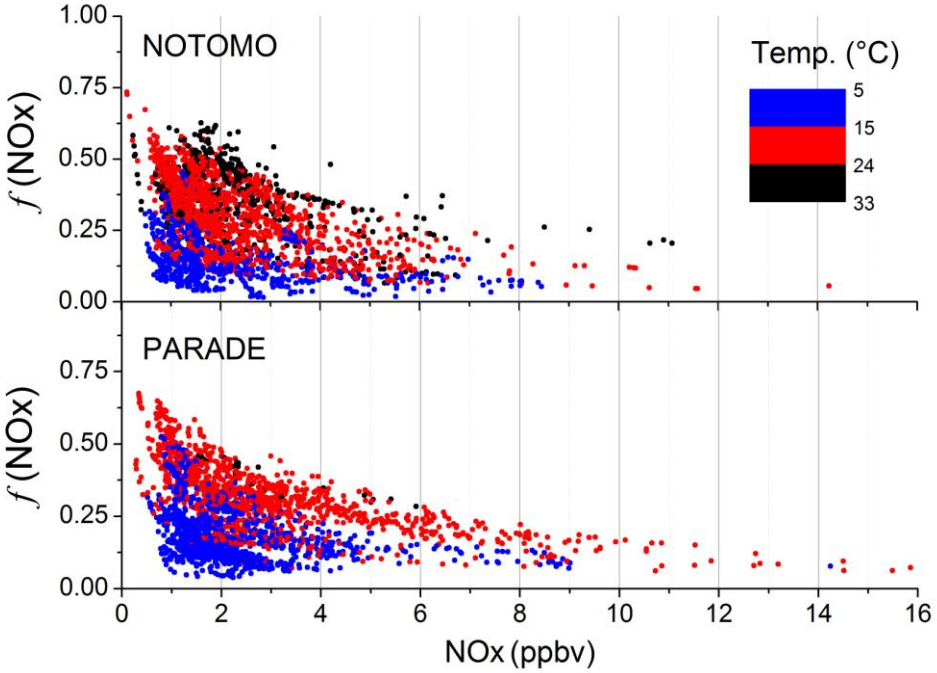

Fig. 3. The fraction of NO*x* sequestered as organic nitrates *f*(NO*x*)= [ΣPNs]+[ΣANs] /([ΣPNs]+[ΣANs]+[NO*x*]) as a function of NO*x* for the NOTOMO and PARADE campaigns, both colour coded for temperature.

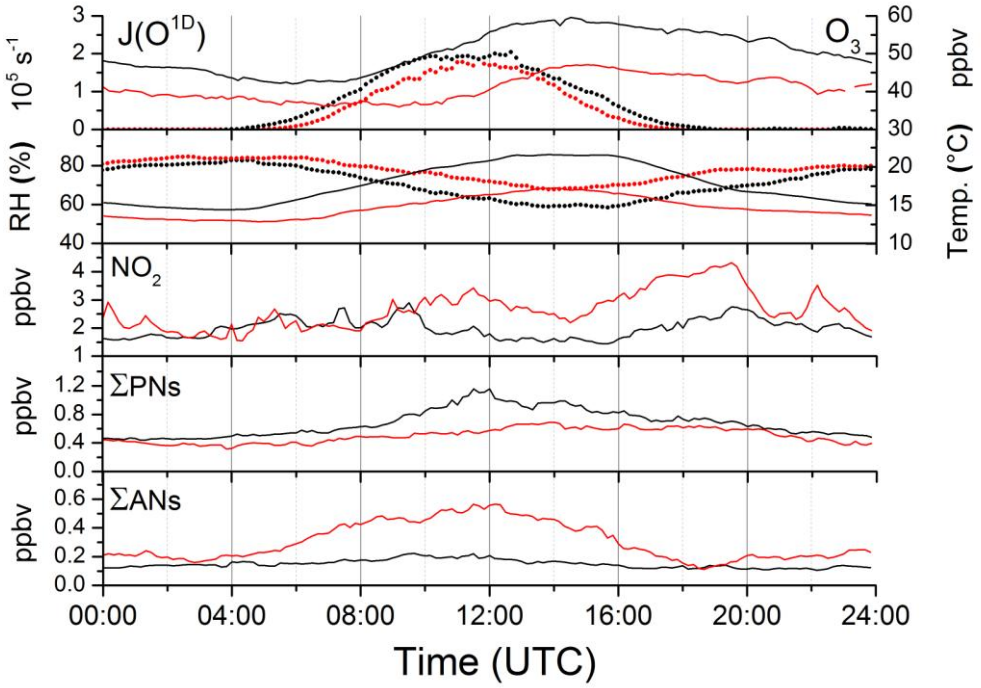

Fig. 4. Mean diel profiles during PARADE (red) and NOTOMO (black) of J(O^1D) and relative humidity (points) and [O_3], temperature, [NO_2], [ΣPNs] and [ΣANs] (lines).

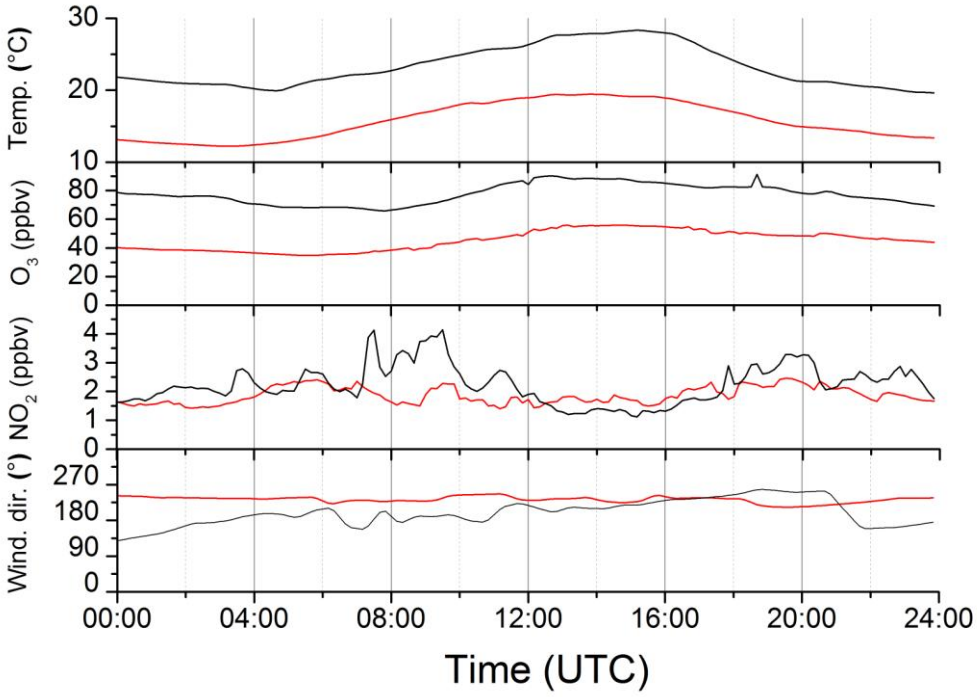

Fig. 5. Mean daily profiles of [O_3], temperature, [NO_2], and wind direction for the NOTOMO campaign separated into days with a clear influence from local rush-hour traffic (black). The rest are shown in red.

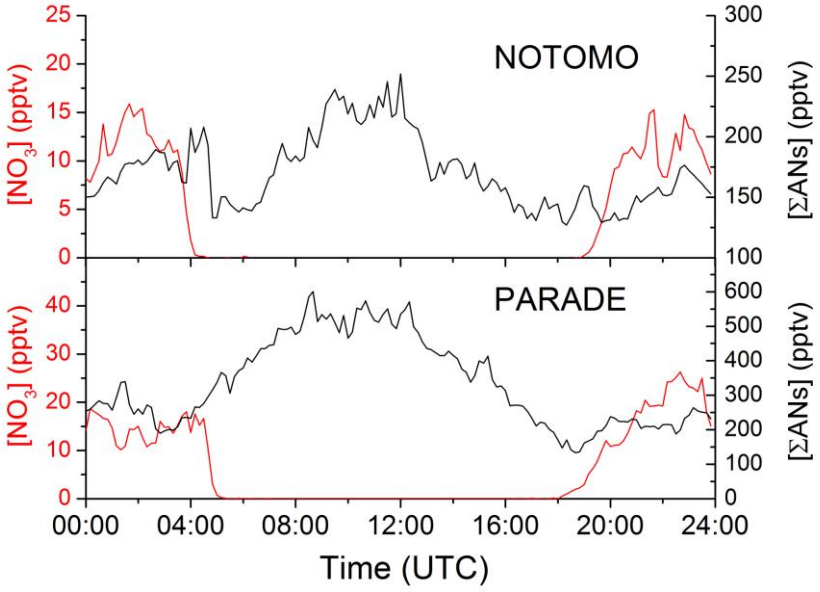

Fig. 6. Mean daily profiles of [NO_3] (red) and [ΣANs] (black) for the NOTOMO (top) and PARADE campaigns (bottom) for relative humidity < 90%.

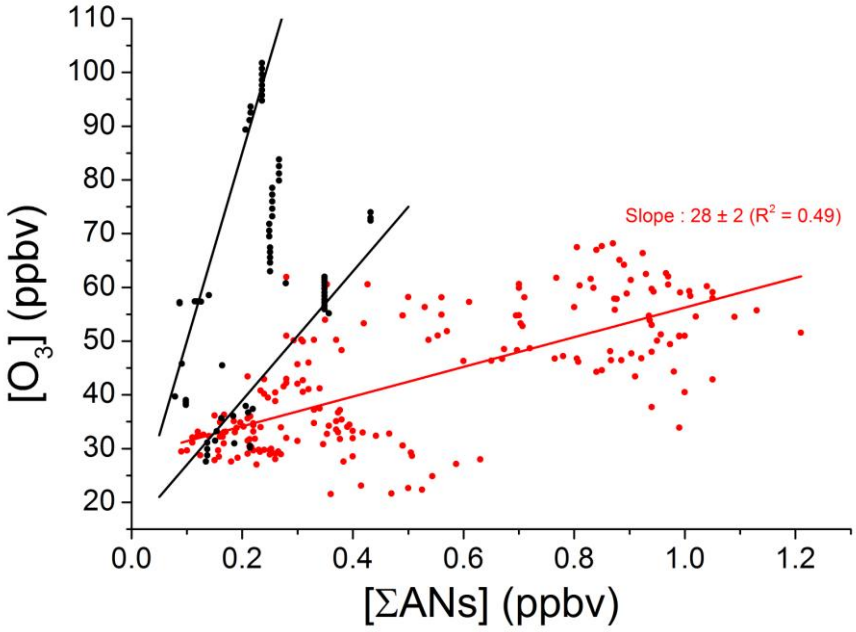

Fig. 7. [O_3] versus [ΣANs] measured between 11:00 and 13:00 UTC for the PARADE (red data points) and NOTOMO campaigns (black data points). The lines represent the best fit for the PARADE (red). For NOTOMO the black line are chosen to encompass all possible values of α assuming a background O_3 level of 15 ppbv. The apparent, poor resolution in the NOTOMO data is the result of the iterative correction procedure as described in the text.